Dispersible Exfoliated Zeolite Nanosheets and Their Application in High Performance Zeolite Membrane

A DISSERTATION
SUBMITTED TO THE FACULTY OF
UNIVERSITY OF MINNESOTA
BY

Kumar Varoon Agrawal

IN PARTIAL FULFILLMENT OF THE REQUIREMENTS
FOR THE DEGREE OF
DOCTOR OF PHILOSOPHY

Michael Tsapatsis, Lorraine F. Francis

October 2013

Acknowledgements

I want to thank my advisors Prof. Michael Tsapatsis and Prof. Lorraine Francis for providing me the opportunity to work in their research laboratories. Without their guidance and mentoring, this thesis would not have reached anywhere. Michael's strategic approach towards conducting research, along with his cautionary attitude aided me in advancing my research in the right direction. His constant push for excellence made me achieve a lot more than what I could have managed otherwise. His calm demeanor during failure and success has always been a source of inspiration. Lorraine has been a great mentor, who has always been eager to help. Her feedback on research and on the way of conducting research helped me become a better scientist. I want to extend my appreciation to Prof. Andreas Stein, Prof. Alon McCormick and Prof. Prodromos Daoutidis for agreeing to serve on my committee.

I am very grateful to the past and present members in the Tsapatsis and the Francis laboratories, with whom I had many beneficial discussions. I especially want to thank Sudeep Maheshwari, Sandeep Kumar, Damien Brewer, Alex Lee, Wei Fan and Dongxia Liu, who helped me to acquire the basic skills needed to conduct my research. I want to thank Zheyu, Nicole, Kevin, Cory and Missy, whose hard work as undergraduate researchers really propelled my research forward. I had a great time working with the students and postdocs. I had great interactions with Bahman, Nafiseh, Xueyi, Garrett, Mi Young, Han, Neel, Heng, Kyle, Bryce, Ankit, Maryam, Balu, Limin, Aparna, Wanlu and Meera. Thank you all.

I wish to express my sincere gratitude to Berna Topuz with whom I worked very closely for the past year and half. She is not only an exceptional colleague, but also a very kind friend. I am deeply indebted to her.

I would like to offer my appreciation to Purnendu prabhu, Anusuya mataji and family, who created for me a home away from home, especially in my first two years. I pay my humble obeisance to you. I am grateful to Teresa Bredahl and Julie Prince who have helped me both professionally and personally.

My friends Anand Gautam, Diwakar Shukla, Manish Mittal, Aruna Ramkrishnan and Hui Sun were always there for me. This journey would not have been possible without

the blessings of my parents, my brother and sister. Their encouragement and motivation during the difficult times really pulled me through. Last but definitely not the least, I want to thank my best friend and fiancé Nandita for her never-ending love and support.

To my Family

Abstract

In the wake of the energy crisis, an efficient separation technology such as membrane is required to replace the energy intensive processes like distillation. High performance zeolite membrane can be fabricated by coating of a thin film of high-aspect-ratio zeolite nanosheets on a porous support. However, the synthesis of highly crystalline and morphologically intact zeolite nanosheets by the direct hydrothermal synthesis has been challenging. Successful reports on the synthesis of zeolite nanosheets by the exfoliation of their layered structure exist, but the synthesis routes provided in these reports often lead to significant damages to the structure and the morphology of nanosheets.

This dissertation focuses on the development of a scalable method for the synthesis of zeolite nanosheets, while preserving their structure and the morphology. MWW and MFI nanosheets were prepared by polymer melt compounding of their layered precursors with polystyrene. Zeolite nanosheets were extracted out of the polymer matrix by solution processing of the zeolite-polymer nanocomposite. Exfoliated nanosheets and their coatings were then characterized by the scanning electron microscopy (SEM), transmission electron microscopy (TEM), atomic force microscopy (AFM), nuclear magnetic resonance (NMR), and X-ray diffraction (XRD). A compact, oriented, 300-nm thick zeolite film was fabricated on a symmetric alumina support by a one-step filter coating method. This nanosheet film demonstrated molecular sieving capabilities after a mild hydrothermal treatment.

Density gradient centrifugation was used to purify the zeolite nanosheets from the polymer matrix, and the large unexfoliated particles, resulting in a two-fold increase in the yield of nanosheets in the final coating suspension. Sub-100 nm thick films of these nanosheets were made on a symmetric alumina supports. Nanosheet films with thickness ranging from 10 nm to 100 nm were prepared on an asymmetric silica supports. In-plane secondary growth of these films by the impregnation growth method led to *b*-oriented, 100-150 nm thick zeolite film that separated xylene isomers with separation factors of 100-800, while providing a high permeance of *p*-xylene (4×10^{-7} moles/m^2-s-Pa).

.

Table of Contents

List of Tables

List of Figures

List of Abbreviations

3DOM	: Three-dimensionally Ordered Macroporous
AFM	: Atomic Force Microscopy
CTAB	: Cetyltrimethyl Ammonium Bromide
CTMA	: Cetyltrimethyl Ammonium Hydroxide
DGC	: Density Gradient Centrifugation
ED	: Electron Diffraction
EISA	: Evaporation Induced Self Assembly
F1	: Fraction 1
F2	: Fraction 2
F3	: Fraction 3
F4	: Fraction 4
FFT	: Fast Fourier Transform
FIB	: Focused Ion Beam
HMI	: Hexamethyleneimine
HRTEM	: High Resolution Transmission Electron Microscopy
KOH	: Potassium Hydroxide
MR	: Member Ring
NMR	: Nuclear Magnetic Resonance
OSDA	: Organic Structure Directing Agent
PSS	: Porous Stainless Steel
PVA	: Poly (vinyl alcohol)
RCF	: Relative Centrifugal Force
SEM	: Scanning Electron Microscopy
SWCNT	: Single-Walled Carbon Nanotubes
TBAOH	: Tetrabutyl Ammonium Hydroxide
TEAOH	: Tetraethyl Ammonium Hydroxide
TEM	: Transmission Electron Microscopy
TEOS	: Tetraethyl Orthosilicate
TGA	: Thermogravimetric Analysis
TMAdaI	: Tetramethyl Adamantanamine Iodide
TMAdaOH	: Tetramethyl Adamantanamine Hydroxide
TMAOH	: Tetramethyl Ammonium Hydroxide
TPABr	: Tetrapropyl Ammonium Bromide
TPAOH	: Tetrapropyl Ammonium Hydroxide
XRD	: X-Ray Diffraction

Chapter 1: An Introduction to Zeolites and Their Thin Films

1.1 Zeolites and Zeolite Membranes

Zeolites are crystalline aluminosilicates comprising a uniform network of SiO_2 and Al_2O_3 tetrahedra.[1, 2] This three dimensional network of tetrahedra in zeolites often houses uniform microporous channels with pore sizes ranging from 0.3 to 2 nm (Fig. 1.1). The pore channels and the structure-property relationship of these zeolites have been widely studied since the discovery of zeolite by a Swedish mineralogist named Axel Fredrick Cronstedt in 1756. Cronstedt coined the term zeolite based on the Greek words *zein* and *lithos* meaning 'boiling stones'. Since then, many naturally occurring zeolites haven been discovered. However, it took another 200 years to synthesize a zeolite. The first synthetic zeolite 'mordenite' was reported by Barrer in 1948.[3] The commercial success of synthetic zeolite A, X, and Y brought zeolites into the industrial and academic limelight.[4] The term 'molecular sieves' was coined for zeolites as they adsorb small molecules (smaller than their pore channel) but reject large molecules.

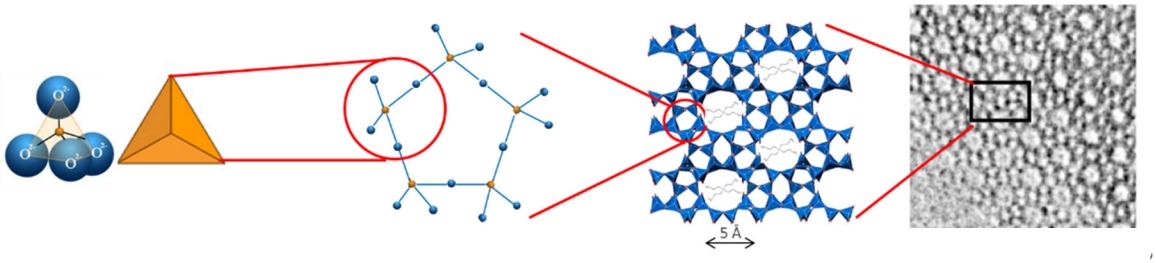

Fig 1.1. The structure of a siliceous zeolite (MFI), built up from a porous network of SiO_2 tetrahedra. The high resolution TEM (HRTEM) image on the right confirms the theoretical structure of MFI.[5]

The chemical and physical properties of zeolites largely determine their applications. For example, the charged structure of the aluminosilicate zeolite plays a key role in applications such as catalysis, ion-exchange and adsorption.[6-9] On the other hand, the performance of charge neutral, siliceous zeolite frameworks relies upon their hydrophobicity and the relative adsorption affinity.[10-12] For example, a thin and compact film of siliceous zeolites can be used as molecular sieving membranes[13-15], barriers[16, 17],

ultralow dielectric constant films[12, 18], sensors, second-order nonlinear optical materials[15, 19], etc.

Zeolite membranes are important because they provide a sustainable, energy efficient route to separate chemicals in contrast to distillation, crystallization and pressure swing adsorption. One prominent advantage of zeolite membranes over other membrane technologies is the chemical and thermal stability of zeolites. Also, the separation performance (permeance and separation efficiency) of zeolite membranes is much better (by a few orders of magnitude) than that of the polymer membranes due to the stiff microporous structure of zeolites.

In the past two decades, a number of studies have demonstrated and discussed the purification of gases (e.g. H_2 from CO_2[17, 20-22], butane isomers[23-25], etc.), organic vapors (xylene isomers[13-15]), and alcohols (ethanol from water[26, 27]) using zeolite membranes. For example, one of the most sought after separation-process is the purification of *p*-xylene from its isomers (*o*-xylene and *m*-xylene). *P*-xylene has a high economic value because it is used as a raw material for the production of terephthalic acid, which is then subsequently processed into PET bottles and polyester clothing. According to a report in the *2012 World Paraxylene and Terephthalates Analysis*, the estimated annual production of *p*-xylene is expected to surpass 30 million tons by 2015[28]. The current process of *p*-xylene production produces a large proportion *m*- and *o*-xylenes, which act as impurities in the further processing steps. Thus, it becomes imperative to separate *p*-xylene from its isomers before further processing. Current technologies use crystallization and distillation methods to separate *p*-xylene from its isomers (*m*-xylene and *o*-xylene), both of which are energy intensive. The boiling points of the xylene isomers are very close (Fig. 1.2), necessitating a very high energy investment in the separation process using distillation. Instead, *p*-xylene can be purified by passing the xylene mixture through a perm-selective zeolite membrane. Since *p*-xylene is a smaller molecule (kinetic diameter ~ 5.8 Å) compared to *o*-xylene (6.8 Å) and *m*-xylene (6.8 Å), a zeolite membrane can efficiently separate out *p*-xylene from its isomers. Thin defect free MFI films have been shown to selectively sieve *p*-xylene as the straight and zig-zag channels of MFI are just big enough to accommodate and transport *p*-

xylene (Fig. 1.3). Based on this selective transport property, a defect free film of MFI is a highly attractive option for the purification of *p*-xylene.

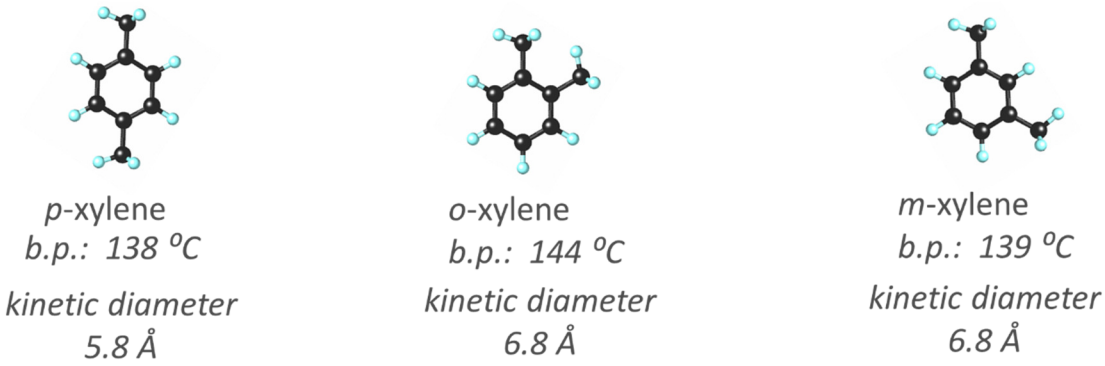

Fig 1.2. A schematic showing the structure, boiling point and kinetic diameter of xylene isomers.

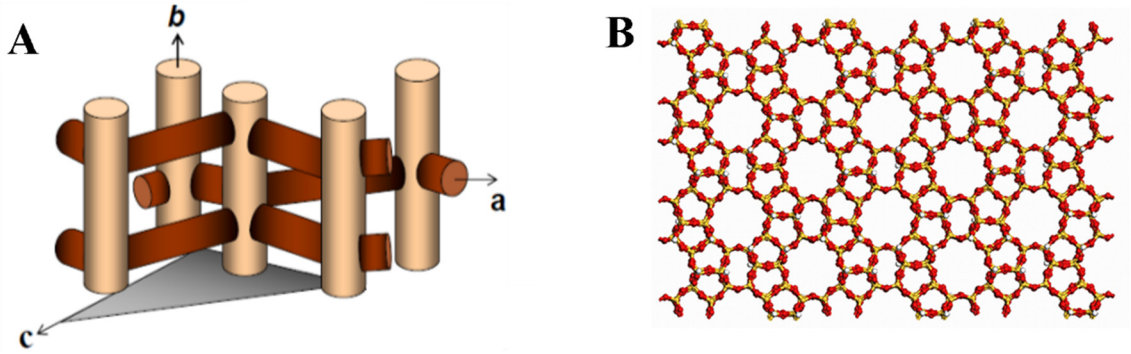

Fig 1.3. A: Cartoon of the MFI channel system showing straight channels along the *b*-axis, and zig-zag channels along the *a*-axis. B: MFI structure along the *b*-axis. The yellow dots are silicon atoms and the red dots are oxygen atoms.

1.2 Fabrication of Zeolite Membranes

Zeolite membranes are usually synthesized by hydrothermal synthesis using a silica source, an organic structure directing agent (OSDA), and a solvent (usually water). Thin zeolite membranes have poor mechanical strength and therefore, they are fabricated on a porous support. While asymmetric supports with the surface roughness of a few nanometers are ideal for the fabrication of thin zeolite films, symmetric supports are often desired due to their low cost.

Zeolite membranes are usually synthesized by either of these two methods - a direct primary growth of the support or a seeded secondary growth. In both of these methods, the support is dipped inside the zeolite growth precursors (source of alumina and silica, OSDA and water) and then heated for the nucleation and growth of the zeolite crystals. While the primary growth method is a simpler growth technique, it does not provide control on the orientation of the zeolite crystals in the membrane.[29] Orientation of the zeolite in the zeolite membrane often determine the separation performance of the membrane. Another drawback of the primary growth technique is that it often leads to a thicker membrane with higher resistance to molecular transport. In comparison, the microstructure of the membrane prepared by seeded growth technique can be controlled by controlling the size, shape and orientation of the seed crystals[30]. Consequently, very thin, oriented membranes can be prepared by the seeded growth method[31]. Fig. 1.4 illustrates an example of a siliceous MFI membrane using the seeded growth method. Here, a *b*-oriented MFI seed layer was inter-grown to obtain an oriented, perm-selective membrane that separated *p*-xylene from *o*-xylene[15].

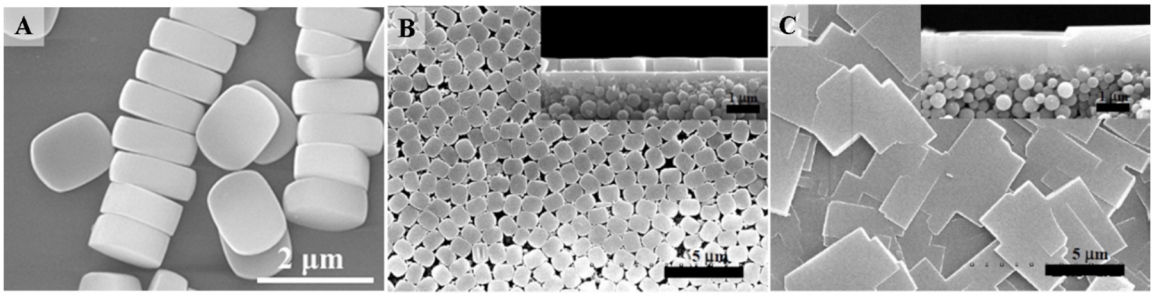

Fig 1.4. A: SEM image of MFI crystals. B: A *b*-oriented MFI seed layer on a porous silica support C: An oriented MFI film after the secondary growth. Images reproduced from Pham et al.[15] Reprinted with permission from AAAS.

Most zeolites have a two- to three- pore channel system, where each channel offers different resistance to molecular transport.[32] Due to this, the orientation of the zeolite film is an important factor for determining the performance of the membrane. For example, the zeolite MFI has a straight 10 member ring (MR) pore channel along its *b*-axis, and a sinusoidal 10 MR channels along *a*-axis of MFI (Fig. 1.3A). Another example is the MWW zeolite which has an hourglass-shaped channel with a 6 MR aperture along its *c*-axis, and

a straight 10 MR channel in the perpendicular direction.[33] Hence, the size, the shape and the orientation of the seed crystals becomes a crucial parameter in determining the microstructure, and consequently the performance of the zeolite membrane.

1.3 Exfoliated Zeolite Nanosheets for the Fabrication of Ultrathin Zeolite Film

Despite the significant progress in the synthesis of perm-selective zeolite membranes, the industrial deployment of the zeolite membrane technology has been limited to small and medium scale processes (~10-100 m^2 in total surface area of the membrane). A major bottleneck in the large scale deployment (~1000 - 10000 m^2) of zeolite membranes is the high cost of zeolite membrane.[31] A zeolite membrane module is estimated to cost between 5000-10000 USD/m^2. Large scale deployment of zeolite membranes is economically unfavorable, unless the cost of zeolite membranes is reduced by a factor of 10. One of the ways to solve this problem is to increase the throughput of zeolite membranes by a factor of 10. Lower surface area of the high throughput zeolite membrane would be needed to separate a specific amount of chemicals. This can compensate the high cost of the zeolite membranes.

The throughput of the zeolite membrane can be increased by fabricating an oriented, ultrathin membrane for certain diffusion limited separations. Key efforts in this direction have been focused on reducing the size of the zeolite seed crystals[8, 11, 31] and redesigning the OSDA[13, 14, 30] or the growth modifiers[34, 35] for achieving oriented growth of the seed layer. Reducing the size of the zeolite crystals by disassembly or dissolution of the larger crystals[31, 36] has been achieved, but the process results in isotropic zeolite nanocrystals that are very difficult to orient on the support. Also, the scalability of this approach is questionable due to the long processing time associated with this method.

Another approach to obtain thin zeolite crystals of the size of a few nanometers is exfoliating layered zeolites into thin sheets.[7] Layered zeolites came into limelight due to their ability to host many molecules in their gallery spacing, which led to an improvement in their performance, especially as catalysts.[6, 8, 37-40] Exfoliation of layered zeolites was

pursued to reduce the diffusional path length for species involved in chemical reactions, and thus improve the product yield. In zeolite membranes, reducing the diffusional path length for chemical species will increase the flux through the membrane, and hence reduce the total membrane area required in the separation process.[10, 17, 22, 41-45] Exfoliated layered zeolites have sheet like morphology with thickness of a few nm and usually an aspect-ratio of 100 or more. Due to this, they are called as *'zeolite nanosheets'*. Due to their high aspect ratios, zeolite nanosheets are extremely flexible and can conform to rough substrates (Fig. 1.5). This enables use of less expensive symmetric supports for fabrication of the zeolite membranes. Also, due to their high aspect ratio and flexibility, zeolite nanosheets can potentially pack better than isotropic crystals. This can potentially lead to revolutionary defect-free zeolite films without the need for secondary hydrothermal synthesis.

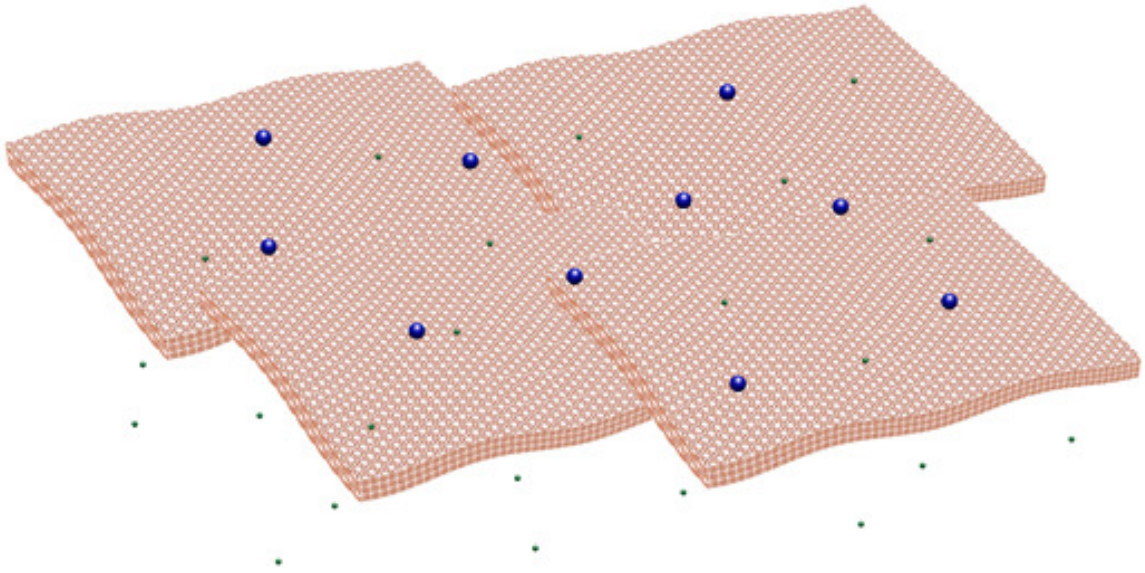

Fig 1.5. A schematic of a high throughput membrane prepared by using high-aspect-ratio MFI nanosheets.

1.4 Thesis Outline

This dissertation is divided into 5 chapters focusing on fabrication of the high throughput zeolite membranes. Chapter 2 describes fabrication of a film of the zeolite platelets on a high throughput stainless steel support. Chapter 3 focuses on the preparation

and processing of the highly crystalline zeolite nanosheets by exfoliation of the layered zeolites. Chapter 4 describes purification of zeolite nanosheets from the polymer and the large unexfoliated particles to enable fabrication of the sub-100 nm thick zeolite film. Chapter 5 reports the study on the in-plane growth of the zeolite nanosheet films to fabricate thin, oriented MFI membranes.

Chapter 2 discusses dip coating of the zeolite platelets on stainless steel tubes of high porosity. A method of preparing the zeolite platelets and their coating suspension for this purpose is described. This is followed by dip coating studies to remove pinhole defects on the surface of the stainless steel tubes. Finally, gas permeation studies were conducted to characterize the transport mechanism in this film.

Chapter 3 describes the synthesis of highly crystalline and morphologically intact MWW and MFI zeolite nanosheets. A novel method based on solution processing of the exfoliated zeolite nanosheets is presented. A series of characterization techniques are employed to determine the crystallinity and the thickness of the exfoliated zeolite nanosheets. Thin films of these zeolite nanosheets are prepared on the membrane supports using a scalable filter coating technique. The suitability of these films in separation of xylene isomers is demonstrated.

Chapter 4 discusses purification of the zeolite nanosheets to remove the unwanted polymer matrix and the unexfoliated zeolite particles from the coating suspension. Density gradient centrifugation in a nonlinear stack of organic solvents is employed to purify the nanosheets. Use of these purified nanosheets to fabricate a sub-100 nm thick zeolite film is explored.

Chapter 5 describes the attempts made towards attaining in-plane growth of the sub-100 nm thick films of the zeolite nanosheets. Parameters affecting the crystal growth were studied by varying the growth conditions. The membranes were characterized by microscopy and gas permeation. Special attention was given to the minimization of the zeolite film thickness.

Chapter 6 summarizes the progress in using thin films of zeolites for fabricating high throughput membranes. Possible future research opportunities pertaining to zeolite nanosheets and their films are outlined in Chapter 7.

Chapter 2: Coating of High Throughput Supports

*To be submitted.

2.1 Introduction

Fabrication of a high throughput zeolite films is desirable for the large scale deployment of zeolite membranes[31]. The cost of a zeolite membrane module is estimated to be \$5000-\$10000 per m^2, which is not economically viable for the large scale deployment of these membranes (greater than a 1000 m^2 of surface area). One of the approaches to compensate for the high cost of the zeolite membranes is to increase the performance of the membrane. This can be achieved by employing a high throughput support for the fabrication of the zeolite membranes.[46] Commercially available high throughput supports include those made of sintered metals and ceramics in the shape of tubes and disks. Tubular metal supports have an advantage over the tubular ceramic supports that they can be easily sealed with the gas supply lines using commercially available sealing materials. However, the metal supports have much higher thermal expansion coefficient than that of the zeolites. This can lead to thermal stress induced cracking or delamination of the zeolite films during the heat treatment. Another inherent challenge with the high throughput supports is that they usually have an extremely rough surface, as pore openings can be as large as 20-50 μm, despite of having a pore aperture as small as 1 μm.[47]

A common approach to mitigate the high surface roughness of the stainless steel supports is fabrication of a smooth coating on top of the support.[48] However, these intermediate layers often lead to poor adhesion and weak mechanical strength of the final membrane.[49] Also, addition of an intermediate layers is expensive as each layer usually requires additional time-consuming drying and sintering steps. One strategy to eliminate the intermediate layer is use of high aspect ratio zeolite platelets. Due to their large lateral size, zeolite platelets can be deposited on top of the support pore aperture. High coverage of the support surface can be obtained using a much smaller number of platelets compared

to coatings of isotropic particles. Also, oriented films prepared using zeolite platelets can be thinner than that prepared using the isotropic particles, helping in reduction of the thermal stress induced cracking and delamination issues. Pure silica zeolites such as ITQ-1 can be synthesized with platelet morphology having lateral size of 1-3 µm and thickness of 50 nm.[50] These platelets are ideal for the fabrication of a thin zeolite film on the high throughput stainless steel tubes with the pore aperture of 1 µm. A defect free ITQ-1 film on a porous stainless steel (PSS) support can be used for separation of He and H_2 from CO_2 and N_2 due to 3 Å pore aperture of ITQ-1.[33] Fig. 2.1 shows a schematic of the layered structure of the ITQ-1 platelets comprising of hourglass shaped pore channels, and 3 Å pore apertures formed by 6 member rings (MR) of silica tetrahedra.

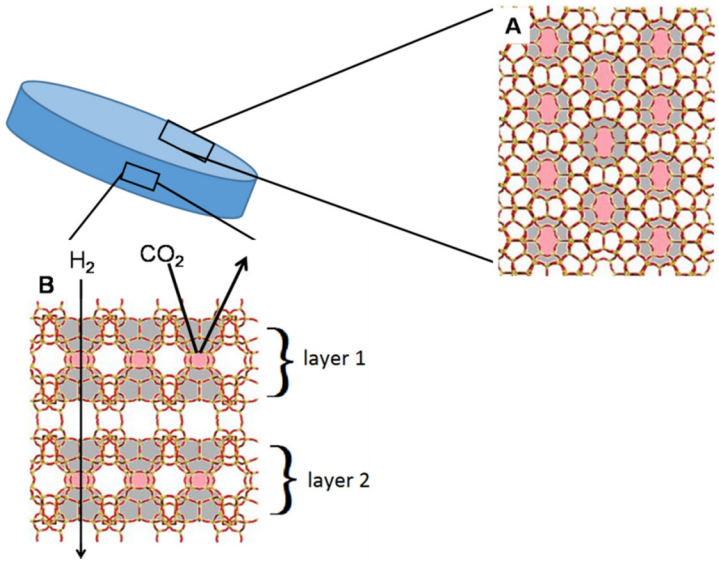

Fig 2.1. A: Schematic of an ITQ-1 platelet viewed along its thin dimension as well as its cross-section. The 6 MR present in the structure of ITQ-1 are highlighted in pink while the 12 MR hourglass pores leading to the 6MR transport limiting pores are highlighted in grey. The arrow mark transport path of H_2 through the hourglass shaped pore channel of ITQ-1.

2.2 Synthesis of ITQ-1 Platelets and Their Coating Suspension

The ITQ-1 platelets were synthesized by a two-step process. In the first step, the OSDA for ITQ-1, N,N,N-trimethyl-1-adamantammonium hydroxide (TMAdaOH) was synthesized. In the second-step, the ITQ-1 crystals were produced by hydrothermal synthesis.

2.2.1 Synthesis of TMAdaOH

TMAdaOH is not commercially available, and hence an in-house protocol was developed for the synthesis based on a previously reported method by Liu et al.[51] The synthesis of this quaternary amine was carried out by the alkylation of 1-adamantamine by iodomethane followed by an ion-exchange step to replace the iodide ion with a hydroxide ion.

The synthesis was carried out by dissolving 14.001 g of 1-adamantamine (97%, Sigma-Aldrich) in 150 ml chloroform in a 250 ml conical flask. Following that, 34.05 g of $K_2CO_3 \cdot 1.5H_2O$ was added to this solution while ensuring continuous stirring. The potassium hydroxide acts as a moisture scavenger in the reaction. Stirring was monitored to ensure the continuous mixing of the potassium hydroxide during the reaction. The conical flask was covered with an aluminum foil to avoid exposure to light and thus, preventing the photolytic degradation of the alkyl iodide. Since the addition of the alkyl iodide to the chloroform is highly exothermic, the reaction flask was cooled in an ice bath before the addition of the chloroform. Once the conical flask was cool, 39.42 g of methyl iodide was added slowly while stirring the solution. After 24 hours, additional 19.5 g of methyl iodide was added slowly. The reaction mixture was continuously stirred at room temperature for a period of 7 days. At the end of the reaction, the product was filtered over a filter paper (Whatman qualitative filter paper, grade 415) to remove the solids. The cake was washed with additional chloroform to fully recover the product, and then the washed solution was added to the filtrate. The filtrate solution contained the product, which was recovered by evaporating the solution using a rotary evaporator (Buchi rotovap). The resulting solid was purified by washing the solid with diethyl ether. This was done by dispersing the solid in the diethyl ether followed by filtering the dispersion to remove any unreacted 1-adamantamine. The unreacted 1-adamantamine separates out by dissolving in the diethyl ether. The filtered cake was dried in the rotary evaporator to obtain the iodide salt of the OSDA (N,N,N-trimethyl-1-adamantammonium iodide, TMAdaI). 1H and 13C Nuclear magnetic resonance (NMR) and elemental analysis (Table 2.1) was carried out to confirm the chemical composition of the product formed in the synthesis.

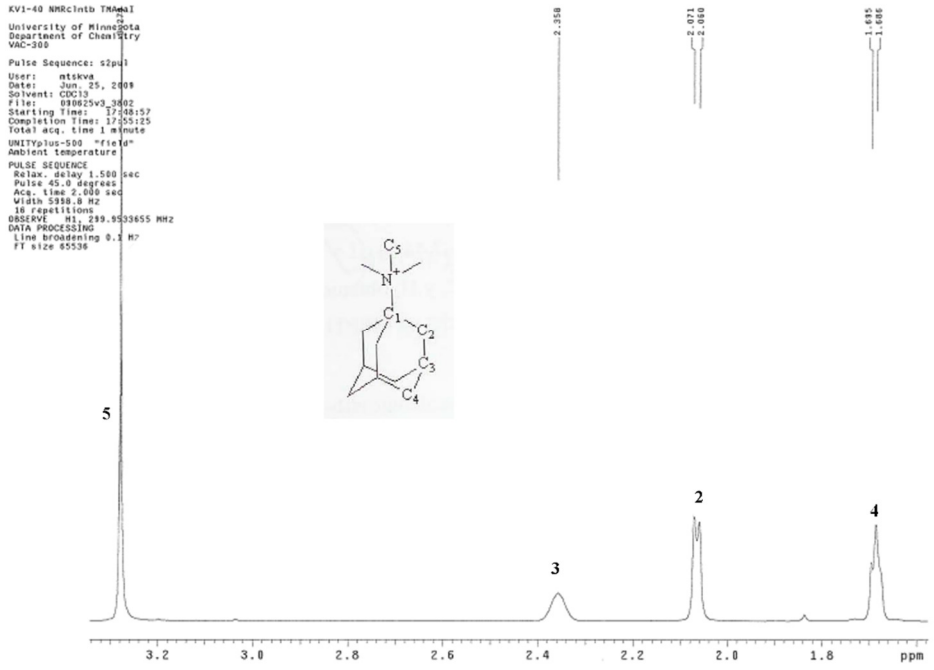

Fig 2.2. 1H NMR of TMAdaI confirming a successful synthesis.

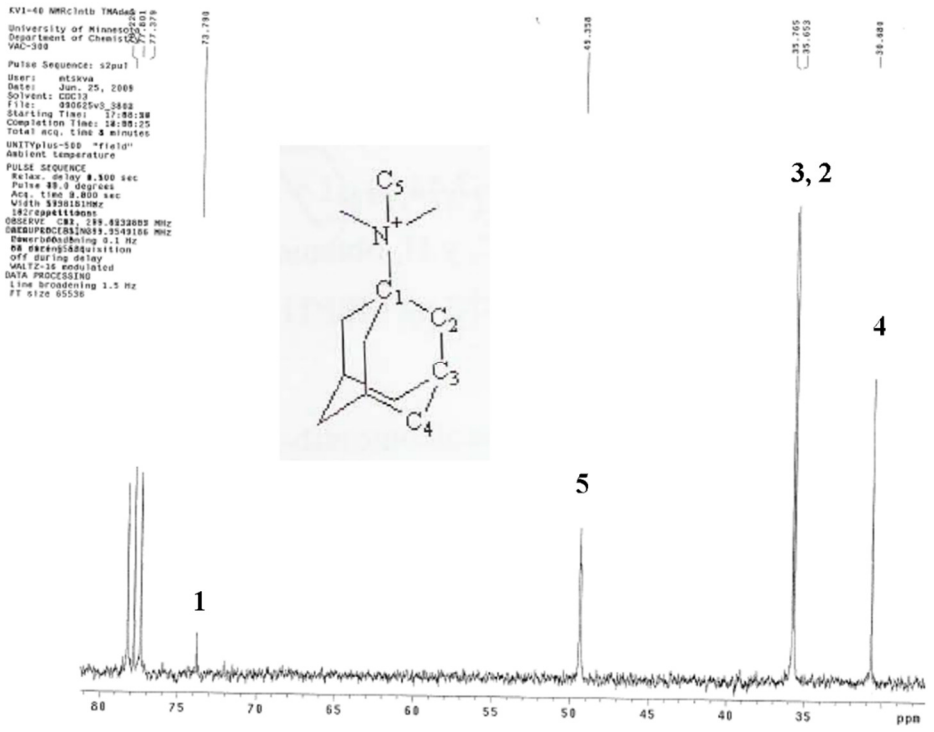

Fig 2.3. 13C NMR of TMAdaI confirming a successful synthesis.

Table 2.1. Elemental analysis of TMAdaI confirming a successful synthesis.

Element	Theoretical Prediction	Experiment 1	Experiment 2
C	48.59	48.65	48.63
H	7.53	7.38	7.54
N	4.36	4.36	4.29

For the synthesis of TMAdaOH, TMAdaI was ion-exchanged with AgO. In a typical ion-exchange reaction, TMAdaI was dissolved in water to make a 0.2 M solution. Then the excess silver oxide was mixed with the TMAdaI solution. The solution was covered by an aluminum foil to prevent the photolytic degradation of AgO. The Ion-exchange process was carried out by stirring the mixture for 7 days. After 7 days, the solution was filtered to remove the brown silver iodide precipitate. The concentration of the TMAdaOH solution was determined by titrating a small amount of TMAdaOH solution with 0.1 N HCl. The water in the OSDA solution was evaporated to increase the concentration of the TMAdaOH solution to at least 0.32M. This solution was then used to synthesize the ITQ-1 platelets.

2.2.2 Hydrothermal Synthesis of the ITQ-1 Platelets

ITQ-1 was synthesized by following the recipe developed by Camblor et. al.[50] For the synthesis of ITQ-1, fumed silica (Cab-O-Sil M5, Cabot Corp.) was mixed with TMAdaOH, hexamethyleneimine (HMI) (Sigma Aldrich), NaCl (Sigma Aldrich) and distilled water to obtain a gel composition of SiO_2 : 0.25 TMAdaOH : 0.31 HMI : 0.20 NaCl : 44 H_2O. Although the ITQ-1 platelets can be prepared without NaCl, the presence of the salt increases the final crystal size, which is desired for a good coverage of the wide pore aperture of the PSS tube. After stirring the synthesis gel for 5 hours at room temperature, the gel was transferred to a Teflon-lined steel autoclave. The hydrothermal synthesis was carried out at 150 ^{0}C, while rotating the autoclave. After 5 days, the heating was stopped and the gel in the autoclave was centrifuged to obtain a yellowish cake. The cake was washed with distilled water to reduce the pH to 9. The final product was obtained by drying the cake in a vacuum oven at 130 ^{0}C. The morphology and structure of the ITQ-

1 platelets was confirmed by Scanning electron microscopy (SEM) and XRD (X-ray diffraction), respectively, as shown in Fig. 2.2. As-synthesized ITQ-1 platelets were 30-50 nm thick with a lateral size of 2-3 μm. The platelets consisted of many layers of ITQ-1 nanosheets, which had inter-grown with each other. Powder XRD of the as-synthesized ITQ-1 confirmed the high crystallinity of the platelets. High crystallinity of the ITQ-1 particles is desired for their application as molecular sieving membranes. The (001) and (002) peaks in the powder XRD pattern confirmed the layered structure of the as-made ITQ-1 with an interlayer spacing of 2.7 nm.

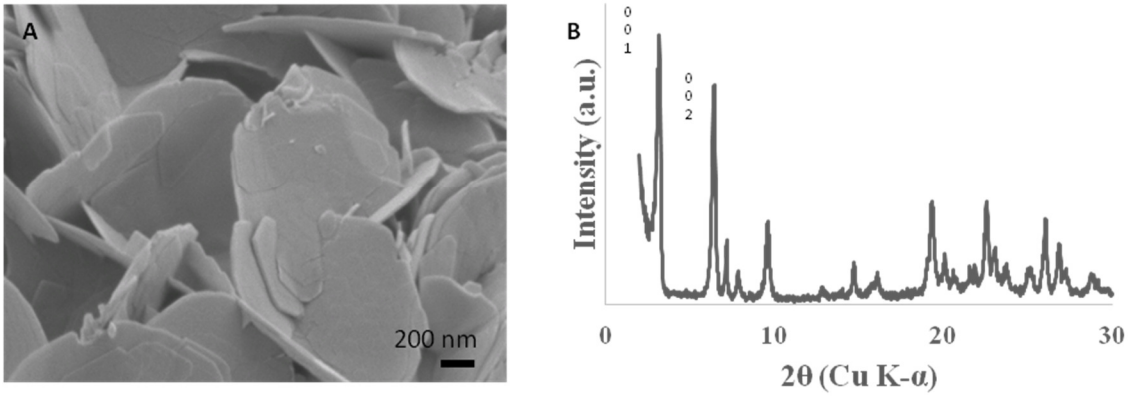

Fig 2.4. A: An SEM image of as-synthesized ITQ-1 platelets showing a highly intergrown morphology. B: Powder XRD pattern of as-synthesized ITQ-1 platlets.

2.2.3 Preparation of Coating Suspension of ITQ-1 Platelets

As-synthesized ITQ-1 particles were inter-grown as large spherical particles (Fig. 2.2A and 2.3A). Due to their poor packing efficiency, these large spherical particles are not suitable for the fabrication of thin, compact ITQ-1 films on the PSS supports. To break apart the inter-grown layers, the ITQ-1 platelets were dispersed in water to make a 5% (w/w) suspension. The suspension was sonicated in a bath sonicator (Branson 5510R-DTH, 135 watts) for several hours. Bath sonication was effective in breaking the platelet intergrowth. The yield of the segregated platelets increased with increasing the sonication time. After 7 hours of the bath sonication treatment, the resulting ITQ-1 suspension was centrifuged at 300 relative centrifugal force (RCF) for 10 minutes to sediment and remove the inter-grown particles from the segregated platelets. The segregated platelets were

centrifuged at 10000 RCF for 10 minutes. This cake formed after centrifugation was re-dispersed in a specific amount of water to obtain the desired concentration of ITQ-1 platelets. Thermogravimetric (TGA) analysis was done on the ITQ-1 suspension to confirm the concentration of ITQ-1 platelets in the suspension. Fig. 2.3B shows a film of the segregated ITQ-1 platelets on a carbon tape mounted on a flat stainless steel support. The film was prepared by drying a drop of platelet suspension on a carbon tape at 70℃. Due to their high aspect ratio, ITQ-1 platelets packed well and oriented themselves flat on the support. This affirmed the suitability of ITQ-1 platelets for making a thin, compact film on the porous stainless steel supports.

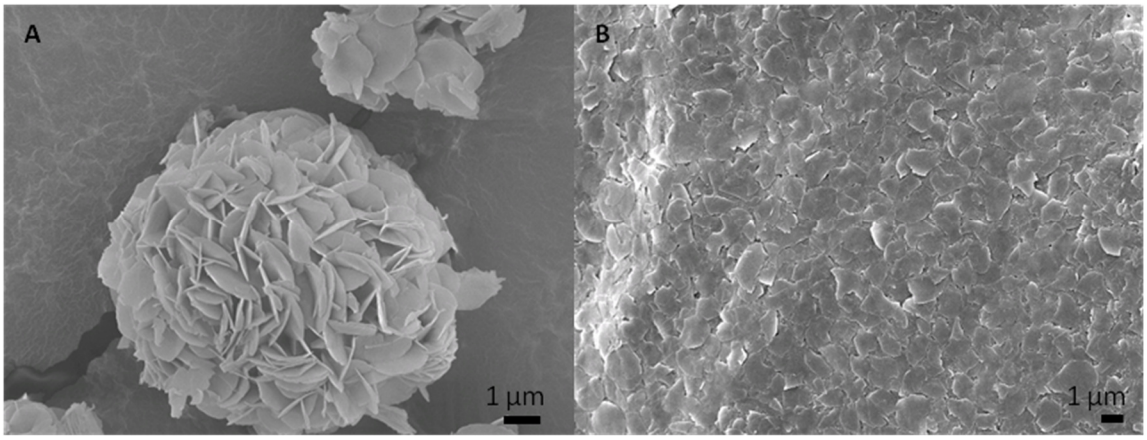

Fig 2.5. A: An SEM image of as-synthesized ITQ-1 platelets. Platelets have intergrown to form large spherical particles. B: An oriented ITQ-1 film prepared from a suspension of segregated ITQ-1 platelets.

2.3 Dip Coating of ITQ-1 Platelets on the Porous Stainless Steel Tubes

Porous Stainless Steel (PSS) tubes from Pall Inc. were used as the high throughput substrates for the fabrication of the thin ITQ-1 films. These tubes were fabricated by sintering of SS 316 powder with a particle size range of 10-20 µm. The tube consisted of two inches long PSS media connected on either end by one inch long non-porous stainless steel tube (Fig. 2.4A). The outer diameter of the tube was 10 mm. The PSS tubes had a high surface roughness as the pore openings were as big as 20 µm (Fig. 2.4B). The SEM of the cross section of the PSS tube revealed that they had a symmetric structure with their wall thickness close to 1 mm (Fig 2.4C).

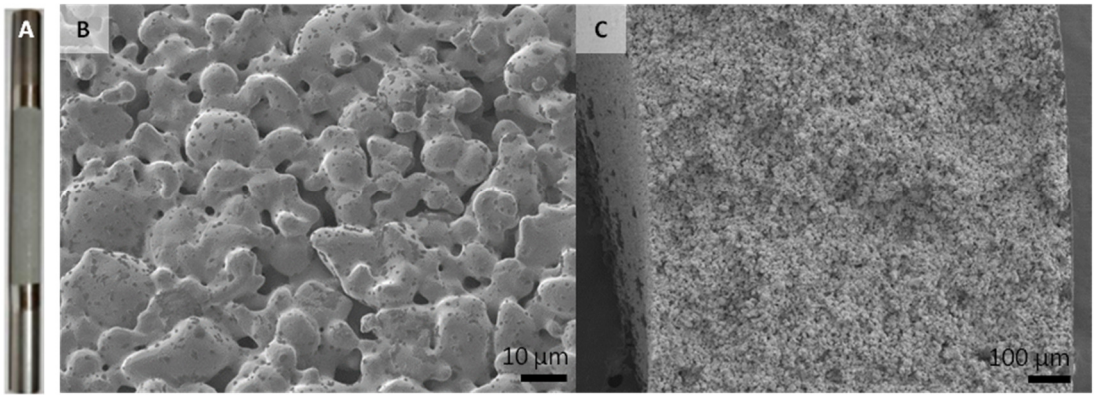

Fig 2.6. A: Picture of the PSS tube. B: Surface morphology of the PSS tubes revealing 10-20 µm pore opening. C: Cross section of the PSS tubes revealing their symmetric structure.

One of the most popular methods to make a uniform coating on a large surface is dip coating[52]. Dip coating is a simple and easy to implement technique. Dip coating has been used commercially for fabrication of large scale coatings on various substrates. In the dip coating process, a substrate is dipped inside the coating suspension for a specific period. Then, the substrate is pulled out of the coating suspension at a controlled velocity. The substrate coming out of the coating suspension pulls out a film of the coating suspension due to a viscous drag experienced by the coating suspension. Some of the coating suspension flow downwards due to the gravitational pull. The shear force due to the downward flow of the suspension often helps in orienting the anisotropic particles. As the solvent evaporates, the colloidal particles are trapped at the receding air-solvent interface, and are subsequently deposited on the surface of the substrate.[53, 54] The thickness of the wet dip coated film is determined by gravity, the viscosity of the suspension, and the surface tension of the solvent.[55] The film thickness during the dip coating of porous substrates is determined by dip coating effects as well as capillary infiltration effects.

Dip coating of a plate was first experimentally studied by Goucher and Ward in 1922.[56] Very first theoretical calculations on dip coating of flat plate was done by Landau and Levich, who showed that wet film thickness is a function of surface tension, viscosity and gravity (Equation 2.1).[57]

Equation 2.1

$$\frac{T}{\left(1-T^2\right)^{2/3}} = 0.944\,Ca^{1/6}$$

where,

$$T = \text{film thickness} = \frac{h}{\left(\frac{\eta V}{\rho g}\right)^{1/2}}$$

$$Ca = \text{capillary number} = \frac{\eta V}{\gamma_{LV}}$$

For dip coating of rods and tubes in a low capillary number system, modified Landau Levich Equation was proposed (Equation 2.2)[58]:

$$h = \sqrt{\frac{\gamma_{LV}}{\rho g}}\,Ca^{2/3}\left\{\frac{1.338}{\sqrt{\frac{\gamma_{LV}}{\rho g R^2}+\frac{1.414}{1+0.44\left(\frac{\gamma_{LV}}{\rho g R^2}\right)^{0.44}}}}\right\}$$

Equation 2.2

where,

$h = \text{coating thickness}$

$R = \text{radius of the SS tube}$

If the Bond number (Bo = $\rho gr^2/\gamma$) for a tube is greater than 1, then the flat plate correlation for dip coating (Equation 2.1) can be applied for tubes[55, 58, 59]. For the PSS tubes from Pall Inc., the Bond number was 3.41. Hence, the flat plate correlation developed by Landau and Levich can be applied to the SS tubes. As evident from the Equation 2.1, increasing the withdrawal velocity increases the coating thickness. Other parameters like viscosity, density and radius are fixed for a given composition of the coating suspension.

For the coating of PSS tubes, a 3.65% (w/w) suspension of ITQ-1 in water was used. When dip coating of the PSS tube (V = 4.5 cm/s, Ca = 6.38 x 10^{-4}) was performed

with both ends of the tube open, both the internal as well as the external walls of the PSS tube were coated (Fig. 2.5 A, B, C and D). Coating on both walls of the PSS tube is not desirable as it will lead to a reduction in the flux of the gases through the PSS tube. Pinhole defects (a few uncoated pore channels) were also present on the surface of the PSS tube, indicating that the coating was not uniform.

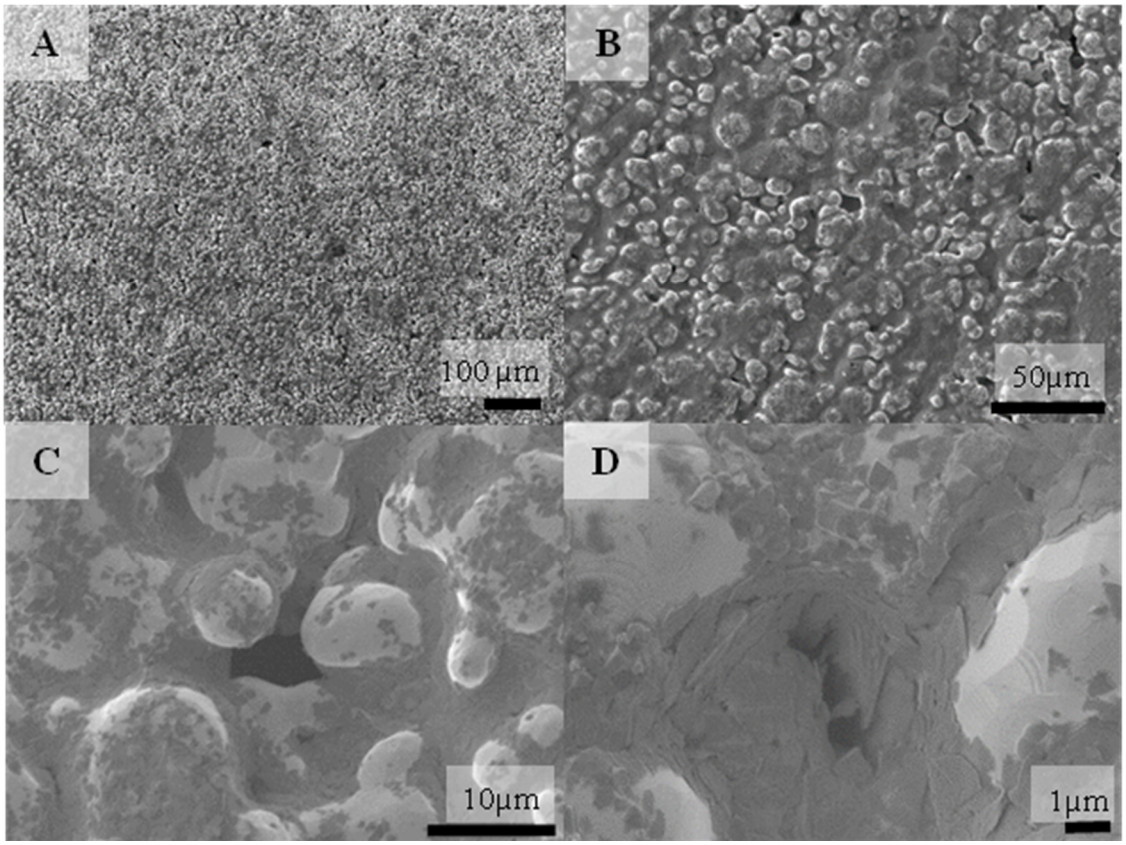

Fig 2.7. SEM images of the surface of a PSS tube dip coated with 3.65% (w/w) suspension of ITQ-1 platelets, while keeping both ends of the tube open.

To prevent coating on the internal wall of PSS tubes, the ends of PSS tubes were sealed before dip coating. Dip coating in this manner (V = 13.8 cm/s, Ca = 2.5 x 10^{-3}) coated a visibly thin, non-uniform coating (Fig. 2.6 A and B). Many of the tube pore openings did not get coated. This could be due to infiltration of the dip coated film inside the pores of the tubes. This is one of the most challenging problems, especially for the coating of porous substrates with relatively large pore openings. One potential solution to

prevent the infiltration of the coated film is masking the support[60], but it is time consuming and difficult to scale up.

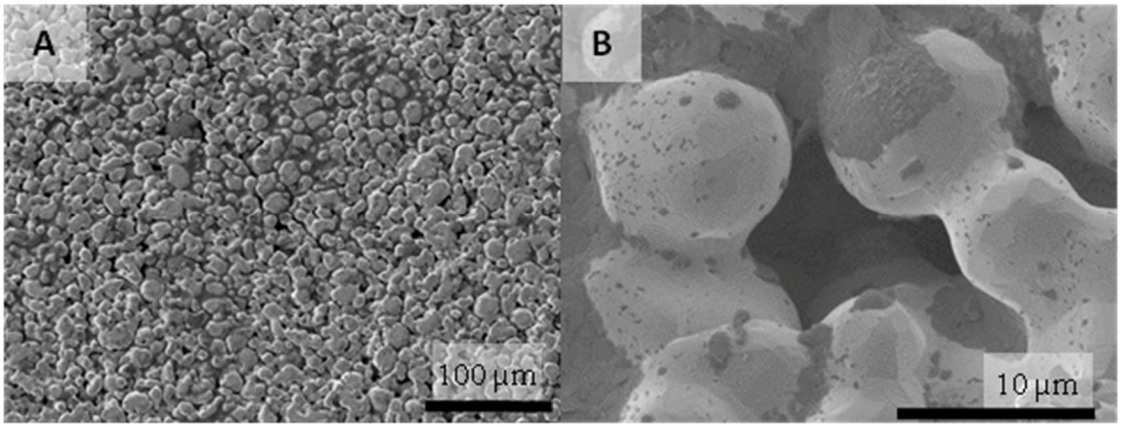

Fig 2.8. SEM images of the surface of a PSS tube dip coated with 3.65% (w/w) suspension of ITQ-1, while keeping both ends of the tube closed.

Infiltration of the coating suspension can be reduced by increasing the viscosity of the coating suspension. Adding a binder such as poly(vinyl alcohol) (PVA) not only increases the viscosity, but also acts to prevent crack formation in the film during heat treatment of the coating.[61] Heat treatment of the coating is a necessary step to remove the OSDA from the zeolite platelets. Heat treatment also promotes bonding between the ITQ-1 platelets by the condensation of the terminal silanol groups. Based on this, PVA was added to the coating suspension of the ITQ-1 platelets. The coating suspension after the addition of PVA consisted of 2.6% (w/w) ITQ-1 and 5% PVA. Fig. 2.7 shows the coating of the PSS tubes with this suspension at the dip coating velocities of 0.2 cm/s and 40 cm/s. As expected, the ITQ-1 film was thicker compared to that prepared using the coating suspension without PVA. However, the film fabricated by dip coating at 0.2 cm/s had many pinhole defects (Fig 2.7 A and B). The film fabricated at a higher velocity (40 cm/s) was more uniform (Fig. 2.7C), but still had a few pinholes (Fig. 2.7 D). These large pinhole defects are detrimental to membrane performance as most of the molecular transport will occur through these pinholes.

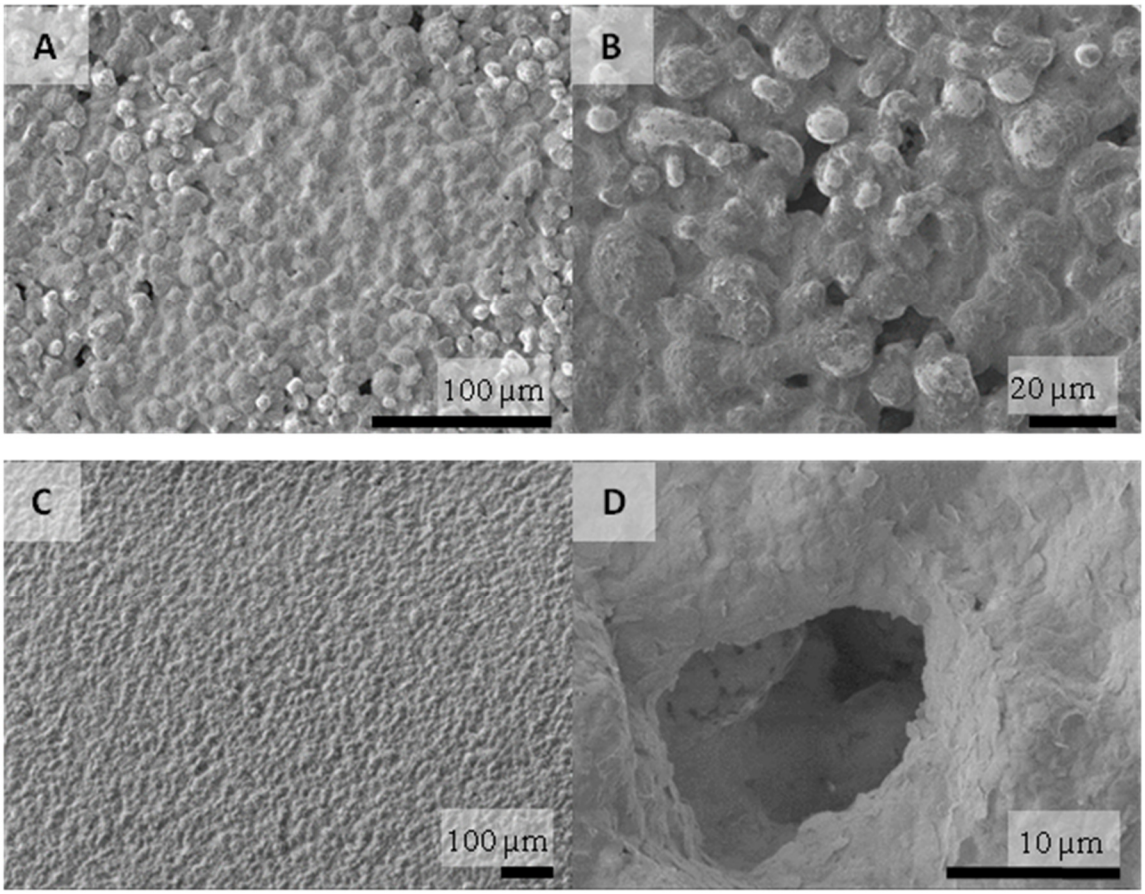

Fig 2.9. SEM images of various coatings. A, B: ITQ-1 film made by dip coating of the PSS tube with ITQ-1/PVA suspension at 0.2 cm/s. C, D: ITQ-1 film by dip coating at 40 cm/s. ITQ-1 films were heat treated at 540℃ for 6 hours before SEM imaging.

One of the strategies to eliminate pinholes is repeated dip coating. However, repeated coatings of the PSS tube with PVA containing ITQ-1 suspension led to a very thick film of ITQ-1, which peeled off during the heat treatment step. The thickness of the film deposited by a single dip coating step is limited by the maximum allowable dip coating velocity, which was 40 cm/s. To make a thicker coating of the ITQ-1 platelets without encountering delamination issues, the viscosity of the coating suspension was increased by increasing the PVA content to 7.5%. A coating of this suspension (7.5% PVA, 2.5% ITQ-1) with a dip coating velocity of 15 cm/s (Ca = 1.46) led to a uniform coating without any pinhole defects (Fig. 2.8A). However, higher magnification SEM image (Fig. 2.8B) revealed that the ITQ-1 platelets on the surface of the coating were not oriented. This can

be attributed to the high viscosity of the coating suspension (~700 cP), which reduced the rotational degree of freedom of the ITQ-1 platelets.

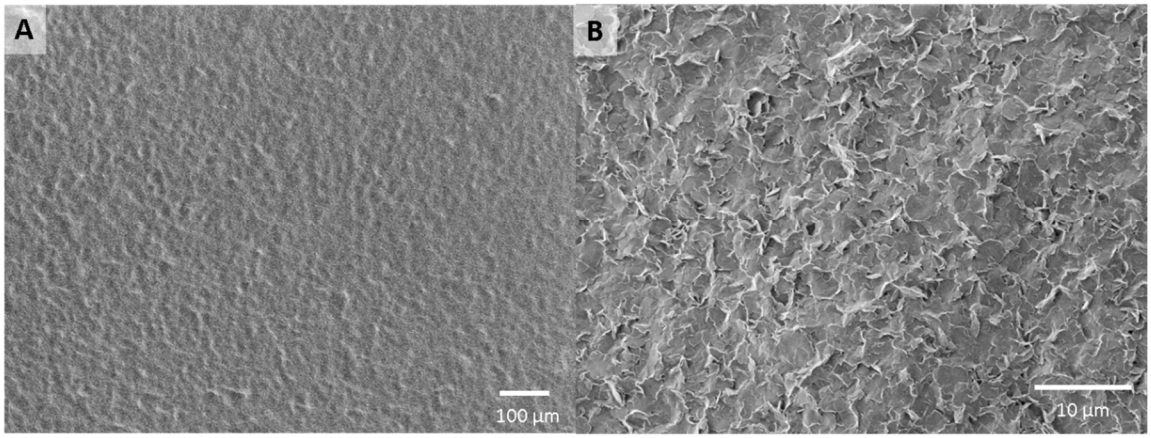

Fig 2.10. A: An SEM image showing complete coverage of the PSS tube by dip coating of 7.5% PVA, 2.5% ITQ-1 suspension at 15cm/s. B: The surface of the coating indicates non-oriented ITQ-1 platelets. The ITQ-1 film was heat treated at 540℃ for 6 hours before SEM imaging.

The non-oriented ITQ-1 film had many defects, potentially due to poor packing of the ITQ-1 platelets. Secondary growth of ITQ-1 on the non-oriented ITQ-1 seed layer is not preferable. A non-oriented seed layer will lead to a non-oriented membrane.[13] To improve the orientation of this film, another layer of ITQ-1 was coated on the top of this film to make a *c*-oriented ITQ-1 coating. This was achieved by dip coating the non-oriented ITQ-1 film on the PSS tube using a 3.6% (w/w) suspension of ITQ-1 (V= 0.8 cm/s) in water. Since, a thin, oriented coating of the ITQ-1 platelets was targeted, PVA was not added to the suspension. The ITQ-1 film (Fig. 2.9) thus prepared, did not peel off during the heat treatment. The ITQ-1 platelets conformed to the surface roughness of the PSS support and oriented themselves with their *c*-axis perpendicular to the support surface (Fig 2.9 B and C). A cross-section of this film revealed that the average thickness of the ITQ-1 film prepared in this way was approximately 10 µm. The ITQ-1 film thickness varied due to the surface roughness of the PSS support.

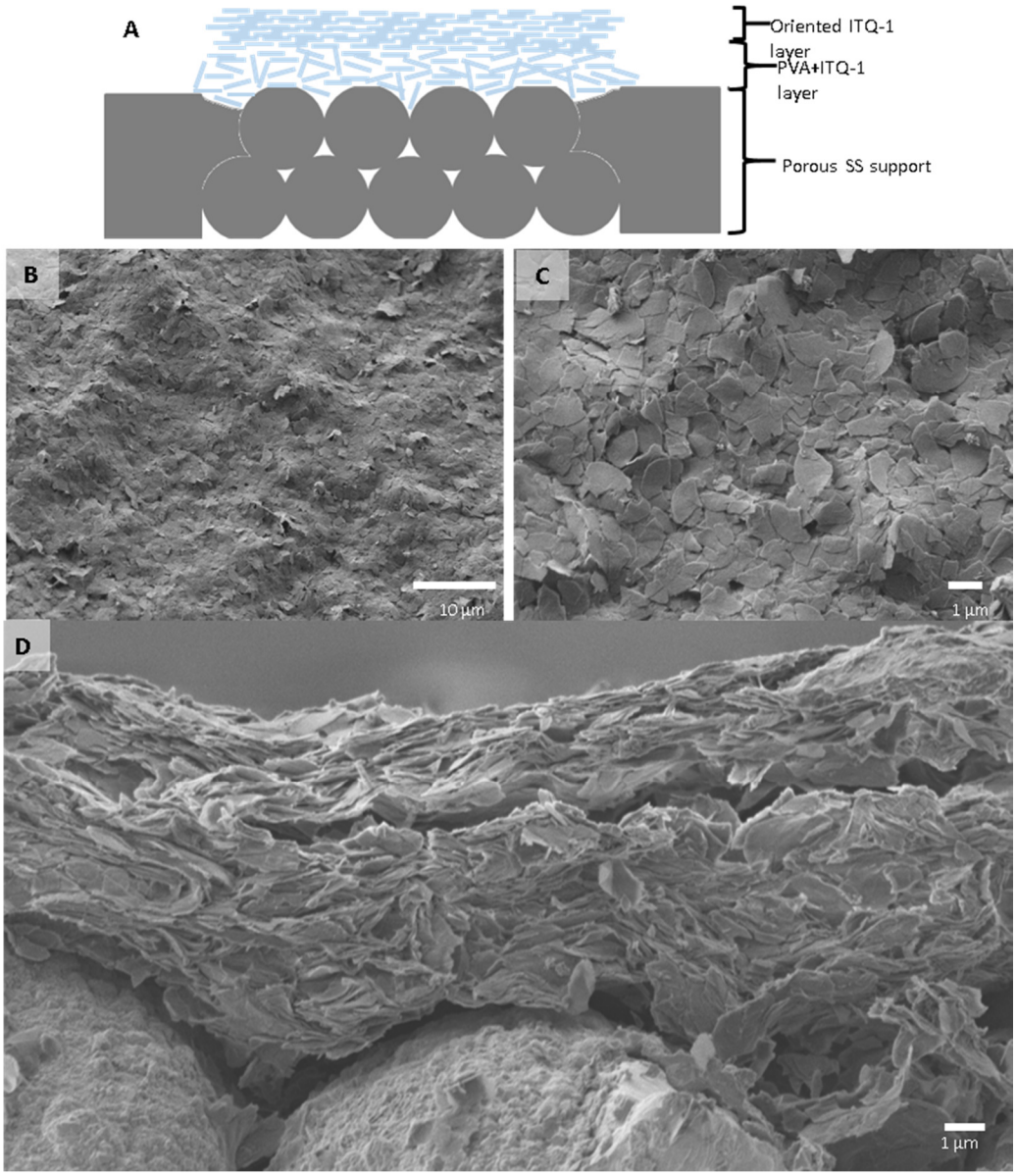

Fig 2.11. A: A schematic diagram of the coating of ITQ-1 platelets on PSS tube. B, C: SEM images of an oriented film of ITQ-1 platelets on the PSS tube. D: SEM image of the cross section of the PSS tube showing 10 µm thick film of ITQ-1 platelets.

2.4 Gas Permeation at High Temperature

Gas permeation tests were carried out to characterize the performance of the ITQ-1 film as a hydrogen selective membrane. Fig. 2.10 shows a schematic of the permeation setup in which the ITQ-1 membrane was heated in a tubular furnace. The preheated gases

(H_2, He, N_2, CO_2) were fed individually over the outer surface of the PSS tube at 1 atmospheric pressure while the inside of the tube (permeate side) was maintained at vacuum using a vacuum pump.[22] The permeate chamber had a fixed volume of 1 liter. The flux and permeance of each gas was calculated by measuring the rate of increase in pressure in the permeate side when the permeate side was isolated from the vacuum pump. The flux and permeance calculations were carried out assuming ideal gas equation (equation 2.3).

$$\text{Permeance} = \frac{V}{ART}\frac{dP}{dt} \qquad \text{Equation 2.3}$$

Where,

V = Volume of the permeate chamber

A = Area of the membrane

R = Gas constant

T = Temperature of membrane

$\frac{dP}{dt}$ = Rate of increase in pressure

The temperature dependence of the gas transport through the membrane was measured by varying the membrane temperature from 30°C to 600°C. (Table 2.1). As indicated by the ideal gas selectivity data in Table 2.1, transport of the gases through the ITQ-1 film was in the Knudsen regime.[62] In the Knudsen diffusion regime, permeance of the molecules through a porous film can be related to the temperature and the molecular weight of the molecule as following:

$$\text{Knudsen Permeance} = \frac{2\varepsilon\mu d}{3L}\sqrt{\frac{8}{\pi MRT}} \qquad \text{Equation 2.4}$$

Where,

ε = Porosity

μ = Shape factor = 1/τ, where τ = tortuosity

d = Pore diameter

L = Thickness of film

M = Molecular weight of the gas

R = Gas constant

T = Temperature

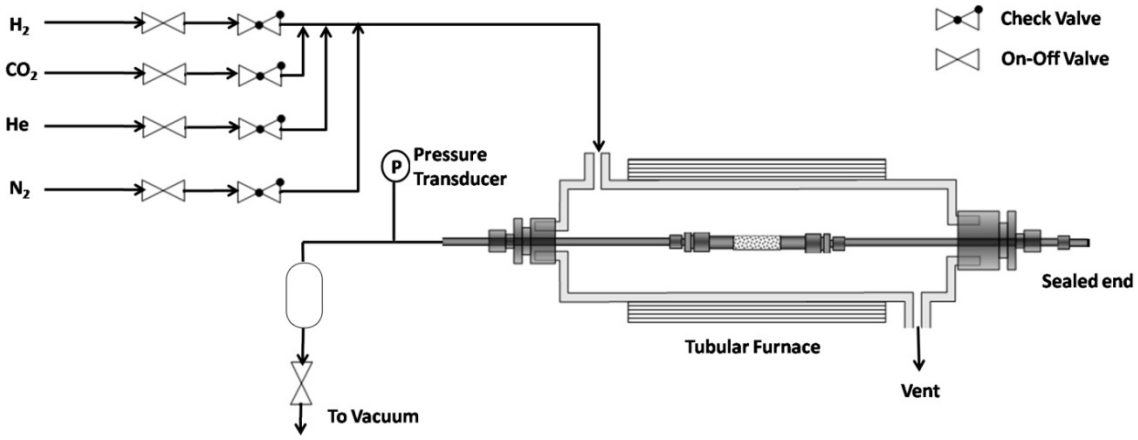

Fig 2.12. A schematic of the gas permeation setup.

Fig 2.11 shows a plot of the permeance of the ITQ-1 film vs. inverse of the square root of the permeation temperature. The linear dependence of permeance with inverse of the square root of temperature also confirms the Knudsen transport mechanism (Equation 2.4). Knudsen transport in the ITQ-1 film indicates that the ITQ-1 film had defects of a few nm in size. These defects could be due to the packing limitation of rigid ITQ-1 platelets especially on a rough support.

Table 2.2. Temperature dependence of the gas permeance and the selectivity of the ITQ-1 film on the PSS support. Knudsen selectivities are is listed in Italics.

					Gas Selectivity *(Knudsen in Italics)*			
Temperature	**Gas Permeance (mol/m^2-s-Pa)**				**H_2/He**	**H_2/CO_2**	**H2/N_2**	**CO2/N_2**
^{o}C	**H_2**	**He**	**N_2**	**CO_2**	*1.41*	*4.69*	*3.74*	*0.80*
215	3.9E-06	2.6E-06	1.3E-06	9.9E-07	1.47	3.83	3.11	0.81
310	3.1E-06	2.1E-06	9.6E-07	8.0E-07	1.46	3.84	3.19	0.83
505	2.1E-06	1.5E-06	6.6E-07	5.4E-07	1.45	3.90	3.21	0.82
594	1.8E-06	1.2E-06	5.6E-07	4.6E-07	1.46	3.92	3.21	0.82

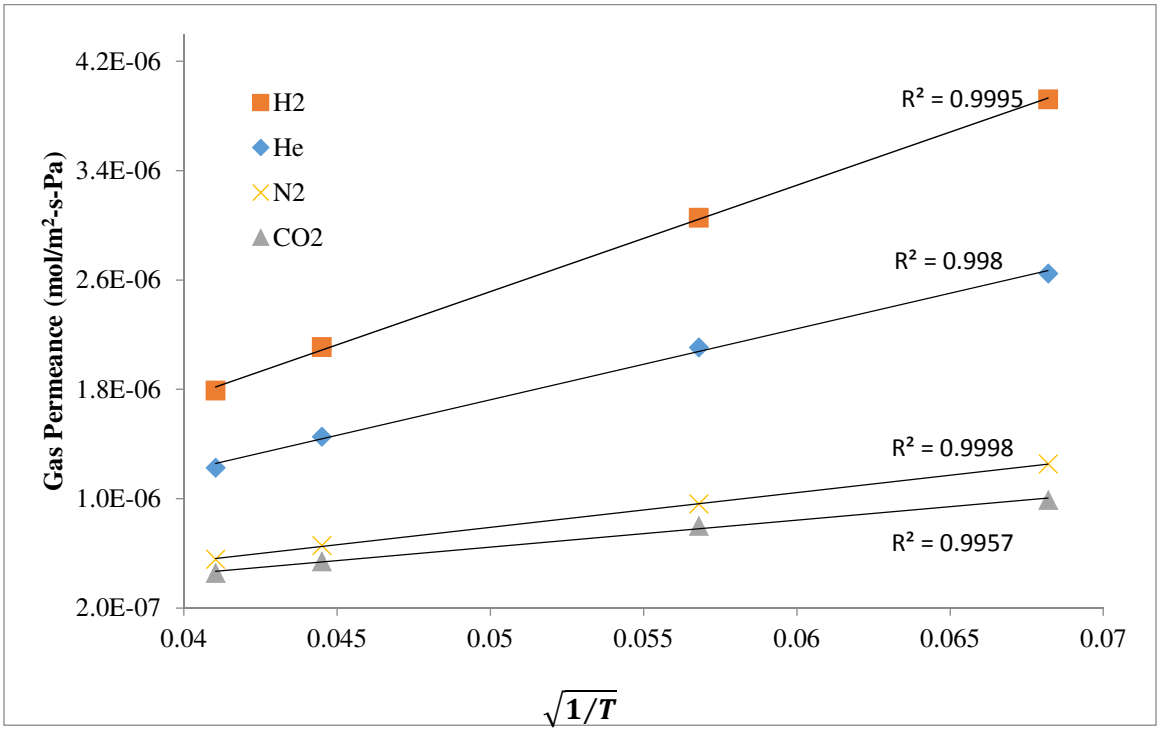

Fig 2.13. Permeance of the ITQ-1 film plotted against the inverse of square root of the permeation temperature.

2.5 Summary

ITQ-1 platelets with a lateral dimension of 1-3 µm were prepared by hydrothermal synthesis for coating of high throughput PSS tubes with a pore opening of 10-20 µm. A segregated suspension of the ITQ-1 platelets was obtained by sonicating as-made ITQ-1 particles, followed by the sedimentation of large inter-grown particles. Thin films of ITQ-1 platelets prepared by dip coating had many pinhole defects due to infiltration of the dip coated film into the PSS pores. Incorporation of a polymeric binder (PVA) in the coating suspension led to a pinhole free film; however, ITQ-1 platelets in the film were randomly oriented. The orientation of ITQ-1 platelets on the surface of the PSS support was improved by dip coating the randomly oriented film in an aqueous suspension of ITQ-1 platelets. Gas permeation studies on these oriented, crack free ITQ-1 films indicated Knudsen transport was the dominant diffusion mechanism. Films fabricated using this procedure separated H_2 from CO_2 with an ideal selectivity of 4, and H_2 permeance of 4 x 10^{-6} mole/m^2-s-Pa at 200

ºC. The film did not form cracks even at temperatures close to 600 ºC, making them attractive for molecular sieving at high temperature.

Chapter 3: Exfoliated Zeolite Nanosheets and Their Membranes

3.1 Introduction

High aspect ratio zeolite single crystals with thickness in the nanometer range (zeolite nanosheets), are desirable for applications including building blocks for heterogeneous catalysts[6-8] and the fabrication of thin molecular sieve films and nanocomposites for energy efficient separations.[63] They could also be of fundamental importance probing mechanical, electronic, transport and catalytic properties of microporous networks at the nanoscale.[2, 12] Despite the steady advances in the preparation and characterization of layered materials containing microporous layers and of their pillared and swollen analogues[6-8, 33, 64-73], the synthesis of suspensions containing discrete, intact, non-aggregated zeolite nanosheets has proven elusive due to structural deterioration and/or aggregation[44] of the lamellae upon exfoliation. Here, we report the isolation and structure determination of highly crystalline zeolite nanosheets of the MWW and MFI structure type and demonstrate the use of their suspensions in the fabrication of zeolite membranes.

3.2 Experimental Material and Methods

3.2.1 Synthesis of ITQ-1

ITQ-1 was synthesized following the protocols reported by Camblor et al. using N,N,N-trimethyl-1-adamantammonium hydroxide (TMAdaOH).[50] TMAdaOH was obtained by alkylation of 1-adamantylamine (Aldrich) with excess of methyl iodide (Aldrich) at room temperature followed by ion exchange of the iodide salt. For the

synthesis of ITQ-1, fumed silica (Cab-O-Sil M5, Cabot Corp.) was mixed with TMAdaOH, hexamethyleneimine (HMI) (Aldrich), NaCl (Aldrich) and distilled water to obtain a gel composition of SiO_2 : 0.25 TMAdaOH : 0.31 HMI : 0.20 NaCl : 44 H_2O. After stirring for 5 hours at room temperature, the resultant gel was transferred to a rotating Teflon-lined steel autoclave at 150 °C. Crystallization was stopped after 5 days and the product was obtained by centrifugation. The cake was washed with distilled water to reduce the pH to 9 and dried in a vacuum oven at 130 °C.

3.2.2 Swelling of ITQ-1

ITQ-1 was swollen with cetyltrimethylammonium bromide (CTAB) at room temperature using the swelling protocol of MCM-22(P) as reported by Maheshwari et al.[44] Typically, 1.8 g of ITQ-1 powder was mixed with 35.0 g of an aqueous solution of 29 wt% CTAB (Sigma-Aldrich) and 11.0 g of an aqueous solution of tetrapropylammonium hydroxide (TPAOH) (40% (w/w), Alfa Aesar). The mixture was stirred at room temperature for 16 hours, after which the swollen ITQ-1 was recovered by centrifugation. Excess CTAB and TPAOH were removed by washing the obtained cake with 9 liters of water. The resultant cake was dried in a vacuum oven at 130 °C.

3.2.3 Synthesis of multilamellar silicalite-1

Multilamellar silicalite-1 was synthesized using the diquaternary ammonium surfactant $[C_{22}H_{45}\text{-}N^+(CH_3)_2\text{-}C_6H_{12}\text{-}N^+(CH_3)_2\text{-}C_6H_{13}](OH)_2$ or $C_{22}\text{-}6\text{-}6(OH)_2$ as reported by Choi et al.[8] $C_{22}\text{-}6\text{-}6Br_2$ was synthesized by alkylation of N,N,N',N'-tetramethyl-1,6-hexanediamine with 1-bromodocosane at 70 °C followed by alkylation of the resultant product by 1-bromohexane at 85 °C. $C_{22}\text{-}6\text{-}6(OH)_2$ was obtained by ion exchange of the bromide salt. For the synthesis of multilamellar silicalite-1, tetraethyl orthosilicate (TEOS) (Aldrich) was hydrolyzed in the presence of $C_{22}\text{-}6\text{-}6(OH)_2$ and distilled water to obtain a gel composition of 100 SiO_2 : 15 $C_{22\text{-}6\text{-}6}(OH)_2$: 4000 H_2O: 400 EtOH. After hydrolysis for 24 hours at room temperature, the resultant gel was transferred to a rotating Teflon-lined steel autoclave at 150 °C. Crystallization was stopped after 5 days and the product was

obtained by centrifugation. The cake was washed with distilled water to reduce the pH to 9 and dried in a vacuum oven at 130 °C.

3.2.4 Exfoliation of CTAB swollen ITQ-1 and multilamellar silicalite-1 to obtain MWW- and MFI-nanosheet nanocomposite, respectively

Both layered zeolites were exfoliated by melt compounding to obtain polymer-zeolite nanocomposite as reported by Maheshwari[44, 45]. In a typical exfoliation process, 3.84 g of polystyrene (M_w = 45000 g/mol) and 0.16 g of the dried zeolite (CTAB swollen ITQ-1 or multilamellar silicalite-1) were manually mixed and loaded in a vertical, co-rotating twin screw extruder with a recirculation channel (DACA mini compounder). The mixture was blended sequentially at 120 °C for 20 min, 170 °C for 25 min, 150 °C for 30 min and 200 °C for 20 min under a nitrogen environment and at a screw speed of 300 rpm. The MWW- and MFI-nanosheet nanocomposites were then extruded out at 150 °C.

3.2.5 Preparation of coating suspensions of MWW- and MFI-nanosheets

Coating suspensions were created by dissolution of the exfoliated zeolite-polymer nanocomposite in toluene followed by dispersion and purification. Typically, 0.10 g of the nanocomposite was dissolved in 8.00 g toluene to make a suspension containing 1.25% polymer (w/w) and 0.05% zeolite (w/w). The suspension was sonicated for 1 hour in a Branson 5510R-DTH ultrasonic cleaner at room temperature to disperse the exfoliated zeolite nanosheets in toluene. The resultant dispersions for MFI- and MWW-nanosheets were centrifuged (12000 and 13250 relative centrifugal force (RCF) for 10 and 15 min, respectively) to settle down the larger un-exfoliated particles. The solution containing the exfoliated nanosheets was then pipetted out from the centrifuge tube and used as coating suspension.

3.2.6 Coating of nanosheets on Anopore and α-alumina disk

The anodized alumina membrane (Anopore, pore size 200 nm, diameter 13 mm, PCG Scientifics) was coated by 1.5 g of the coating suspension by vacuum filtration using a Millipore Swinnex filter holder (13 mm). Similarly, homemade α-alumina disks[74] were

coated by 4.00 g of MWW-nanosheet suspension or 3.00 g of MFI-nanosheet suspensions. The coated nanosheets of MFI on the Anopore and the α-alumina disks were calcined at 540 °C for 6 hours and MWW coating was calcined at 580 °C for 4 hours to remove residual polymer and structure-directing agents.

3.2.7Secondary growth of MFI-nanosheet films on the α-alumina disk

The MFI-nanosheet coating on the α-alumina disk was hydrothermally grown to reduce inter-particle gaps. In a typical secondary growth, TEOS (Aldrich) was hydrolyzed for 4 hours at room temperature in the presence of TPAOH (1.0 M, Aldrich) and distilled water to obtain a synthesis sol with a composition of 60 SiO_2 : 9 TPAOH : 8100 H_2O : 240 EtOH. The synthesis sol was aged at 90 °C for 6 hours in a Teflon-lined autoclave. Then, the MFI-nanosheet coating was placed vertically in this aged sol, and heated at 90 °C for 4.5 hours in a Teflon-lined autoclave. The membrane was then calcined at 480 °C for 4 hours with temperature ramp rate of 0.5°C/minute to remove the TPAOH from the framework.

3.3 Characterization

A FEI Tecnai T12 transmission electron microscope (TEM) operated at 120 kV and a FEI Tecnai G^2 F30 TEM operated at 300 kV were used for TEM studies. All images were recorded using CCD cameras. 50 nm thin sections of the nanocomposites were prepared by a Leica EM UC6 Ultramicrotome equipped with a diamond knife. The sections were then mounted on a TEM grid (400 mesh Cu, PELCO). For examining morphology of the nanosheets and high-resolution TEM, a drop of nanosheets suspension in toluene was deposited on a TEM grid (ultrathin carbon film on holey carbon support film, 400 mesh Cu, Ted Pella) and was air-dried.

For AFM, muscovite mica was etched in 50% HF for 4 hours to generate the 2.0 and 1.0 nm steps[75], which were used as a standard in determining the nanosheet thickness. Nanosheet specimens for AFM were prepared by placing a drop of their suspension on freshly cleaved muscovite mica followed by calcination in air at 540°C for 6 hours. A

Molecular Imaging PicoPlus scanning probe microscope (since renamed Agilent 5500 AFM/SPM system) was used for imaging. AFM tips were used as obtained from AppNano (Fort-10, Si, N type, uncoated). AFM was done in tapping mode in the repulsive regime. The image analysis was performed with the Gwiddion 2.22 software.

X-ray diffraction (XRD) patterns were collected using a Bruker-AXS (Siemens) D5005 diffractometer using CuKα radiation. Small angle XRD measurements were done on a homemade pinhole diffractometer using CuKα radition. Scanning electron microscopy (SEM) was done using a Hitachi S-900 instrument after the samples were coated with 3 nm of platinum. Cross section of the supported films for SEM and TEM were prepared using a focused ion beam (FIB) SEM instrument (Quanta 3D DualBeam). N_2 adsorption-desorption isotherms were collected at 77 K on an Autosorb iQ-Chemi system (Quantachrome Instruments). Micropore volume was extracted by conventional t-plot method (thickness 3.7-5Å) and BET surface area was calculated in the relative pressure range of 0.05-0.3. ^{29}Si MAS NMR spectrum was obtained from a Bruker DSX-500 solid state NMR spectrometer.

Xylene isomer vapor permeation measurements were made in the Wicke-Kallenbach mode (stainless steel permeation cell fitted inside a Thermolyne 48000 furnace) using 180 ml/min of Helium carrier containing equimolar feed of *p*-xylene (0.5 KPa) and *o*-xylene (0.5 KPa).[74] The separation factor is defined as the molar ratio of isomers in the permeate over the molar ratio in the feed.

3.4 Results and Discussion

MWW- and MFI-nanosheets were prepared starting from their corresponding layered precursors ITQ-1[6] and multilamellar silicalite-1[8], respectively. Prior to exfoliation by melt blending with polystyrene (M_W = 45000 g/mol), ITQ-1 was swollen following a previously reported procedure[44], while multilamellar silicalite-1 was used as-made. Melt blending was performed under nitrogen environment in a co-rotating twin screw extruder with a recirculation channel.[45] The polystyrene nanocomposites obtained by melt blending were characterized by X-ray diffraction (XRD) and microtomed sections were imaged by

transmission electron microscopy (TEM) to reveal the presence of exfoliated MWW- and MFI-nanosheets embedded in the polymer matrix (Fig. 3.1 and 3.2).

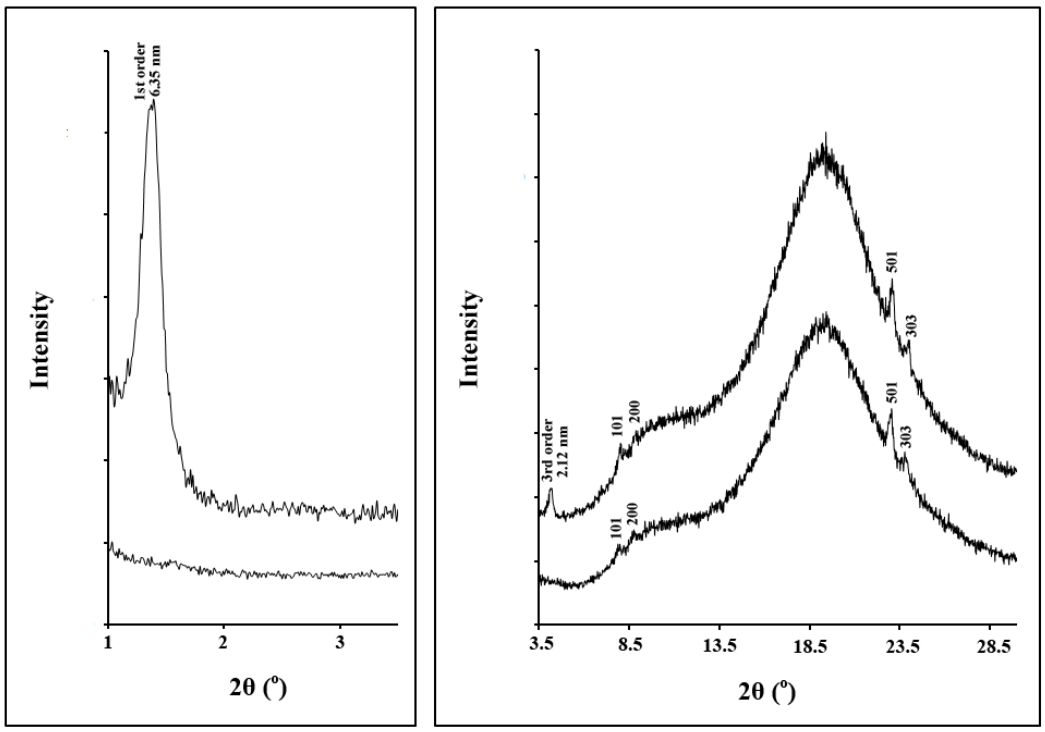

Fig 3.1. XRD patterns at small (left) and wide (right) angles from a polystyrene/layered MFI nanocomposite before (upper trace) and after (lower trace) melt blending. The 1st and the 3rd order reflections of the layered structure disappear after melt blending indicating exfoliation, while the higher angle peaks remain unchanged indicating structure preservation during exfoliation. The absence of the 2nd order reflection of the layered structure has been addressed before[37]. The broad underlying peaks are due to polystyrene.

To obtain a dispersion of these nanosheets, the nanosheet-polystyrene nanocomposites were placed in toluene and sonicated. After polymer dissolution and removal of larger particles by centrifugation, the dispersions, containing approximately 1.25% w/w polymer and 0.01% w/w nanosheets, were used to prepare samples for TEM and atomic force microscopy (AFM) examination, by drying a droplet on TEM grids and freshly cleaved mica surfaces, respectively (AFM sample calcined in air at 540 ^{0}C to remove polymer). Low magnification TEM images of high aspect ratio MWW- and MFI-nanosheets reveal their flake–like morphology (Fig. 3.3 A and B). The uniform contrast from isolated nanosheets suggests uniform thickness, while the darker areas can be attributed to overlapping of neighboring nanosheets. Although lattice fringes are not easily

visible in the high resolution TEM (HRTEM) images of the nanosheets (Fig. 3.4 A and B), they do exist, as confirmed by their fast Fourier transform (FFT) (Fig. 3.4 C and D). In addition, electron diffraction (ED) from a single MWW- and MFI-nanosheet (Fig. 3.3 C, D, E and F) and XRD data obtained from calcined powders of MWW- and MFI-nanosheets (Fig. 3.5 A and B) confirm that the nanosheets are highly crystalline materials of the MWW and MFI type, respectively. The thin dimensions of MWW- and MFI-nanosheets, as expected, are along the *c*- and *b*- axes, respectively, as indicated from the FFT of the HRTEM images and the ED data.

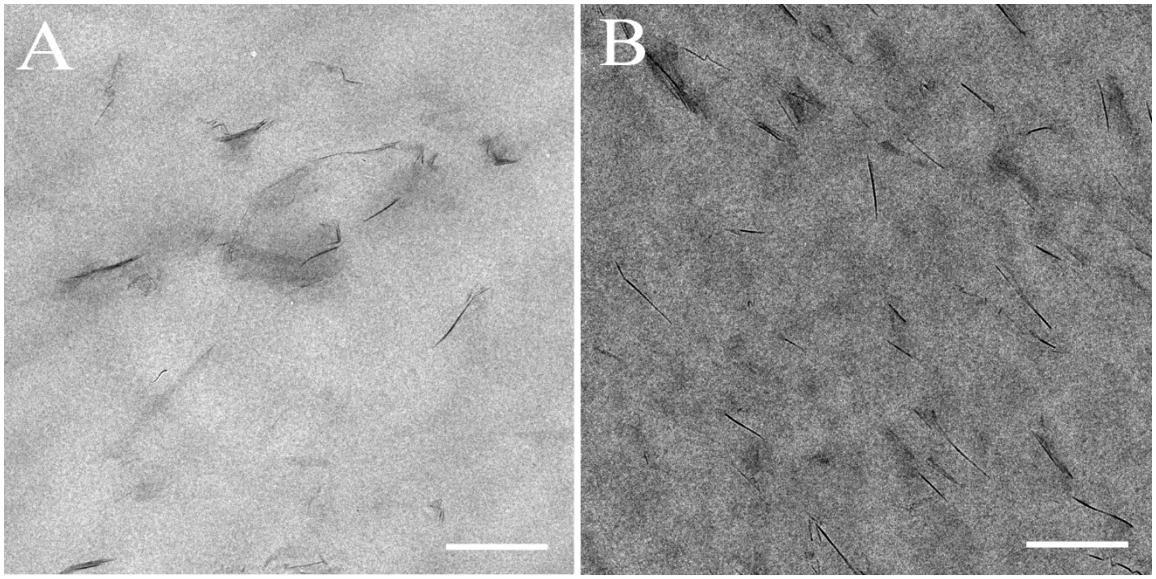

Fig 3.2. TEM images of thinly sectioned (microtomed) nanosheet-polystyrene nanocomposites prepared by melt compounding. A: MWW-nanosheets. B: MFI-nanosheets in polystyrene matrix. The scale bars indicate 200 nm.

AFM measurements, calibrated using steps formed on freshly cleaved mica[75], revealed remarkable uniformity in nanosheet thickness: 2.6±0.3 and 3.4±0.3 nm for the MWW- and MFI-nanosheets, respectively (Fig. 3.5 C, D, E and F). The MWW-nanosheet thickness is close to the one expected from the thickness of the ITQ-1 layers[7]. The MFI-nanosheet thickness, determined by AFM is consistent with 1.5 unit cells along the *b*-axis. Further examination of the HRTEM images collected here (Fig. 3.6) and of the images reported by Choi et al.[8] in conjunction with the thickness determined by the AFM suggests the presence of three complete pentasil chains running along the nanosheets. A $Q^3/(Q^3+Q^4)$

ratio of 11% is estimated for 1.5 unit cell thick MFI, which is in agreement with the ^{29}Si MAS NMR data (Fig. 3.7).

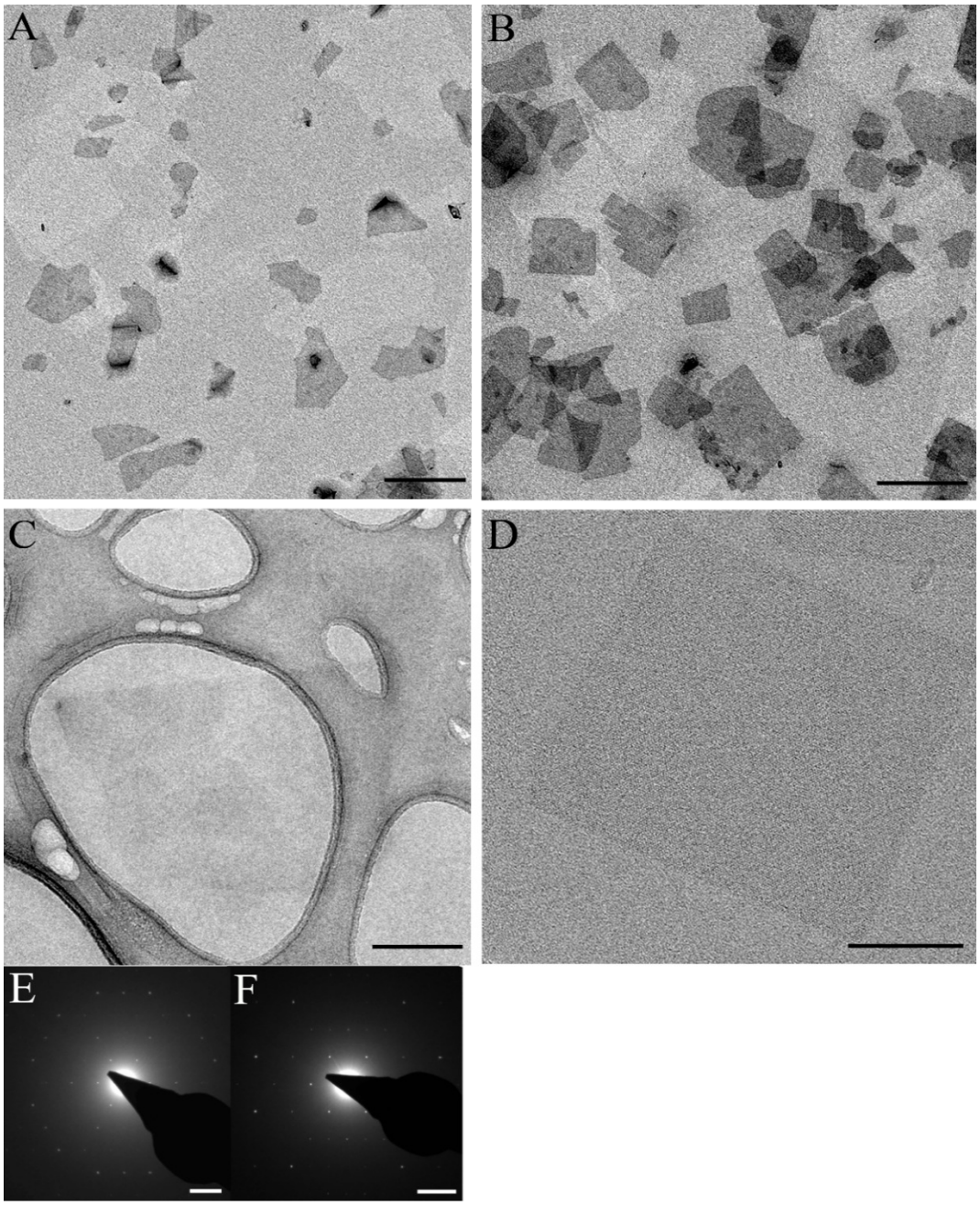

Fig 3.3. A: Low-magnification TEM images of *c*-oriented MWW-nanosheets. B: TEM images of *b*-oriented MFI-nanosheets. C: TEM images of single MWW- nanosheets. D: TEM images of a single MFI-nanosheet. (E) and (F) are the corresponding ED patterns of the same particles shown in (C) and (D), respectively. Scale bars indicate 200 nm for (A), (B) and (C), 50 nm for (D) and 1 nm^{-1} for (E) and (F).

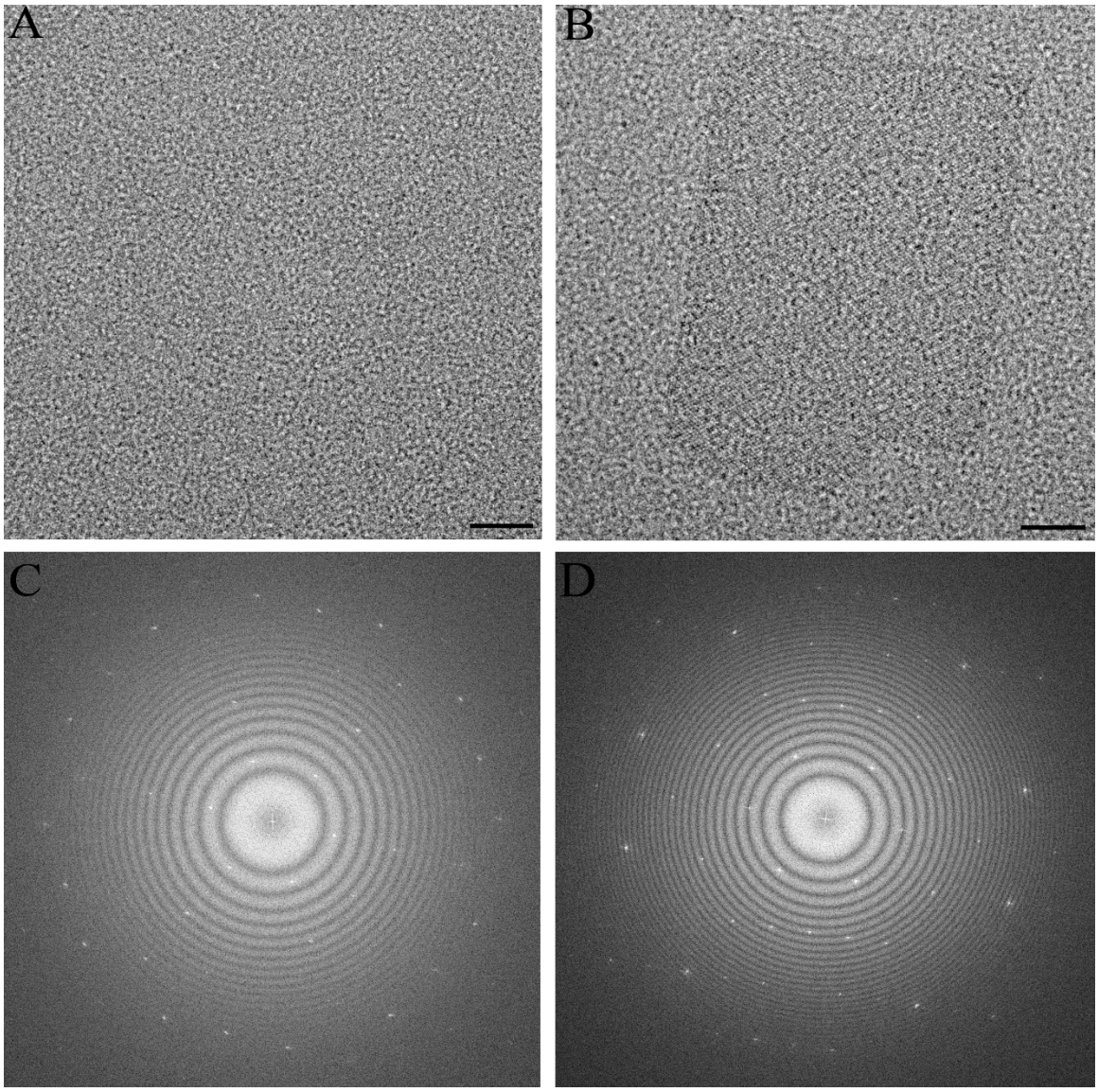

Fig 3.4. HRTEM images of nanosheets and corresponding fast Fourier transform (FFT). A: HRTEM image of an MWW-nanosheet. B: HRTEM image of an MFI-nanosheet. C: FFT of (A). D: FFT of (B). The scale bars in (A) and (B) indicate 20 nm.

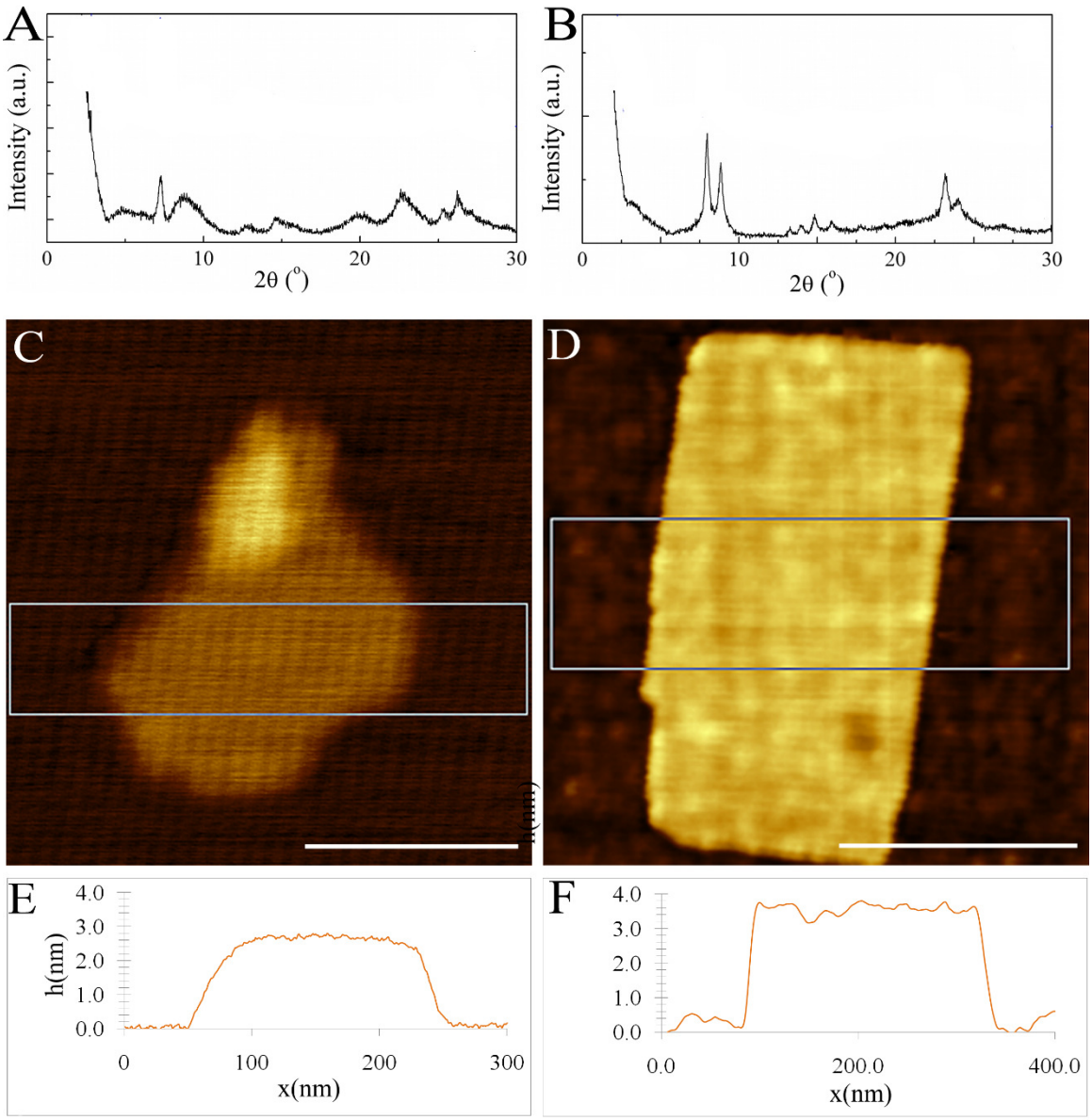

Fig 3.5. Powder XRD pattern (Cu Kα source, λ = 1.5418 Å) from MWW-nanosheets (A) and MFI-nanosheets (B). The powder for XRD were obtained by calcination of the nanosheet-polystyrene nanocomposite at 540 ^{0}C. AFM (tapping mode) topographical images of MWW- and MFI-nanosheets are shown in (C) and (D), respectively. Average step height data of the area highlighted in (C) and (D) is plotted in (E) (MWW-nanosheet) and (F) (MFI-nanosheet). The height data is calibrated using steps formed on freshly cleaved mica. The scale bars in (C) and (D) indicate 200 nm.

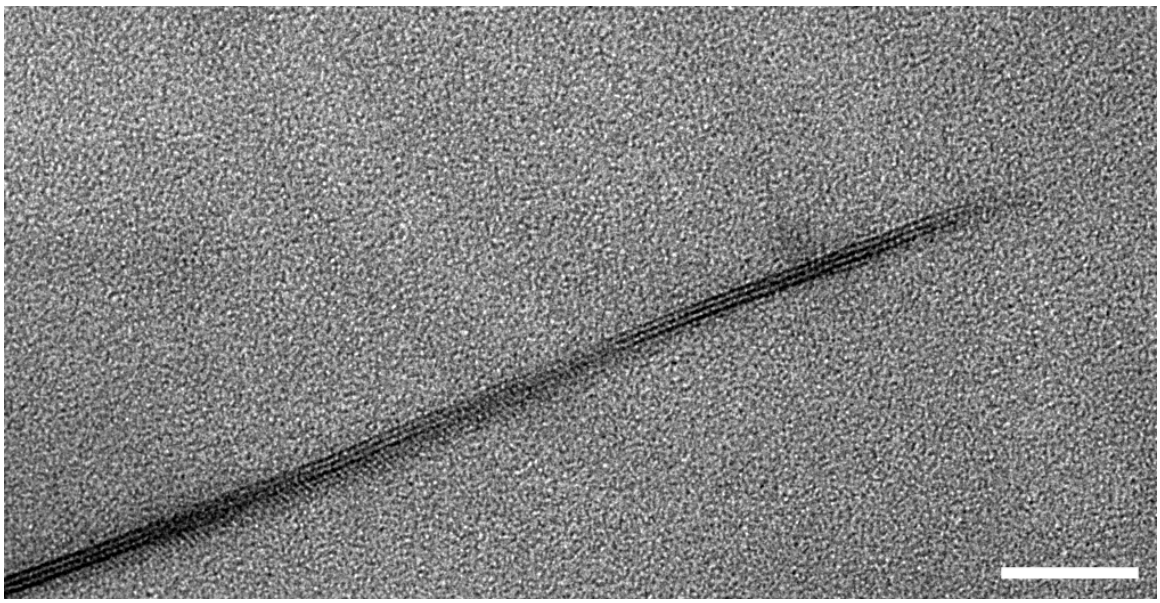

Fig 3.6. HRTEM image of a thinly sectioned MFI nanosheet-polystyrene nanocomposite prepared by melt compounding. The three dark lines running along the nanosheet correspond to the three pentasil chains. The scale bar indicates 20 nm.

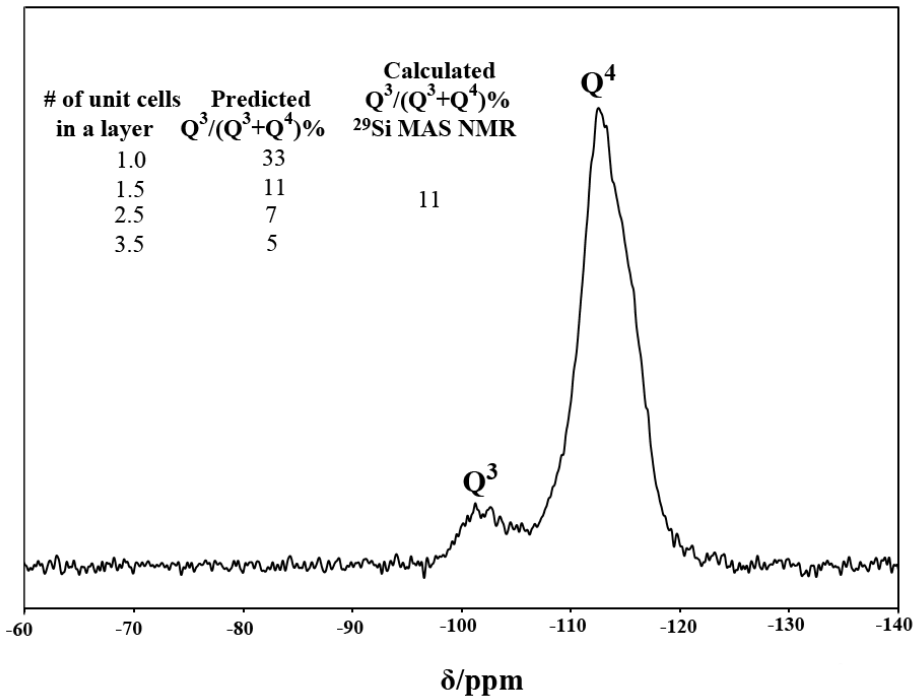

Fig 3.7. ^{29}Si MAS NMR of exfoliated MFI. The $Q^3/(Q^3+Q^4)$ ratios for MFI layer structure with its thickness in the range of 1-2.5 unit cell is listed in the inset. The calculated Q3/(Q3+Q4) ratio from 29Si MAS NMR indicates that the exfoliated MFI layers are 1.5 unit cell thick.

It is worth noting that the XRD of MFI-nanosheets (Fig. 3.5 B) shows sharper reflections compared to that of MWW-nanosheets (Fig. 3.5 A), probably due to the differences in thicknesses and better structural preservation of MFI-nanosheets. The latter could be attributed to the absence of the swelling step in their processing.

Previous attempts to obtain exfoliated nanosheets of MWW have been met with only partial success, due to the fragmentation, aggregation and curling of the lamellae[45, 69, 76], while exfoliation of lamellar silicalite-1 has not been reported before. Our attempts to remove the polystyrene by methods that include calcination or other thermal treatments of the nanosheet-polymer nanocomposite resulted in particles that exhibited significant curling (Fig. 3.8 A and B). The presence of curled particles is detrimental to the quality of coatings because the curled particles neither pack nor orient themselves in their coatings (Fig. 3.8 C and D). However, the dissolution and purification process reported here was sufficient to obtain flat, crystalline exfoliated nanosheets capable of producing a highly packed and oriented coating.

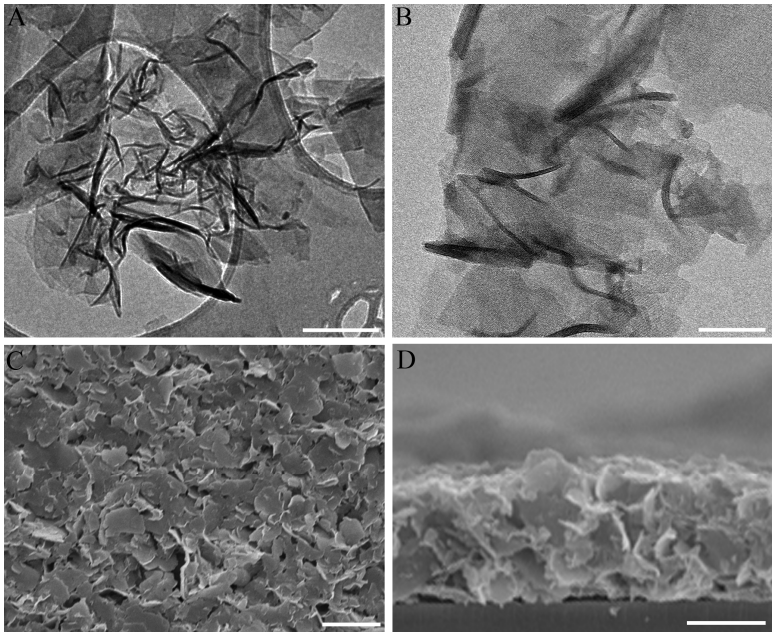

Fig 3.8. TEM images of agglomerated and curled MWW-nanosheets (A) and MFI-nanosheets (B) obtained after calcination of the polymer nanocomposite at 540 °C. SEM images (top- (C) and side-views (D)) of MWW-nanosheet coating formed from an aqueous dispersion of nanosheets obtained after calcination of the polymer nanocomposite at 540 °C. The nanosheet orientation in the coated film is not uniform due to their curling and bending. The scale bars indicate 200 nm for (A), 50 nm for (B) and 1 micron for (C) and (D).

The presence of microporosity (Fig. 3.9) within the MFI layers imparts molecular sieving and hosting capabilities and thus, expands the list of available nanosheets amenable to layer-by-layer assembly[77, 78] for the fabrication of nanocomposites. Moreover, due to their large lateral area and small thickness, the zeolite nanosheets can coat porous substrates to form well-packed thin deposits. As a result, these nanosheets are attractive materials for the fabrication of thin zeolite membranes. For example, simple filtration of the MFI-nanosheet suspension through an anodized alumina membrane (Anopore, pore size 200 nm) followed by calcination for polymer removal resulted in a uniform, well-packed deposit consisting of highly oriented, overlapping flat nanosheets (Fig. 3.10A). Even rough porous substrates, such as homemade α-alumina supports with ca. 200 nm pores, can be coated by filtration to obtain smooth films (Fig. 3.10 B, C, D and E). Fig. 3.10 B is a top view SEM image of an MFI-nanosheet coating on α-alumina indicating uniform surface coverage. Because the nanosheets are very thin, secondary electrons from the underlying nanosheets can be observed marking their morphology and underscoring the overlap. Cross-sections cut by focused ion beam (FIB) were observed by ion beam microscopy (Fig. 3.10 C) and TEM (Fig. 3.10 D and E). We observed no penetration of the nanosheets in the interior of the substrate. This is a desirable feature for forming thin zeolite films to achieve high flux membranes. The nanosheets conform to the substrate surface roughness due to their high aspect ratio and nanometer-range thickness. As a result, neither masking of the support pores[60] nor use of smoothened multilayered (asymmetric) membranes[31] or functionalization[13] is necessary as in the case of coating from isotropic zeolite nanoparticles or non-isotropic microparticles. However, these films do not show any selectivity for *p-/o*-xylene (a typical mixture that is widely used to assess the molecular sieving capability of MFI films[14, 29]). It is evident from Figure 3.10D and the HRTEM image in Figure 3.10E that nm-sized gaps exist in between the nanosheets. After a single hydrothermal treatment for 4.5 hours at 90 ^{o}C under conditions, that in the absence of nanosheet coating do not result in an observable deposit (molar composition, 60 SiO_2: 9 TPAOH : 8100 H_2O : 240 EtOH; aged at 90 ^{o}C for 6 hours), the MFI-nanosheet film thickness remained unchanged (Fig. 3.11 A, B, C and D), while the gaps between the

nanosheets were reduced, as suggested by the TEM images of the film cross-section (Fig. 3.11 D and E) and an improved separation performance. Five membranes prepared by this method separated xylene isomers (*p*-xylene from *o*-xylene) with *p*-xylene/*o*-xylene separation factor of 40-70 and *p*-xylene permeance of 3×10^{-7} mol/m^2-s-Pa^{-1} at 150 ^{o}C (Fig. 3.12).

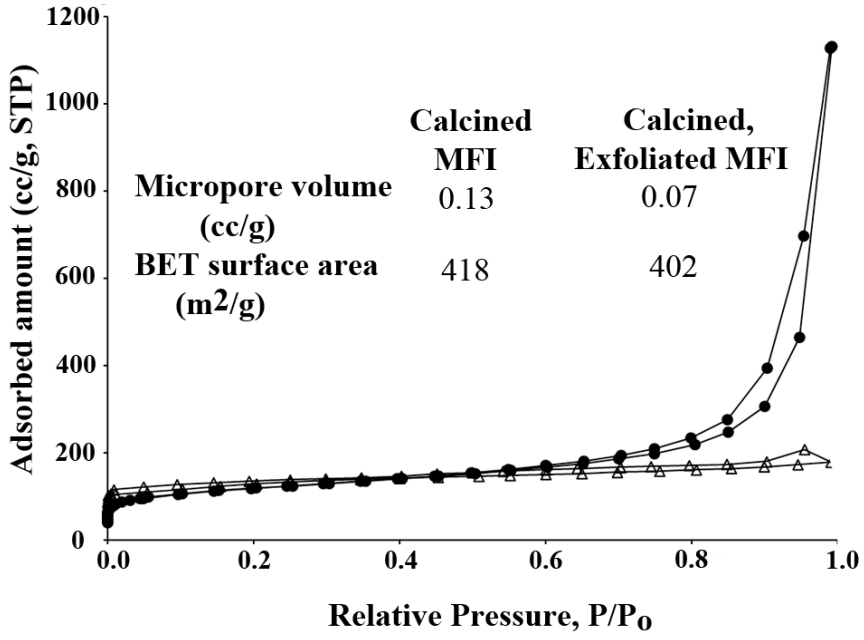

Fig 3.9. N_2 adsorption-desorption isotherm of calcined commercial MFI (triangles) and calcined, exfoliated MFI (circles). Textural data (micropore volume and BET surface area) are given in the insets.

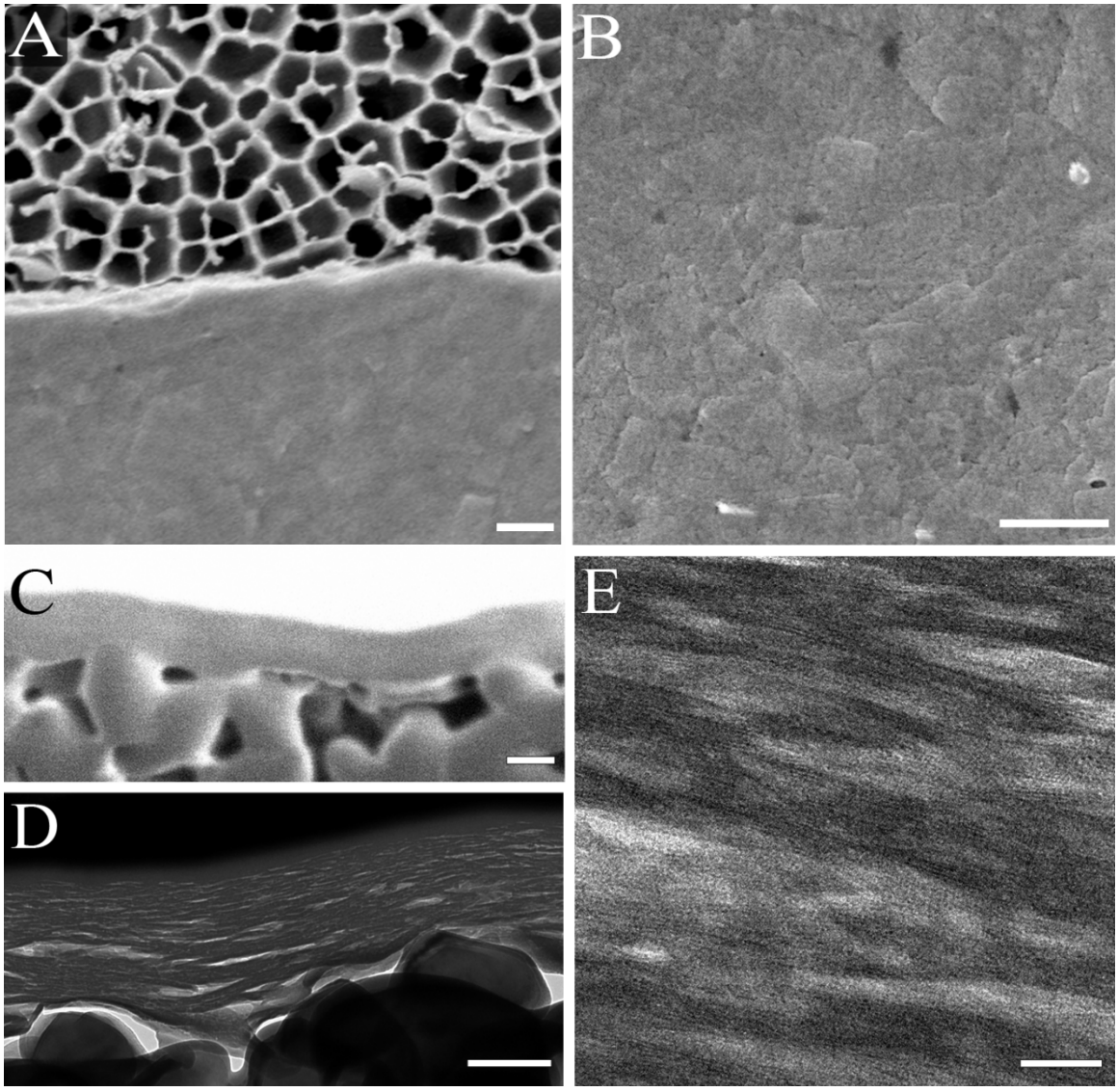

Fig 3.10. Images of the MFI-nanosheet coating on porous supports. A: SEM image (top-view) of the coating of MFI-nanosheets on an Anopore disk. The top half of the image shows the bare Anopore support, while the bottom half shows a uniform coating of nanosheet on the 200 nm pores of the support. B: SEM image (top-view) of the coating of MFI-nanosheet on a homemade porous α-alumina support. C: FIB image of the cross section of the coating in (B). The image is taken by a Ga ion source (30 KV) at a tilt angle of 52^0. The nanosheet coating is sandwiched between the FIB deposited platinum (to protect the coating from milling) and the alumina support. D: TEM image of the cross section of the coating in (B). The dark layer on top of the coating is FIB deposited platinum. E: HRTEM image of the coating cross section. The scale bars indicate 200 nm in (A) to (D) and 20 nm in (E).

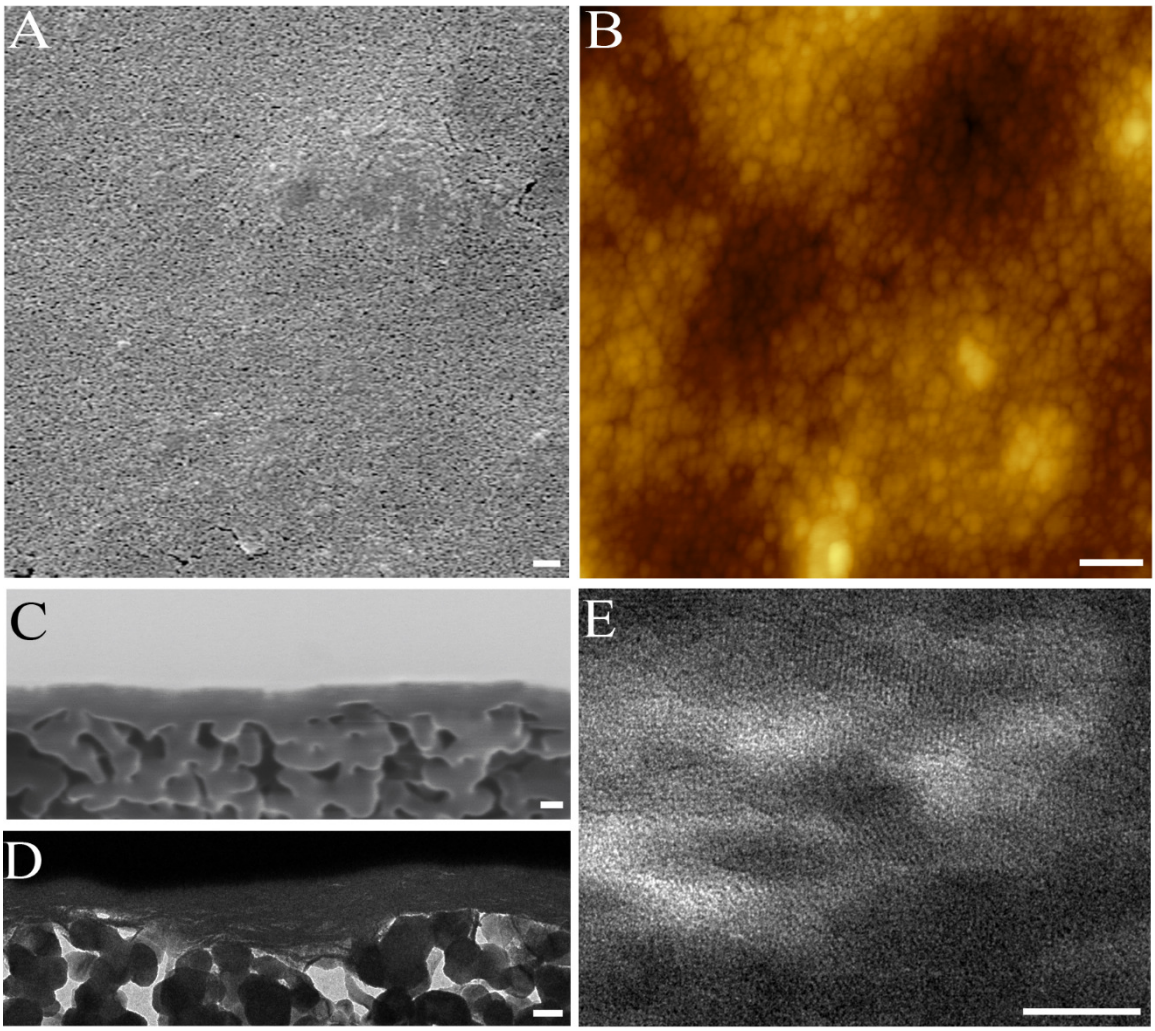

Fig 3.11. Images of the MFI film on a homemade porous α-alumina support after the secondary growth of MFI-nanosheet coating. Secondary growth was done at 90 ^{0}C for 4.5 hours in a synthesis sol with a composition of 60 SiO_2 : 9 TPAOH : 8100 H_2O : 240 EtOH (aged at 90 ^{0}C for 6 hours before being used for secondary growth). A: SEM image (top-view) of the film. B: AFM topographical image of the film revealing surface roughness due to ca. 25 nm steps formed on the smooth surfaces of the nanosheets. C: FIB image of the cross section of the film. The image is taken by a Ga ion source (30 KV) at a tilt angle of 52^0. The film is sandwiched between FIB deposited platinum (to protect the coating from milling) and the alumina support. D: TEM image of the cross section of film. The dark layer on top of the coating is FIB deposited platinum. E: HRTEM image of the coating cross section. The scale bars indicate 200 nm in (A) to (D) and 20 nm in (E).

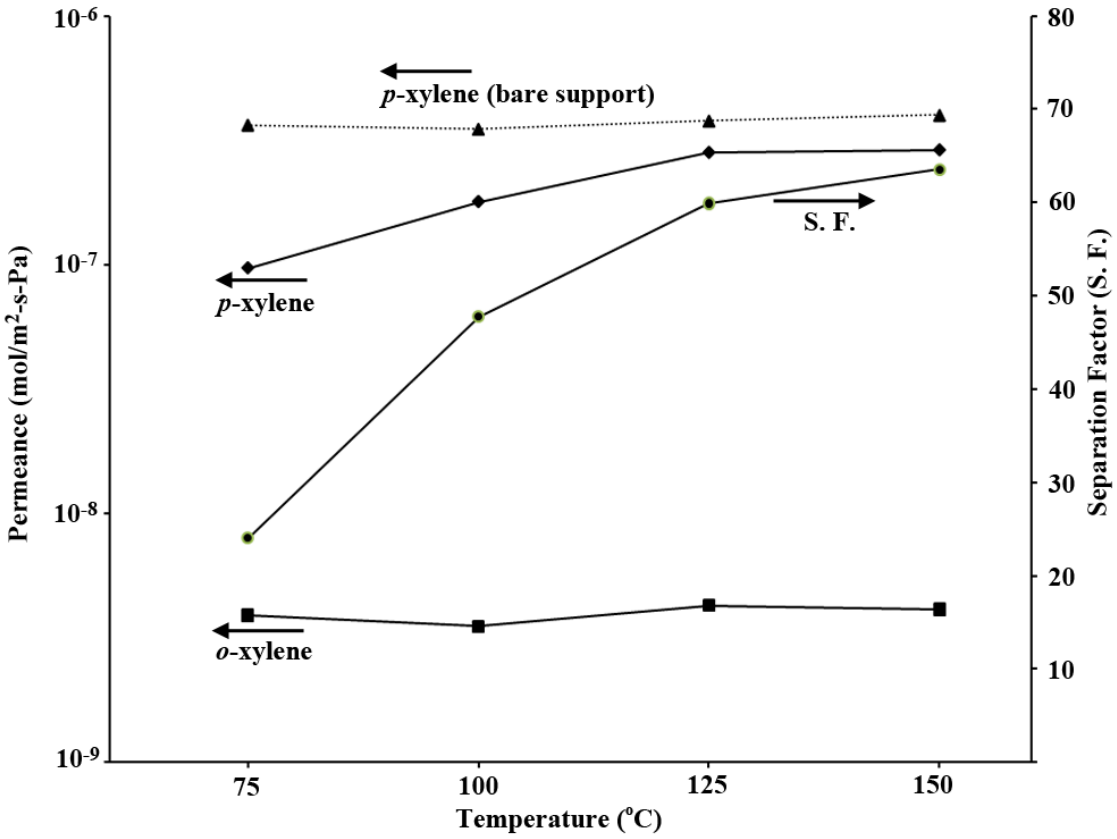

Fig 3.12. *P*-xylene and *o*-xylene permeances and *p*-/*o*- xylene separation factors versus temperature for one of the five membranes tested. *P*-xylene permeance through a bare support is given for comparison.

3.5 Summary

These findings indicate that the films fabricated using exfoliated zeolite nanosheets exhibit the expected molecular sieving properties and are appropriate to be used as a membrane. The exfoliation and purification process, described here, may also be applicable to other microporous layered materials to obtain high-aspect-ratio, crystalline nanosheets with high purity and thickness uniformity. Moreover, the simple film formation method introduced, based only on filtration of the nanosheet suspensions, is likely to be easily scalable for large scale membrane formation on low-cost, commercially available porous supports with large pores and rough surfaces.

Chapter 4: Purification of Exfoliated MFI-nanosheets by Density Gradient Centrifugation

4.1 Introduction

The development of better separation processes was and remains today a major activity for chemical engineers.[79] Among advancements in nanotechnology, thin film fabrication of microporous materials emerged in the last two decades as a possible route to high throughput membranes. Sub-500nm-thick zeolite films are desirable for large-scale deployment of this technology.[80] These ultrathin zeolite membranes can be fabricated by oriented assembly of high-aspect-ratio zeolite nanosheets on porous supports.[81-83] In contrast to isotropic zeolite nanocrystals, zeolite nanosheets are flexible, allowing them to conform to the rough surface of the underlying support, without the need of support pore masking[60], or support modification using mesoporous top-layers[31]. Recently, starting from multilamellar MFI[8], 1.5 unit cell-thick MFI-nanosheets were obtained via exfoliation of the lamella by melt compounding with polystyrene.[82] Dissolution of the polymer-zeolite nanocomposite in toluene, followed by removal of unexfoliated particles by a one-step centrifugation process, yielded structurally and morphologically intact zeolite nanosheets. A simple filtration technique followed by a mild hydrothermal treatment was used to fabricate ca. 350 nm thick zeolite membranes, which separated *p*-xylene from *o*-xylene.

To fabricate thinner zeolite membranes using these MFI-nanosheets, the coating suspension must be further purified to obtain uniform (in thickness and lateral size) nanosheets, while removing the larger unexfoliated particles and the polystyrene used in the melt compounding process. Polystyrene removal by heat treatment leads to curling and agglomeration of nanosheets, deteriorating their ability to pack and orient in a thin film. [82] Therefore, a method is required to purify nanosheets without inducing structural and

morphological damages. Solution processing of nanosheets by density gradient centrifugation (DGC) is one such technique.

In DGC, particles are separated by exploiting the differences in their sedimentation velocity. This is attained by centrifugation of the particles in a fluid medium with density gradient along the depth of the fluid[84]. The density gradient can be linear (linear increase in density along the depth of the fluid) or nonlinear (by stacking of fluids with dissimilar densities). If centrifugation is carried out for a long enough time to achieve equilibrium, particles with identical density accumulate in corresponding density zones along the depth of the fluid (isopycnic sedimentation). In the case of particles with different size and shape but identical density, a non-equilibrium approach is adopted (rate-zonal centrifugation[85]). In this case, segregation of particles is time-dependent as, for example, larger particles sediment at a faster rate as compared to the smaller particles.

DGC was first reported as a tool to calculate the molecular weight and partial specific volume of DNA and viruses by isopycnic sedimentation[86]. Leif and Vinograd applied this technique to purify subpopulations of human erythrocytes in a linear density gradient of bovine serum albumin[87]. Since then, density gradient has been used to separate a variety of cells[88-90] and cell fractionates[91-94]. This concept was also applied in measurement of the density of polymeric nanoparticles[95] as well as their purification[96-98] by isopycnic sedimentation. For example, three different styrene-butyl methacrylate latex particles were fractioned in linear density gradient created by sucrose solution in water, enabling a study of monomer distribution in each type of latex particle[97].

Recently, density gradient centrifugation has been used to purify carbon nanotubes (CNTs) based on their diameter[99-103], wall thickness[104, 105], length[106] and aggregation[107, 108], leading to fabrication of next generation thin-film electrical devices. Arnold et al. pioneered isopycnic segregation of nanotubes by surfactant encapsulation of single wall carbon nanotubes (SWCNTs), leading to change in the density of nanotubes as a function of diameter[99]. A repeated isopycnic ultracentrifugation in a linear density gradient of iodixanol successfully fractionated SWNTs of different diameters. Using a similar principle, double wall CNTs were separated from single and multiwall CNTs,

carbonaceous impurities and metallic catalyst particles, for applications in field-effect transistors and transparent conductors[104]. Ghosh et al. applied a nonlinear density gradient to separate highly polydisperse sample of SWCNTs in a single step[101]. Fractionation of CNTs based on their length was reported by non-equilibrium rate-zonal centrifugation by exploiting the transient motion of SWNTS in a dense fluid medium[106].

DGC has been also applied to purify a variety of spherical nanoparticles. FeCo nanocrystals coated with graphitic shells were separated by nonlinear density gradient[109]. Gold core/silica shell nanoparticles for application in plasmonics nanoantennas were purified using high viscosity iodixanol density gradient[110]. Monodisperse Si nanocrystals were obtained by fractionation in density gradient of 40% 2-4-6 tribromotoluene in cholorobenzene[111].

Reports of fractionation of particles with sheet-like morphology have been limited. Exfoliated graphene sheets were purified using similar principles applied in fractionation of CNTs in iodixanol density gradient[112]. Sun et al. used rate zonal centrifugation in sucrose density gradient to separate chemically modified graphene in few minutes using ultracentrifugation[113]. Reports of purification of clay particles have been limited to soil mineralogy. DGC in a mixture of tetrabromoethane and acetone was used to identify and separate clay particles saturated by H^+, Ca^{+2}, K^+ and Cs^{+2} ions[114]. Similar density gradient technique was used to fractionate <0.2µm clay materials from three soils with different Fe-oxide minerology[115].

Barring a few[111, 115-117], most of the DGC experiments[84-110, 112-114] have used aqueous density gradient (iodixanol, sucrose, etc.) for fractionation of particles. However, MFI-nanosheets are difficult to stabilize in aqueous suspensions due to presence of long hydrophobic surfactant embedded in their structure[8, 37, 40]. Most of the isopycnic fractionations reported in the literature were carried out for a long time (up to a day) using ultracentrifuges, which also puts restriction on the processable volume. Here, we report purification of MFI-nanosheets from polystyrene, organic contaminations, and unexfoliated particles by using rate-zonal centrifugation in nonlinear density gradients created with organic solvents in a regular centrifuge. Fabrication of an ultrathin zeolite

membrane on a porous alumina support is demonstrated using the MFI-nanosheets purified by DGC.

4.2 Experimental Material and Methods

4.2.1 Purification of Nanosheets to Remove Polystyrene

Nanocomposite of MFI-nanosheets and polystyrene were prepared as reported before.[82] Briefly, multilamellar MFI, prepared by the procedure reported by Ryoo and co-workers[8], was exfoliated by melt compounding with polystyrene[44]. 3.0 g of exfoliated nanocomposite was dispersed in toluene to yield 1.0% w/w suspension by sonication in a bath sonicator (Branson 5510R-DTH, 135 watts) for 30 minutes. The resulting suspension was centrifuged (Beckman Coulter, Avanti J-20 XP equipped with JA25.50 rotor) in four 50 ml FEP centrifuge tubes at 40,000g for 3 hours to sediment zeolite nanosheets at the bottom of the centrifuge tubes. Sedimented nanosheets were separated from the supernatant and re-dispersed in toluene. The centrifugation and re-dispersion process was repeated twice. The resulting nanosheet sediment was then dispersed in 20 ml toluene, and placed on top of 20 ml chlorobenzene in a 50 ml FEP centrifuge tube, drop by drop by a transfer pipette, to create a nonlinear one step density gradient. Centrifugation was carried out at 40,000g for 3 hours. At the end of centrifugation, the nanosheets sedimented at the bottom of the centrifuge tube were collected by pouring out the supernatant. A part of the nanosheet sediment was analyzed by thermogravimetric analysis (TGA) to confirm the removal of polystyrene.

4.2.2 Purification of Nanosheets to Remove Unexfoliated Zeolites

The zeolite sediment obtained after removal of polystyrene was dispersed in 20 ml n-octanol by horn sonication (Qsonica Q500, 500 watts, 0.125” micro-tip operating at 20% of maximum amplitude) for 3 minute followed by sonication in the bath sonicator for 30 minutes. A nonlinear multilayered density gradient was created in a 50 ml FEP centrifuge tube by sequentially placing 5 ml chloroform (ρ = 1.48 g/cc), 5 ml dichloromethane (ρ = 1.33 g/cc), 10 ml chlorobenzene (ρ = 1.10 g/cc), and finally 20 ml nanosheet suspension in

octanol. After centrifugation at 12,000g for 30 minutes, the liquid fractions defined by the solvent interfaces were collected by transfer pipettes in separate vials. These fractions were characterized by transmission electron microscopy (TEM). The top fraction (n-octanol) was diluted to 40 ml and centrifuged at 40,000g for 3 hours to sediment the purified nanosheets. The sedimented nanosheets were dispersed in 40 ml n-octanol by the horn sonication for 3 minute followed by sonication in the bath sonicator for 60 minutes. This suspension was characterized by TEM and high resolution TEM (HRTEM), and used for fabrication of nanosheet films.

4.2.3 Fabrication of Support, Thin nanosheet Film and Membrane

Fabrication of the round α-alumina disks (22 mm in diameter and 3 mm in thickness) by hydraulic pressing of dry α-Al_2O_3 powder (CR-6, Baikowski, average particle size of 400 nm) was carried out as reported before[74]. Supports were sintered at 1160°C for 6 hours for mechanical strength.

For fabrication of supports by colloidal processing, α-Al_2O_3 powder was added to water to make a 20 vol. % suspension. The suspension was electrostatically stabilized at pH 2.2 by slow addition of HNO_3. Horn sonication for 3 minutes followed by bath sonication for 90 minutes was carried out to disperse the agglomerated particles. This suspension was filtered through a 1 micron stainless steel mesh (TWP Inc., part# MIC1TL5) to remove any remaining large agglomerates. The bubbles in the suspension were suppressed by addition of 3 µl n-octanol/g to the suspension, followed by degassing of the suspension in the bath sonicator. For gypsum mold casting, the alumina suspension was poured inside an annular PTFE cylinder (I.D. = 22 mm) standing vertically on a 25 µm cellulose fiber filter (Whatman) on the gypsum mold. Fabrication of support by filtration was achieved by pouring the alumina suspension inside the annular PTFE cylinder standing vertically on a 0.2 micron nylon membrane (Whatman) under partial vacuum (-14 kPa), as shown in Fig. 4.1A. After 2 hours, alumina compacts were removed from the PTFE annulus and dried overnight at the room temperature. The surface of each

compact was cleaned from the loose alumina particles by blowing it with pressurized nitrogen (80 psig). The compacts were then sintered under air flow (150 ml/minute) at 1050 ˚C or 1150°C for 3 hours with heating rate of 2 ˚C/min. To improve the interaction between the support and the zeolite film, the supports were treated with air plasma (Harrick plasma cleaner, PDC-32G) for 2 minute prior to the fabrication of nanosheet film.

Thin nanosheet film was fabricated on alumina supports by vacuum assisted filtration. 0.3 g of nanosheet suspension was diluted with 3.0 g n-octanol and sonicated in the bath sonicator. The sonicated nanosheet suspension was poured over the alumina support held under vacuum in a homemade setup (Fig. 4.1B). At the end of filtration, the disk was dried at 150 ˚C for 4 hours, and calcined under air flow (150 ml/min) at 550 ˚C for 6 hours with heating rate of 1 ˚C/min, to remove the organic structure-directing agent (OSDA) from the nanosheet framework. The calcination was carried out in a quartz petri dish (Technical Glass Products) covered with a cap with a gas inlet and outlet. The retention time of air in the petri dish was ca. 2 minutes.

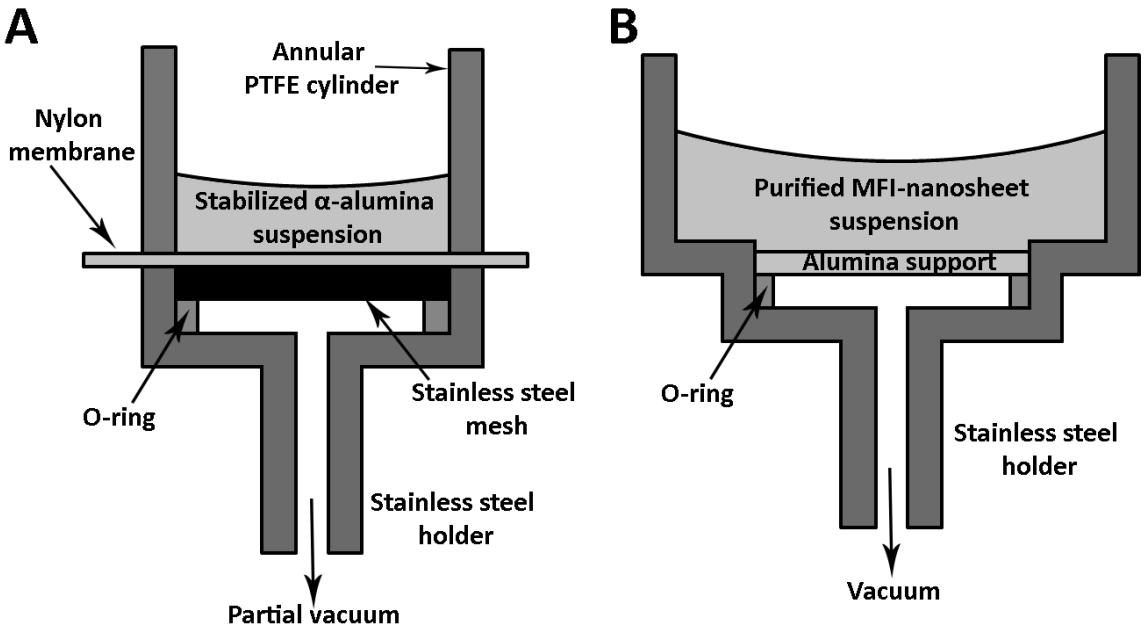

Fig 4.1. Schematic diagrams showing the experimental setups. A: Fabrication of α-alumina support by colloidal processing. B: Fabrication of a thin MFI-nanosheet film on the α-alumina support.

The growth suspension used to reduce the interparticle gaps in the nanosheet film was prepared as reported before.[82] Briefly, a synthesis sol (60 SiO_2: 9 TPAOH: 8100 H_2O: 240 EtOH) was hydrolyzed overnight, and aged at 100 □C for 6 hours in a Teflon-lined stainless steel autoclave. The alumina disk coated with MFI-nanosheet was placed vertically in the aged synthesis sol, and heated at 100 □C for 16 hours in a Teflon-lined stainless steel autoclave. The resulting membrane was then calcined under air flow (150 ml/min) in the quartz petri dish at 480 ˚C for 4 hours with heating rate of 0.5 ˚C/min, to remove TPAOH from the membrane framework.

4.3 Characterization

TGA analysis (Perkin-Elmer TGA-7 analyzer) was done to estimate the amount of organic content in the zeolite sediment obtained after purification by DGC in toluene-chlorobenzene gradient. Analysis was carried out by heating a few mg of the zeolite sediment in air flow (100 ml/min) from 130 ˚C to 550 ˚C (heating rate of 1 ˚C/minute) and maintaining the sample at 550 ˚C for 8 hours.

TEM specimens were prepared by depositing a drop of the suspensions on a TEM grid (ultrathin carbon film on holey carbon support film, 400 mesh Cu, Ted Pella) followed by drying the coated grid in ambient conditions. All TEM and high resolution TEM (HRTEM) studies were conducted using an FEI Tecnai T12 TEM operating at 120 kV and an FEI Tecnai G2 F30 TEM operating at 300 kV, respectively. The images were acquired using a CCD camera.

For preparation of atomic force microscopy (AFM) specimen, 20 µl of purified nanosheet suspension was deposited on a hydrophobic silicon wafer by spin coating at 3000 rpm for 4 minutes. The nanosheet coating was calcined in air flow at 540□C for 6 hours to remove the OSDA from the pores and surface of the nanosheets. AFM was carried out in tapping mode in the repulsive regime using a Molecular Imaging PicoPlus scanning probe microscope (since renamed Agilent 5500 AFM/SPM system). The AFM image analysis was performed using Gwiddion 2.30 software. For calibration of the AFM height

data, 2.0 nm steps of the muscovite mica, created by etching a freshly cleaved muscovite mica in 50% hydrofluoric acid for 4 hours[75], was used as the calibration standard.

For preparation of cross-sections, the nanosheet film and the membrane were coated with approximately 300 nm Au by a sputter coater to protect the surface from beam damages from focused ion beam (FIB). Cross-section was prepared by a FIB equipped with a Ga ion source operating at 30 kV (Quanta 3D DualBeam).

Scanning electron microscopy (SEM) images of the nanosheet film, membrane and cross-sections prepared by FIB were acquired using JEOL 6700 microscope operating at 1.5 kV. Cross section specimens were tilted to 40-48 degree for SEM imaging.

Xylene isomer vapor permeation measurements were carried out as reported before.[82]

4.4 Results and Discussion

4.4.1 Zeolite Nanosheet Purification by DGC

Melt compounded zeolite-polystyrene nanocomposites consist of 96% w/w polystyrene and 4% w/w MFI-nanosheets. Upon dissolution of the zeolite-polystyrene nanocomposite in toluene by sonication, MFI-nanosheets dispersed in the toluene. During centrifugation of this suspension at 40,000g for 3 hours, MFI-nanosheets sediment at the bottom of the centrifuge tube due to the difference of density between nanosheets ($\rho \sim 2.00 - 2.20$ g/cc) and toluene (0.87 g/cc). Since, polystyrene remains dissolved in the supernatant phase (toluene), the sediment consists of mostly MFI-nanosheets. However, the MFI-nanosheets sediment obtained after discarding the supernatant is wet with toluene, and consequently polystyrene dissolved in the toluene. The amount of polystyrene can be further reduced by re-dispersion of the sediment in fresh toluene followed by repetition of the centrifugation process. However, despite this repeated centrifugation and re-dispersion washing process, it is not possible to completely eliminate polystyrene from the zeolite sediment. Fig. 4.2A shows the image of the nanosheet sediment purified by 5 cycles of centrifugation and re-dispersion, dispersed in n-octanol. Polystyrene, which is insoluble in n-octanol, can be seen as spherical particles in the TEM image.

Instead of purification by repeated centrifugation and washing, MFI-nanosheets can be purified from polystyrene using DGC. Centrifugation of the zeolite sediment dispersed in toluene across a step density gradient of toluene/chlorobenzene enables efficient removal of polystyrene (Fig. 4.2B). The density of polystyrene (ρ = 1.06 g/cc) is lower than that of chlorobenzene (ρ = 1.10 g/cc). Also, since chlorobenzene is a poor solvent of polystyrene, polystyrene does not diffuse in the chlorobenzene fraction during centrifugation. On the other hand, denser zeolite nanosheets (ρ ~ 2.00 - 2.20 g/cc) sediment in the chlorobenzene fraction and deposit at the bottom of the centrifuge tube (schematic in Fig. 4.2C). TGA curves of the nanosheet sediments from two separate experiments indicate complete removal of polystyrene (Fig. 4.2C). The weight loss of zeolite sediment during heat treatment to 550 ˚C can be accounted for by the expected loss due to the removal of the organic structure directing agent (OSDA) associated with the MFI-nanosheets[8, 40]. Theoretically, OSDA embedded in the straight pore channels (along the *b*-axis of nanosheets), comprises 20% of the weight of the 1.5 unit cell thick MFI-nanosheets. Extra-framework OSDA, which are loosely held on the surface of nanosheets, comprises another 21% of the weight of MFI-nanosheets, as estimated by the TGA curve in Fig. 4.3. Some of these loosely adhered extra-framework OSDA are expected to be washed away during the DGC processing. Based on this, DGC purified nanosheets are expected to lose 20-41% of their weight in the TGA experiment. The weight loss of DGC processed nanosheets from two separate experiments reported here are well within this range (Fig. 4.2C), indicating complete removal of polystyrene.

MFI-nanosheets purified from polystyrene using nonlinear DGC, did not disperse well in toluene, and agglomerated and sedimented within minutes. Perhaps, the presence of large amount of polystyrene in the unpurified suspension, aided the dispersion of nanosheets in toluene. Moreover, due to presence of long hydrophobic tail of OSDA on the surface of MFI-nanosheets, it is not possible to prepare a stable dispersion of nanosheets in aqueous medium. Therefore, a number of organic solvents were explored to obtain a complete dispersion of MFI-nanosheets. Among them (cyclohexane, n-hexane, chloroform, dichloromethane, chlorobenzene, tetrahydrofuran, ethanol, n-butanol, and n-

octanol), n-octanol dispersed the nanosheets most effectively, and the resulting suspension was stable for many days.

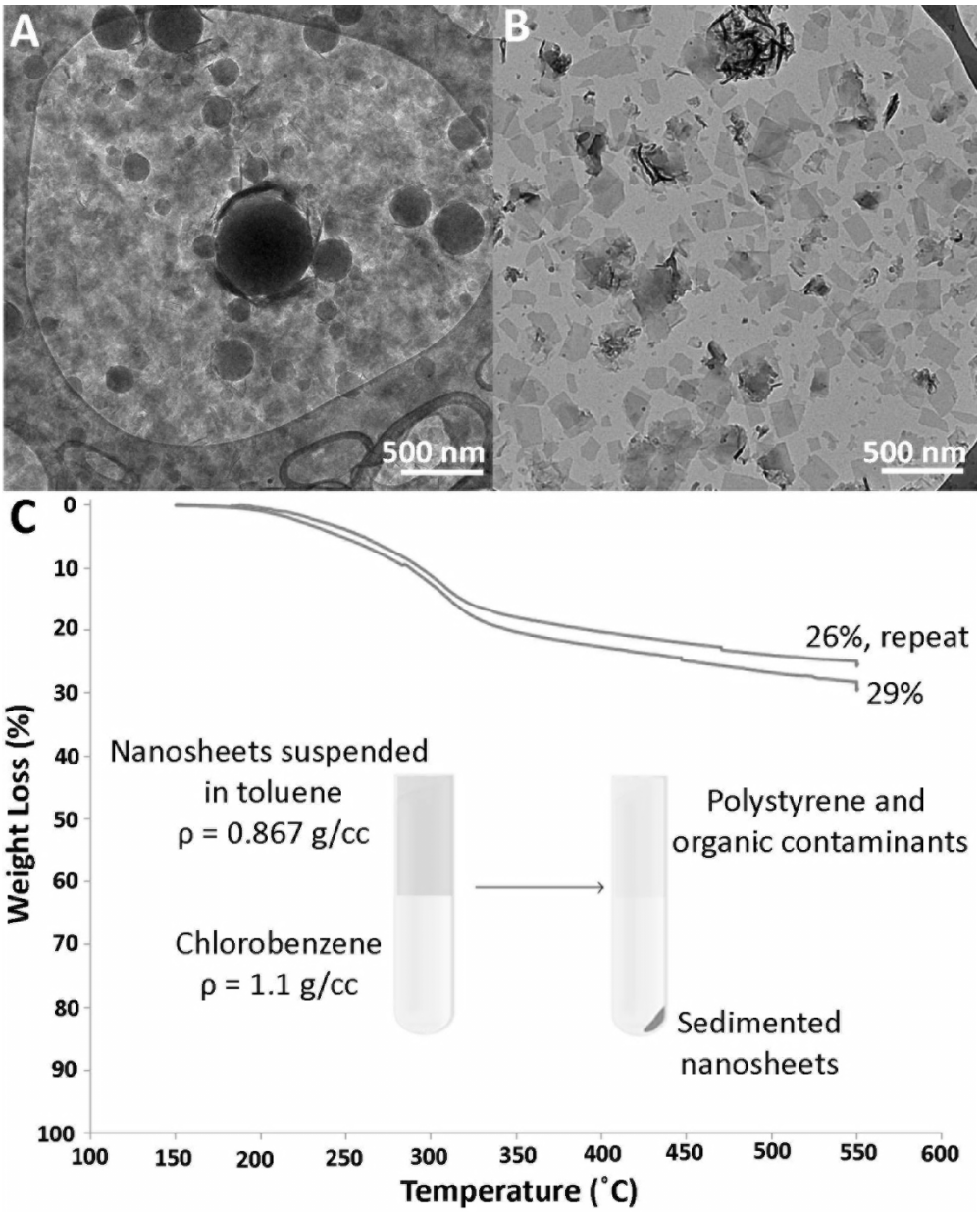

Fig 4.2. A: TEM image of MFI-nanosheets sediment before purification by density gradient centrifugation (DGC). The sediment was prepared by 5 cycles of washing in centrifugation and re-dispersion in toluene. The spheres in the image are polystyrene, which precipitated upon dispersion of the sediment in n-octanol. B: TEM image of MFI-nanosheets purified from polystyrene by nonlinear DGC. C: TGA curves from two separate DGC purification experiments showing expected weight loss of nanosheet sediments due to elimination of organic structure directing agent (OSDA). The schematic below the TGA curves illustrates the experiments for separation of polystyrene from MFI-nanosheets in the toluene-chlorobenzene density gradient.

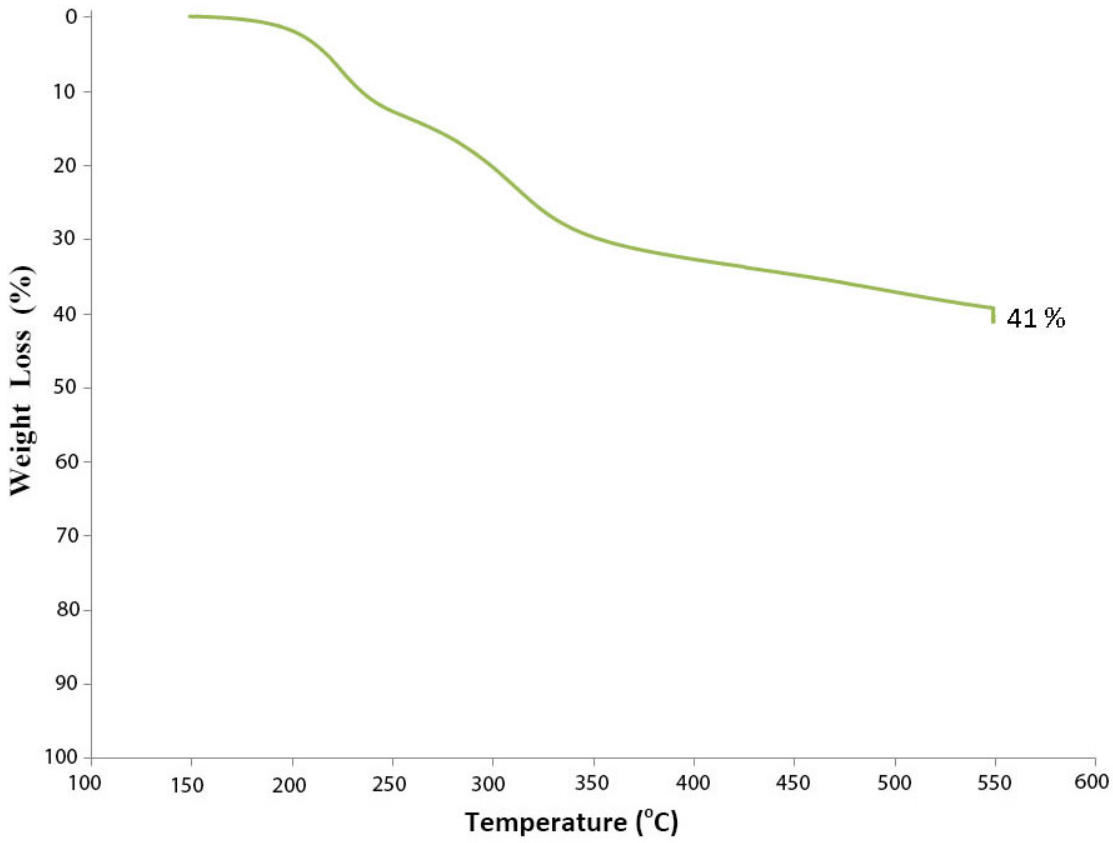

Fig 4.3. TGA curve showing weight loss of as-made multilamellar MFI due to loss of OSDA.

Modification of the density of MFI-nanosheets by surfactant encapsulation and subsequent isopycnic centrifugation[99] is difficult due to the presence of the long tail OSDA on the surface of the nanosheets[99]. Instead, exfoliated nanosheets can be separated from larger unexfoliated nanosheets based on the differences in sedimentation rate, using rate-zonal centrifugation. A nonlinear density gradient created by a simple stacking of fluids with varying density has been proved effective in separating particles based on their size and shape[109]. Based on this, purification was carried out by placing nanosheet suspension in n-octanol ($\rho = 0.82$ g/cc) over density stacks created by cholorobenezene ($\rho = 1.10$ g/cc), dicholoromethane ($\rho = 1.33$ g/cc), and choloroform ($\rho = 1.48$ g/cc), followed by a mild centrifugation at 12,000g for 30 minutes. Four fractions, marked by the solvent interfaces,

were collected and analyzed by TEM, as shown in Fig. 4.4. A quantitative survey on the presence of unexfoliated nanoparticles in each fraction was done by counting the number of unexfoliated particles per 5000 exfoliated nanosheets. There were no unexfoliated particles per 5000 exfoliated nanosheets in the top fraction (F1). Two unexfoliated particles per 5000 nanosheets were found in the 2nd fraction from top (F2). There were a large number of unexfoliated particles in the 3rd (F3) fraction, while the 4th fraction (F4) primarily comprised of unexfoliated particles.

Fig. 4.4A shows TEM image of F1. The presence of segregated, *b*-oriented MFI-nanosheets with uniform contrast is indicative of uniform thickness of nanosheets. Parts of the nanosheets are chipped, perhaps due to vigorous sonication of the zeolite sediments for re-dispersion during the purification process. The MFI-nanosheets obtained by this purification process are polydisperse in their lateral dimension (aspect-ratio). Further optimization of DGC is needed to limit the polydispersity in aspect-ratio of MFI-nanosheet for improvement in packing efficiency of the nanosheets. TEM images of MFI-nanosheets in F2, F3 and F4 are shown in Fig. 4.4B, C, and D respectively. MFI-nanosheets in these fractions are agglomerated, which can be attributed to the instability of nanosheets in chlorobenzene, dichloromethane and choloroform. The yield of exfoliated MFI-nanosheets in F1 is 10%, which is a 2-fold improvement vs. the yield of exfoliated MFI-nanosheets reported before.[82] Future work will focus on further improvement of the yield of the MFI-nanosheets purified by DGC.

Fig. 4.5A shows a higher magnification TEM image of a MFI-nanosheet from F1. The nanosheet is *b*-oriented (i.e., with their *b*-axis along the direction of the e-beam) as it lays flat on the TEM grid due to its high-aspect-ratio (~100). The electron diffraction (ED) pattern of the nanosheet in Fig. 4.5A is shown in Fig. 4.5B. The presence of diffraction spots corresponding to *d*-spacing as small as 1.96 Å establishes that purified MFI-nanosheets are highly crystalline. The ED pattern of ten randomly chosen MFI-nanosheets was studied. All ten nanosheets exhibited ED pattern of MFI oriented along *b*-axis, indicating absence of an amorphous phase. Fig. 4.5C shows a high resolution TEM (HRTEM) image of a part of a *b*-oriented MFI-nanosheet. The HRTEM image has a low

contrast because MFI-nanosheets are only 3.2 nm thick.[82] The bright spots in the HRTEM images are due to the 10 member ring (MR) MFI straight pore channels running along the *b*-axis. The fast Fourier transform (FFT) of the image (Fig. 4.5D) indicates 2.4 Å resolution, comparable to that attainable by imaging of regular zeolite crystals.

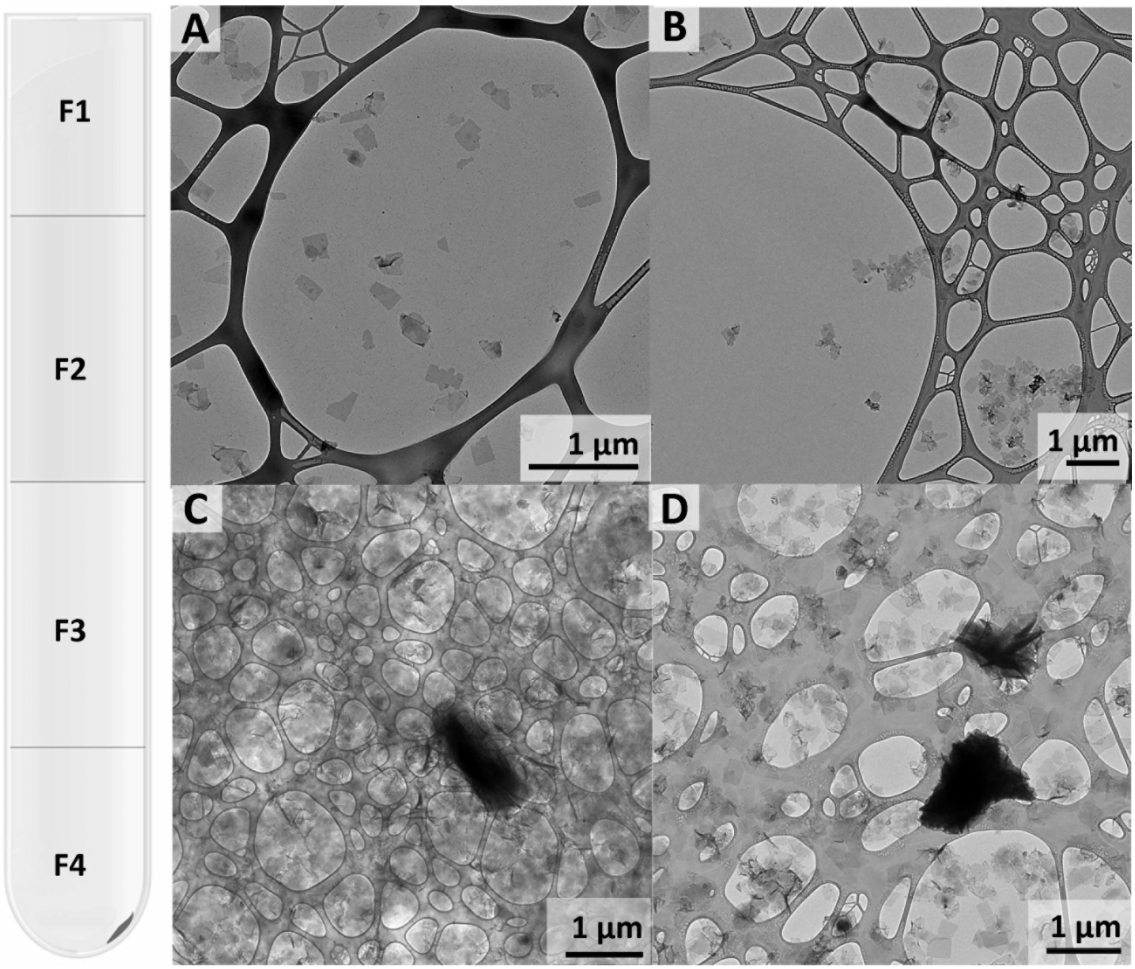

Fig 4.4. Left: Schematic of a centrifuge tube showing the four fractions obtained after the nonlinear density gradient centrifugation (DGC) (F1: n-octanol fraction; F2: chlorobenzene; F3: dichloromethane and F4: chloroform fractions). Right: the corresponding TEM images. A: Top (n-octanol) fraction showing MFI-nanosheets completely purified from unexfoliated particles. B: Agglomerated MFI-nanosheets in the chlorobenzene fraction. Larger unexfoliated particles in dichloromethane (C) and chloroform (D) fractions.

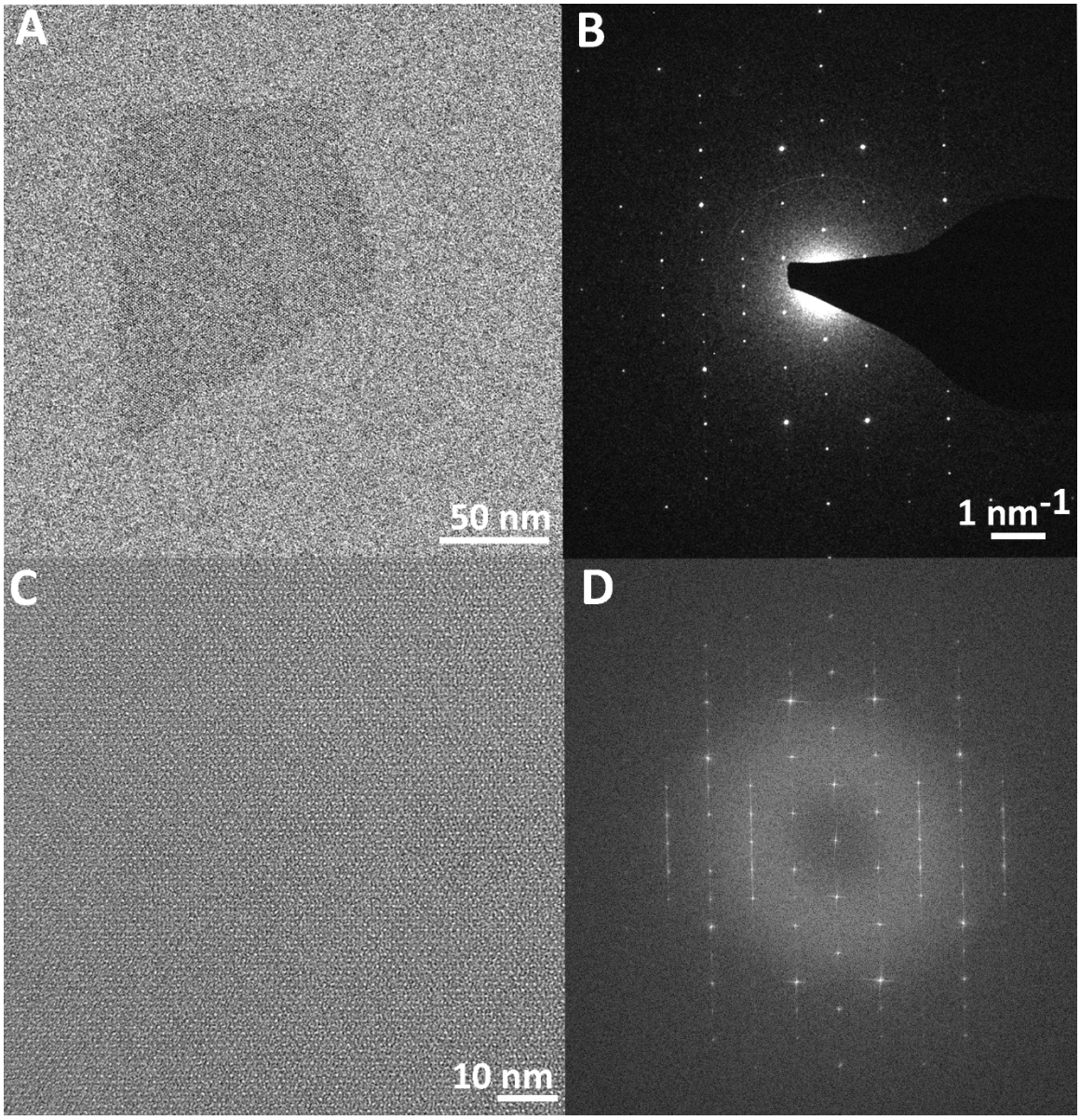

Fig 4.5. A: TEM image of *b*-oriented MFI-nanosheets purified from polystyrene and unexfoliated nanosheets by DGC. B: ED pattern from the MFI-nanosheet shown in (A). C: HRTEM image of a *b*-oriented MFI-nanosheet purified by DGC. D: The FFT of the HRTEM image in (C).

Fig. 4.6A shows a topographical AFM image of MFI-nanosheets deposited on a silicon wafer. The nanosheets lay flat on the silicon wafer owing to their high aspect ratio. A statistical analysis of the height distribution in the AFM data yielded that the MFI-

nanosheet is 3.21 ± 0.26 nm thick, corresponding to a 1.5 unit cell thickness along its *b*-axis. This along with a line scan data in Fig. 4.6B, is consistent with the thickness of MFI-nanosheets reported before.[82]

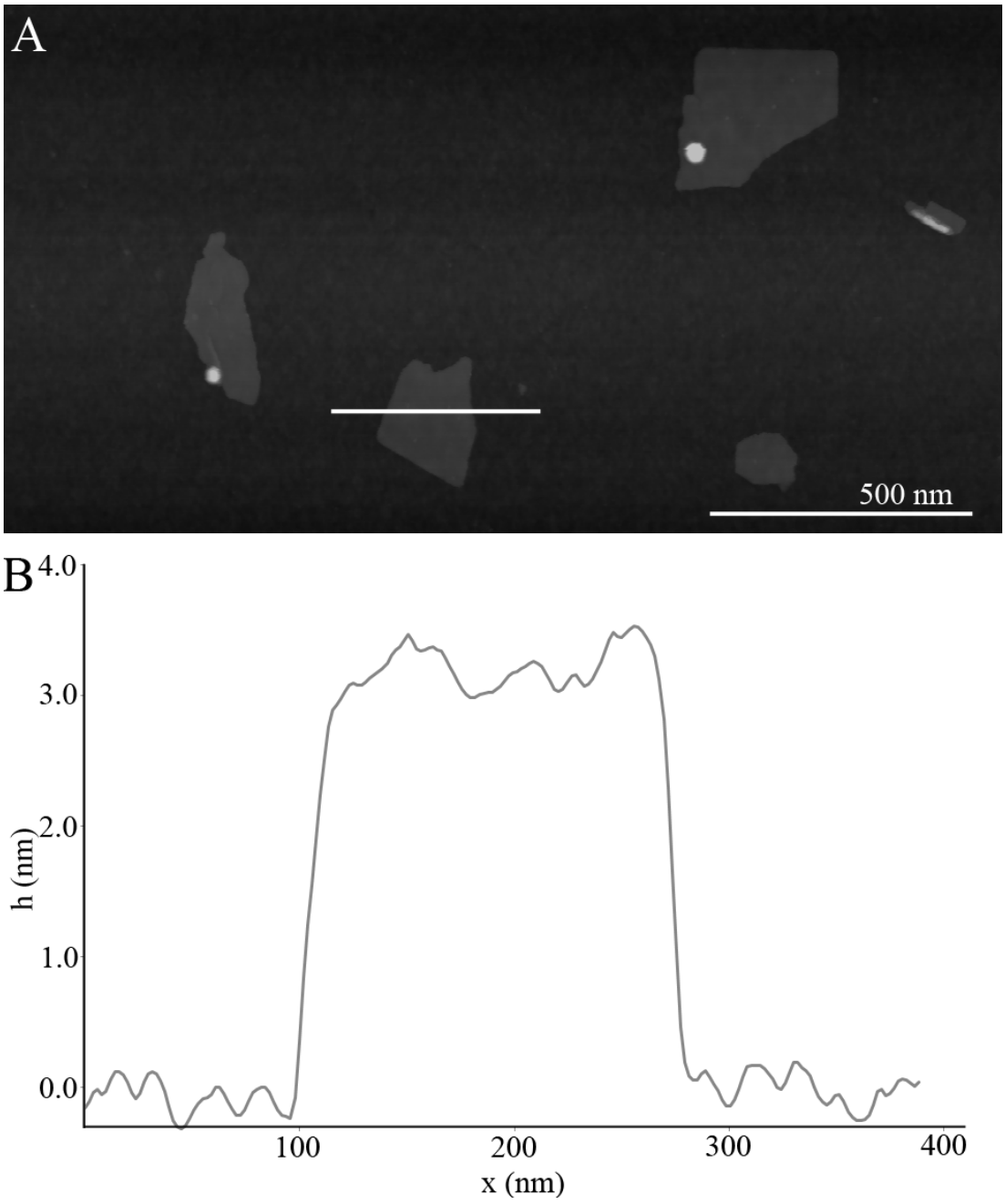

Fig 4.6. A: AFM (tapping mode) topographical image of MFI-nanosheets on Si wafer. B: Plot showing the topographical data (height vs. length) along the line scan across an MFI-nanosheet in (A).

4.4.2 Improved α-Alumina Support for Nanosheet Deposition

Purified nanosheets with high crystallinity are advantageous for fabrication of thin zeolite films for applications such as high throughput membranes. However, a smooth porous support with surface roughness less than the thickness of the desired zeolite film is essential for fabrication of a compact film. The alumina support fabricated by hydraulic pressing and sintering of 400 nm α-alumina particles had a surface roughness more than 500 nm even after polishing (Fig. 4.7A), making it extremely difficult to fabricate a sub-100-nm thick zeolite membrane without the use of an intermediate smoothening layer.[82] The high surface roughness in this support can be attributed to the poor packing of alumina particles as they are highly agglomerated in the powder form.

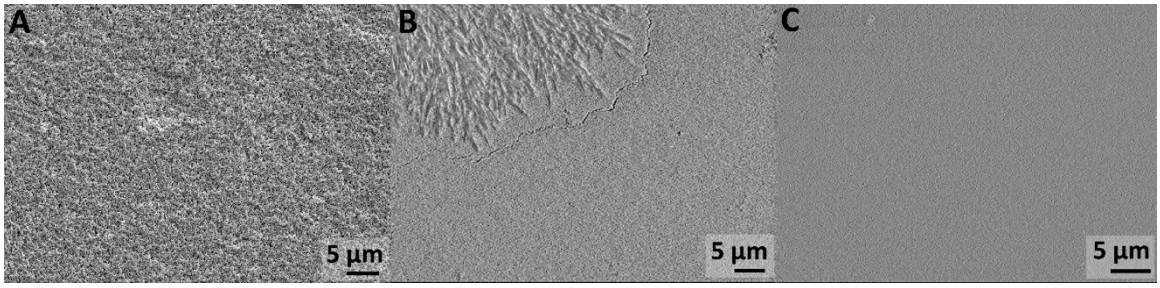

Fig 4.7. SEM images (top view) of the microstructure of α-alumina supports prepared by hydraulic pressing and colloidal dispersion processing. A: Rough surface microstructure of the support prepared by hydraulic pressing of α-alumina powder followed by sintering at 1160 ˚C and polishing. B: Surface of support prepared by casting the alumina suspension on gypsum mold and sintered at 1050 ˚C. C: Smooth surface of α-alumina supports prepared by vacuum assisted filtration of alumina suspension and sintered at 1050 ˚C.

To improve surface quality, supports were prepared from colloidal dispersions. Strong electrostatic repulsion between positively charged alumina particles is achieved in aqueous dispersions at pH in the 2-3 range[118]. The alumina suspension at pH 2.2 had many bubbles, which ruin the uniformity of the support surface (Fig. 4.8A), and hence, n-octanol was added as an antifoam agent to suppress the bubbles in the suspension[119, 120]. Fig. 4.7B shows an SEM image of the top surface of the alumina support prepared with the gypsum mold. The surface this support is much smoother than that made by powder pressing. The

improved surface quality may be attributed greater degree of dispersion of the particles in suspension as compared to the bulk powder. Additionally, the open mold process may have allowed the colloidal ceramic particles to accumulate on the flat air-water interface during casting. However, a significant deposition of gypsum derived $CaSO_4.2H_2O$ on the support surface made it difficult to use this support for ultrathin zeolite film. Fig. 4.7C shows an SEM image of the top surface of alumina support fabricated by vacuum assisted filtration. The surface roughness of this support is the lowest among the three supports due to controlled deposition and elimination of contaminants in the suspension.

Sintering of dispersion processed alumina supports at 1150 ˚C, the temperature typically used for sintering of the alumina disk prepared by hydraulic pressing of the alumina powder, led to partial closure of the surface pores (Fig. 4.8B). This result can be attributed to the higher packing density of the alumina particles in the dispersion-processed disk. Reduction of sintering temperature to 1050 ˚C led to a smooth and uniform surface microstructure, suited for the fabrication of ultrathin nanosheet films (Fig. 4.9A).

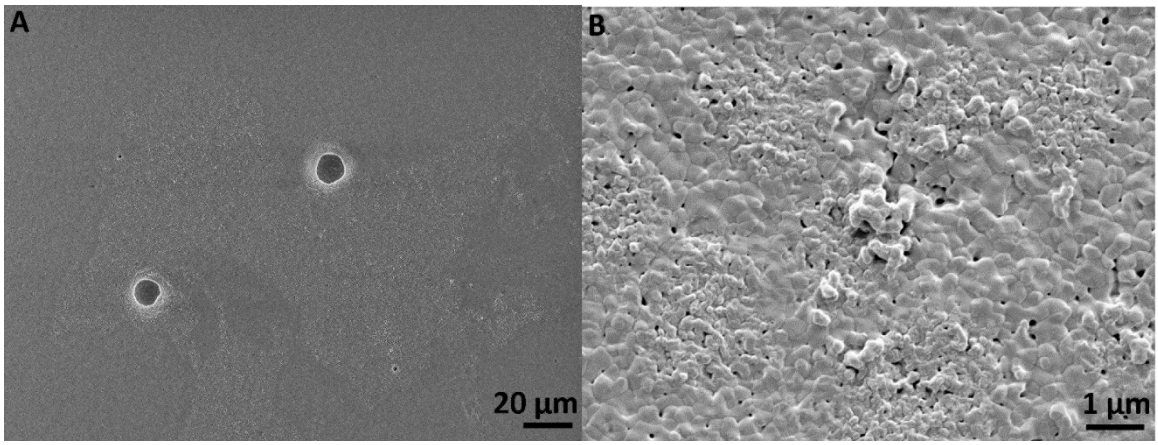

Fig 4.8. SEM images (top view) of the microstructure of α-alumina supports. A: Macro defects caused by the bubbles in the α-alumina suspension during vacuum assisted casting. B: Pore closure of highly packed alumina particles in the alumina support prepared by vacuum assisted casting due to sintering at 1150 ˚C.

4.4.3 MFI-nanosheet Film and Membrane

Fabrication of a uniform sub-100-nm thick nanosheet film on a porous support is a challenging task by traditional evaporation induced self-assembly (EISA) techniques such

as dip coating or convective assembly. Surface wettability issues combined with dripping of coated films, edge effects, and capillary infiltration in porous substrates, make it challenging to control the film thickness uniformly over the entire substrate. Also, EISA requires a fairly large quantity of coating suspension in a concentration of 0.1% or above. In contrast, filtration of nanosheet suspension through a porous substrate is a simple and reproducible technique capable of producing uniform, compact and oriented films.[82] Control of film thickness can be simply achieved by adjusting the amount of suspension added for the filter coating. Also, this technique does not require concentrated coating suspension, thereby allowing the use of dilute nanosheet suspensions.

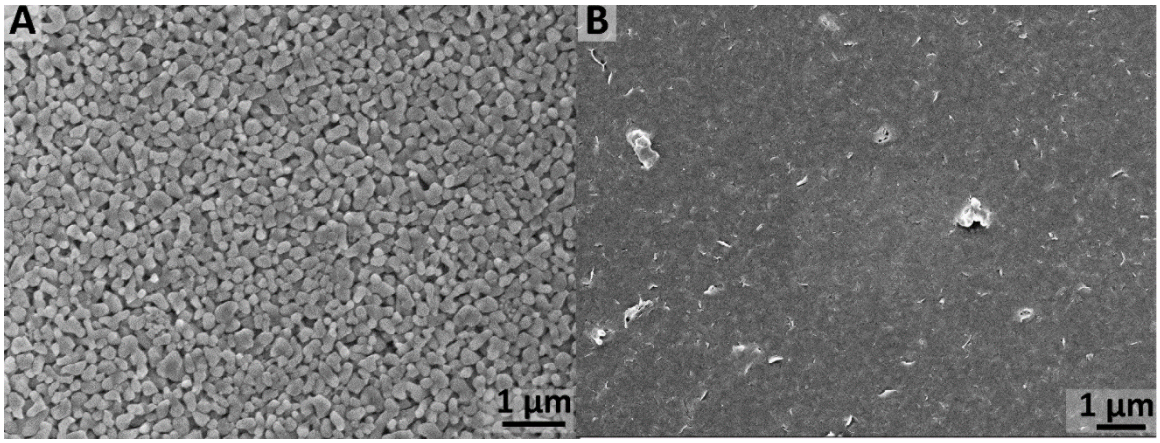

Fig 4.9: A: SEM image of the surface of alumina support prepared by vacuum assisted filtration and sintered at 1050°C. B: SEM image of the surface of support coated with a thin film of MFI-nanosheets.

A thin film of MFI-nanosheets was coated on the high quality α-alumina support by vacuum assisted filtration of the purified nanosheets suspension (Fig. 4.9B). The coating was heat-treated at 540 ˚C to remove the OSDA, and promote interparticle bonding by condensation of terminal silanol groups at the surface of nanosheets. Fig. 4.10A shows a high magnification SEM image of the top surface of the coating. MFI-nanosheets cover the entire support while orienting themselves along their *b*-axis. *b*-orientation of MFI film is advantageous for fabrication of a high throughput membrane, as the fastest transport channel in the MFI crystal is along the b-axis[13, 15]. Although the nanosheet film is compact, interparticle gaps of a few nm can be observed. These gaps could be due to the presence of a few agglomerated nanosheets in the coating suspension or curling of larger nanosheets

during deposition. Future work will focus on fractionation of nanosheets based on their lateral size to further improve the packing of nanosheets in the coated film. Fig. 4.10B shows the cross section of the nanosheet film prepared by FIB. The nanosheet film sandwiched between α-alumina support and the protective gold coating is 80 nm thick. The nanosheet coating follows the surface contour of the underlying α-alumina support owing to the flexibility of high-aspect-ratio nanosheets.

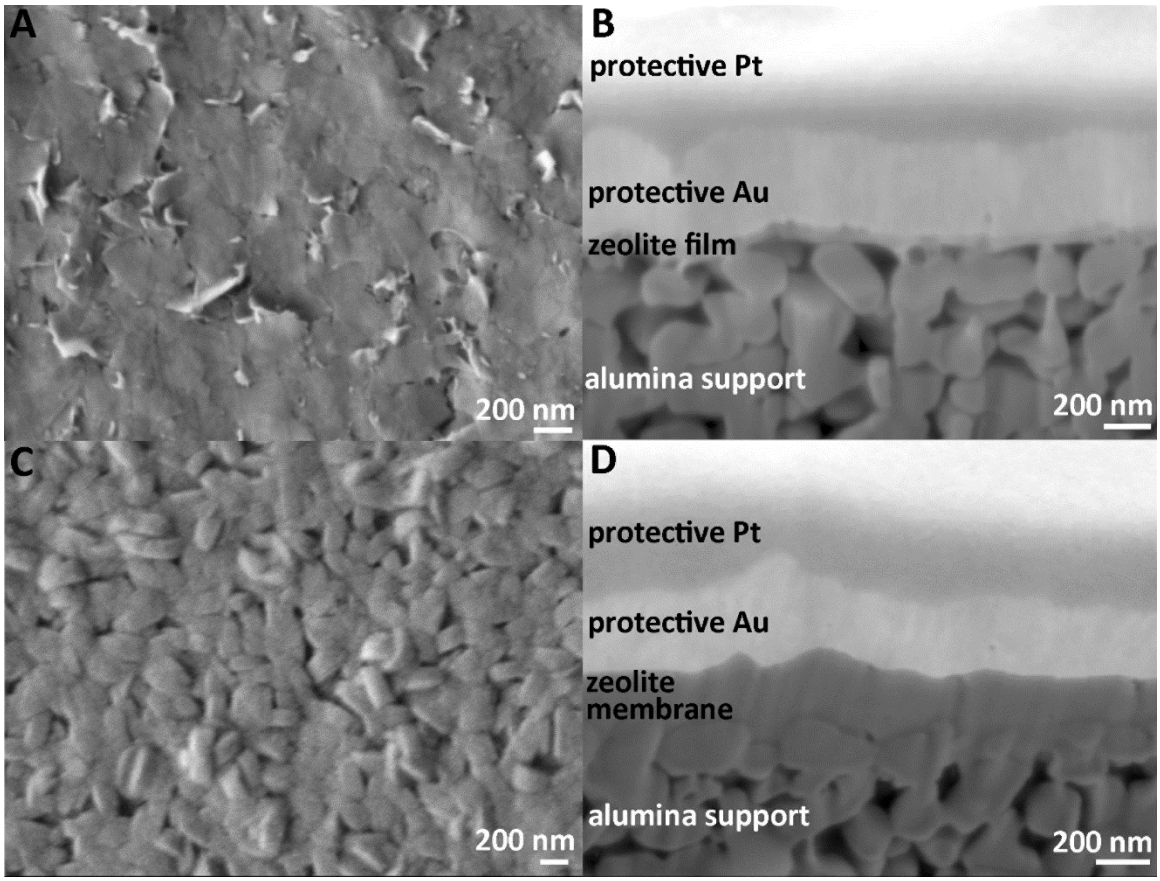

Fig 4.10. SEM images of the MFI-nanosheet films and their cross-section prepared by FIB. A: Top view image of MFI-nanosheet film on the α-alumina support. B: Cross-sectional image of the film shown in (A), acquired at a tilt angle of 48 degrees. C: Top view image of membrane prepared by secondary growth of nanosheet film shown in (A). D: Cross-sectional image of the membrane shown in (C), acquired at a tilt angle of 40 degrees. The protective gold and platinum coatings are deposited to prevent beam-damage to the film/membrane surface during preparation of cross-sections by FIB.

Molecular sieving performance of the MFI-nanosheet film was tested by permeating an equimolar mixture of *p*-xylene and *o*-xylene through the film[13, 15, 30]. MFI

nanosheets have pore openings of 0.56 nm X 0.54 nm along their *b*-axis, whereas the kinetic diameter of *p*-xylene and *o*-xylene are 0.58 nm and 0.68 nm, respectively. However, due to presence of many interparticle gaps in the nanosheet film, separation of smaller *p*-xylene molecules did not take place, indicating a dominant contribution of flow through the larger interparticle gaps created during nanosheet coating. Mild secondary growth of this film, as per previously reported growth method[82], led to reduction in the interparticle defects in the zeolite film. Fig. 4.10C shows an SEM image of the top surface of the secondary-grown film after calcination. The microstructure of the film suggests twinning of zeolite nanosheets leading to growth of *a*-oriented MFI crystal. Similar twinning has been reported earlier in these growth conditions[30]. Fig. 4.10D shows an SEM image of the cross-section of the membrane prepared by FIB, indicating that the nanosheet film grew from 80 nm to 200 nm during the hydrothermal treatment. The increase in thickness of the nanosheet film is due to twinning and subsequent growth of *a*-oriented MFI crystals. Four membranes prepared by this method, separated an isomolar mixture of *p*-xylene and *o*-xylene with separation factor of 25-45, and *p*-xylene permeance of 4 X 10^{-7} moles/m^2-Pa-s (~375 kg/m^2-day-atm) at 150 ˚C. The *p*-xylene permeance through the nanosheet membrane was similar to that of the alumina support.

4.5 Summary

These findings indicate that a nonlinear density gradient of organic solvents can be used to purify exfoliated MFI-nanosheets prepared by melt compounding of multilamellar MFI. Excessive polystyrene present in the nanosheet suspension was removed by DGC of the suspension across chlorobenzene. Rate-zonal centrifugation of nanosheets, in a multilayered density gradient, separated exfoliated nanosheets from larger unexfoliated particles. ED and HRTEM imaging of the purified MFI-nanosheets indicated that exfoliated MFI-nanosheets obtained by this process were highly crystalline. A simple filtration of purified nanosheets through improved quality porous supports led to fabrication of an 80-nm-thick MFI-nanosheet film, which upon a secondary growth to 200-nm-thick film exhibited molecular sieving capabilities for xylene isomers.

Chapter 5: In-plane Growth of MFI-nanosheet Films for High Throughput Membranes

*To be submitted.

5.1 Introduction

An oriented MFI membrane is desirable for achieving maximum throughput of gas and vapor molecules through the MFI film.[13] As shown in Fig 5.1, MFI has straight channels along its *b*-axis and sinusoidal channels along the a-axis.[30] The 0.54 nm x 0.56 nm straight channels are interconnected with the 0.51 nm x 0.55 nm sinusoidal channels. Therefore, a *b*-oriented MFI film is ideal for achieving a high throughput membrane.

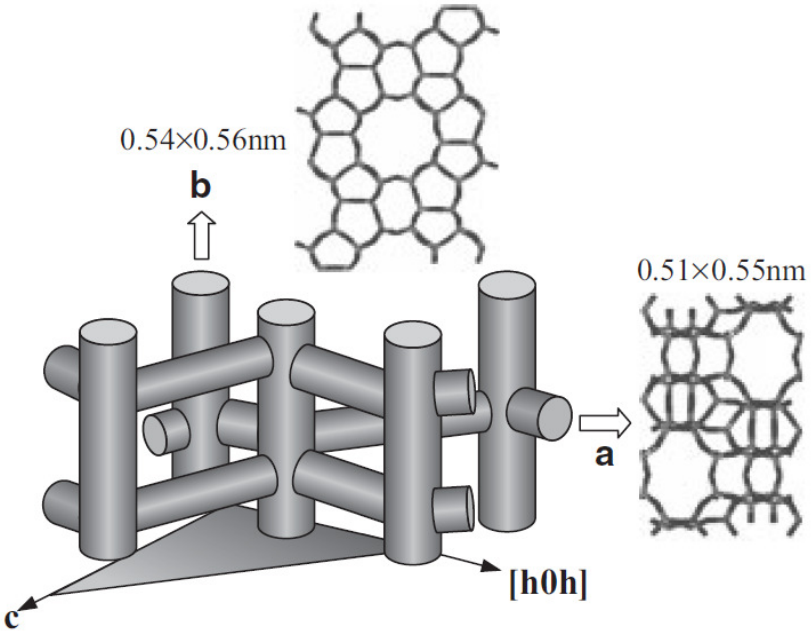

Fig 5.1. The straight and the sinusoidal channels of MFI along *a*- and *b*-axis, respectively[30].

One of the prerequisites for fabricating a *b*-oriented MFI film by the seeded growth method is a *b*-oriented MFI seed layer. However, the fabrication of an oriented MFI seed layer is not straightforward. In past, this has been achieved by a slow dip coating process[121], functionalization of the support surface[122], rubbing MFI crystals on a bare or a modified

support surface,[123] controlled evaporation of a MFI monolayer on the air-water interface[124-126], etc. However, most of these coating techniques are difficult to scale up for the large scale production of *b*-oriented MFI films. A simple and scalable method for the fabrication of *b*-oriented MFI films is the filter-assisted coating of the MFI-nanosheets.[82, 127] Filter coating is an attractive technique as it can deposit sheet like particles on supports with a high surface roughness. However, the MFI nanosheet film deposited by filter coating could not separate molecules due to the presence of void spaces between nanosheets. The void spaces in the compact film of nanosheets are expected to be smaller than that in a film of isotropic particles. A hydrothermal treatment of nanosheets in the MFI film is necessary to eliminate the void spaces. Hydrothermal treatment of the nanosheet films in a C6 solution led to the growth of undesired *a*-oriented MFI crystals on top of the *b*-oriented MFI nanosheet film[127]. This necessitated the development of a technique to achieve an in-plane growth of the *b*-oriented MFI nanosheet seed layer.

The in-plane growth of *b*-oriented MFI films is difficult due to twinning of MFI crystals during the secondary growth. An in-plane growth of the *b*-oriented MFI film was first reported by using a specially designed OSDA, trimer-TPAOH (bis-N,N-(tripropylammoniumhexamethylene) di-N,N-propylammoniumtrihydroxide)[13, 30]. This OSDA preserved the orientation of MFI crystals in the seed layer by increasing the crystal growth rate along the *b*-axis. However, a small amount of randomly oriented MFI crystals always deposit on top of the seed layer during the secondary growth.[15] Moreover, the use of trimer-TPAOH for the growth of the *b*-oriented MFI nanosheet film did not lead to an oriented, perm-selective membrane (Fig. 5.2). In the case of a short hydrothermal treatment, the inter-particle gaps between nanosheets did not close, and, in the case of longer hydrothermal treatment, randomly oriented MFI crystals appeared on the surface of the seed layer.

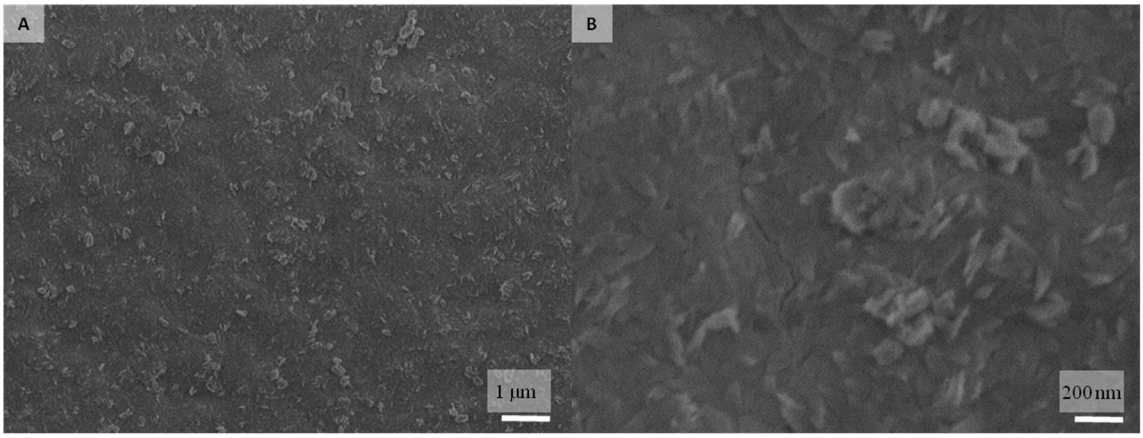

Fig 5.2. Secondary growth of a *b*-oriented MFI nanosheet film using trimer TPAOH as OSDA. Growth was carried out at 120 ºC for 32 hours. The growth gel composition was 30SiO_2: 3trimer TPAOH: 8100$H_2$0: 120EtOH.

Fabrication of a *b*-oriented MFI film using TPAOH as an OSDA in an optimized growth composition (5SiO_2:1TPAOH:1000H_2O:20EtOH) was reported recently.[124] The *b*-oriented MFI film was grown on a smooth non-porous glass plate. However, till date, there are no reports of a *b*-oriented MFI film prepared using this method on a porous support. A secondary growth of an 80-nm thick film of DGC purified MFI-nanosheets deposited on an alumina support, by this method, led to a non-oriented MFI film (Fig. 5.3). This film separated an equimolar mixture of *p*- and *o*-xylene with a moderate separation factor of 20 and exhibited a *p*-xylene permeance of 2 x 10^{-7} moles/m^2-s-Pa.

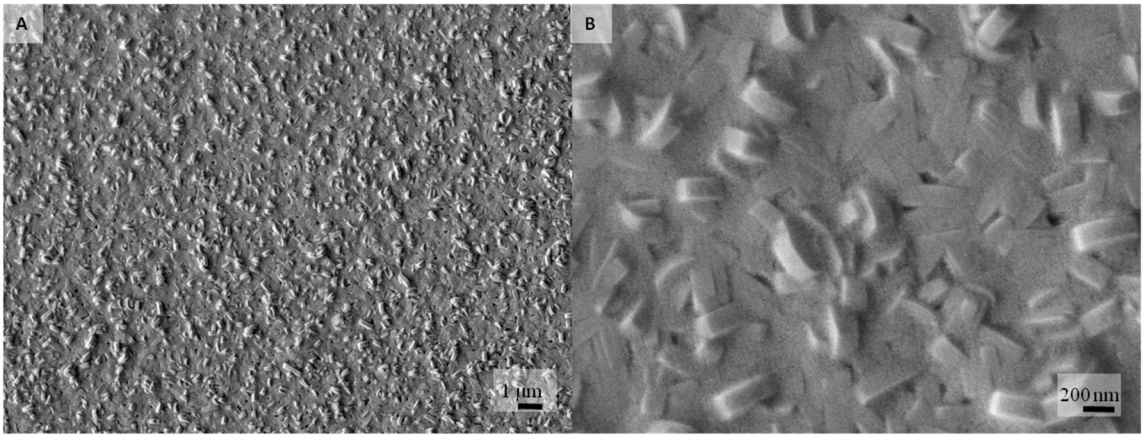

Fig 5.3. Secondary growth of MFI-nanosheet film using the optimized growth conditions reported by Liu et al.[124] The film was grown at 150 ºC for 3 hours.

Recently, Yoon and co-workers reported in-plane growth of *b*-oriented MFI films using a growth gel comprising of ammonium hexafluorosilicate [$(NH_4)_2SiF_6$].[15] The oriented growth was attributed to the absence of bulk nucleation in the growth gel. More recently, the same research group came up with a method of achieving *b*-oriented secondary growth by a gel-less impregnation approach[128]. In this approach, *b*-oriented MFI seed layer deposited on a porous silica support, is impregnated with a dilute TPAOH solution. This is followed by heating of the impregnated supports, which leads to a *b*-oriented MFI film. Once again, the oriented growth was attributed to the absence of bulk nucleation, as no growth gel was used during the heat treatment step. In this chapter, the growth behavior of the *b*-oriented MFI-nanosheet films using $(NH_4)_2SiF_6$ gel and the impregnation growth method is investigated.

5.2 Growth of MFI-nanosheets in Gel Containing $(NH_4)_2SiF_6$

In-plane growth of *b*-oriented MFI crystals was reported by Pham et al. using a semi-solid growth gel. This gel was prepared by mixing TEOS, TEAOH and $(NH_4)_2SiF_6$ in the following stoichiometric ratio -4 SiO_2: 1.92 TEAOH: 0.36 $(NH_4)_2SiF_6$: n H_2O: 16 EtOH, where n varied from 40-80 (Fig. 5.4).[15] Inspired from this, the growth behavior of *b*-oriented MFI-nanosheets in these growth conditions was studied. Growth gels comprising of different OSDA such as tetramethyl ammonium hydroxide (TMAOH) and tetrabutyl ammonium hydroxide (TBAOH) were also investigated to understand the effect of OSDA on the growth of MFI nanosheets.

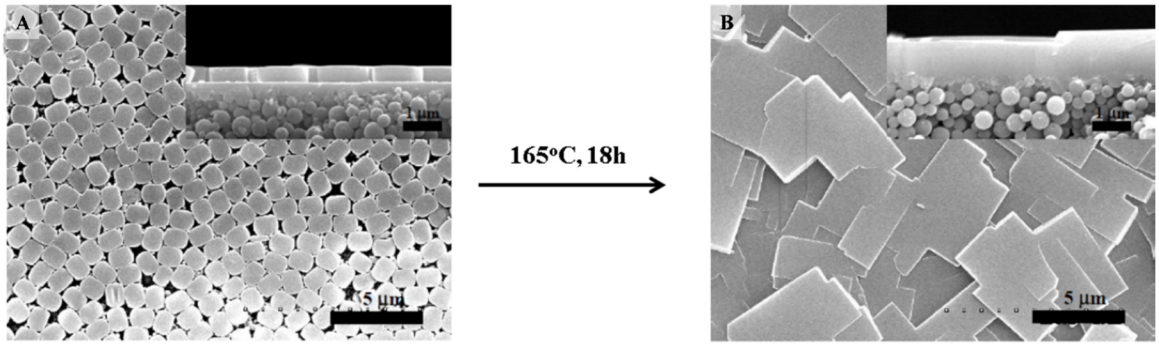

Fig 5.4. In-plane growth of *b*-oriented MFI seed layer using growth gel incorporating $(NH_4)_2SiF_6$. [15] Reprinted with permission from AAAS.

Early stages of the growth of MFI-nanosheets were investigated using MFI-nanosheet crystals coated on a Si wafer. For this, DGC purified MFI nanosheets were spin coated on a Si wafer and calcined at 540 ºC to remove the OSDA (Fig. 5.5A). The growth conditions were rigorously studied by varying growth parameters: the temperature, the growth time and the water concentration in the gel. Fig. 5.5A and B show the SEM images of MFI nanosheets grown in a dilute gel (n H_20 = 100) for 3 days at 100 ºC and 115 ºC, respectively. The growth of the nanosheets at 115 ºC was much higher than the growth observed at 100 ºC. In both cases, the orientation of MFI was preserved and the growth was always in-plane. The growth along the *c*-axis seemed somewhat higher than the growth along the *a*-axis. Also, some of nanosheets grew more than others in both cases. Fig. 5.6B shows an AFM image of the MFI-nanosheets grown in a dilute growth gel for 1 day at 100 ºC. The bright spherical spots in Fig. 5.6B are amorphous silica from the secondary growth step. Fig. 5.6 shows the nanosheet seed before the secondary growth (Fig. 5.6A). From the comparison of AFM images before and after secondary growth, it is evident that the sharp edges of MFI nanosheet became rounded after the secondary growth. The thickness of MFI nanosheet did not change during this mild secondary growth.

Fig. 5.5C and D show the growth of MFI nanosheets in a concentrated gel (n H_20 = 40) at 150 ºC for 6 hours and 1 day, respectively. Needle-like growth was observed in either cases as the growth along the *c*-axis was much higher than the growth along the *a*-axis. Similar to MFI nanosheets grown in the dilute gels, not all nanosheets grew to the same extent. An interesting growth phenomena was observed, in which the growth along the *c*-axis seemed to be disproportionate (Fig. 5.5C and D). Interestingly, the growth of the MFI seed layer reported by Pham et al. (Fig. 5.4B) also had somewhat disproportionate growth along their *c*-axis.[15]

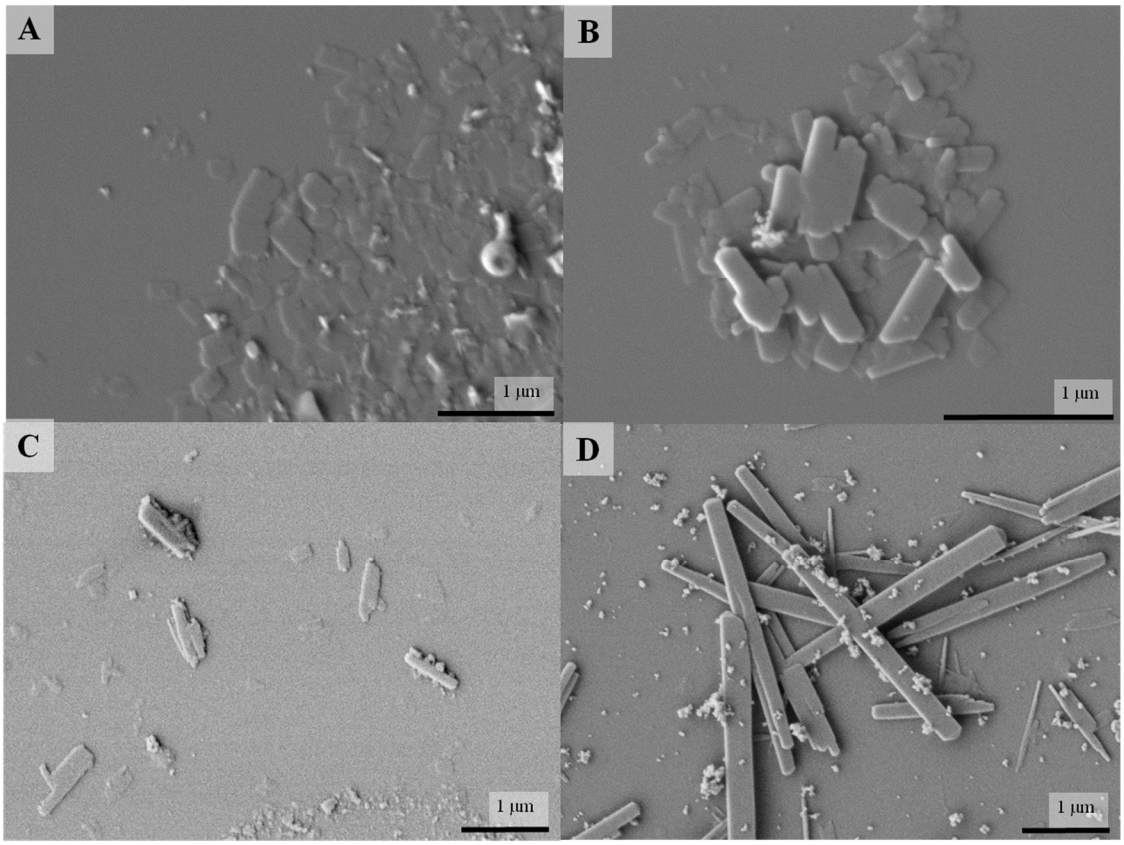

Fig 5.5. A: Growth of MFI nanosheets by the dilute growth gel (n H_20 = 100) at 100 ºC. B: Growth in the dilute gel at 115 ºC. C: Growth in the concentrated gel (n H_20 = 100) for 6 hours. D: Growth in the concentrated gel for 24 hours.

The growth of *b*-oriented MFI-nanosheet film on porous supports was also investigated using $(NH_4)_2SiF_6$ gel. Porous alumina supported MFI-nanosheet films did not grow using these growth gels. This could be due to the leaching of alumina in the growth gel leading to the deactivation of the gel. In order to overcome this problem, porous silica supports prepared according to the method reported by Pham et al.[15] was used as to deposit the MFI nanosheet seed layer. Fig. 5.7B shows an SEM image of the cross-section of the asymmetric silica support, revealing a thin coating of 50 nm silica spheres on top of larger (300-500 nm) silica spheres. The surface of the silica supports was very smooth due to the 50 nm silica layer. Hence, an ultrathin coating of MFI-nanosheets could be easily deposited using the filter assisted coating by simply reducing the amount of nanosheets in the coating suspension. Fig. 5.7C shows a thin, *b*-oriented coating of MFI nanosheets on the

asymmetric silica support. The cross-sectional specimen prepared by the FIB technique revealed that this film was approximately 80 nm thick (Fig. 5.7D). Fig. 5.7E and F show the *b*-oriented MFI nanosheet films with thicknesses of approximately 30 nm and 3-10 nm, respectively. These ultrathin coatings of *b*-oriented MFI nanosheets are promising for the fabrication of highly desired sub-50 nm thick zeolite membranes.[80]

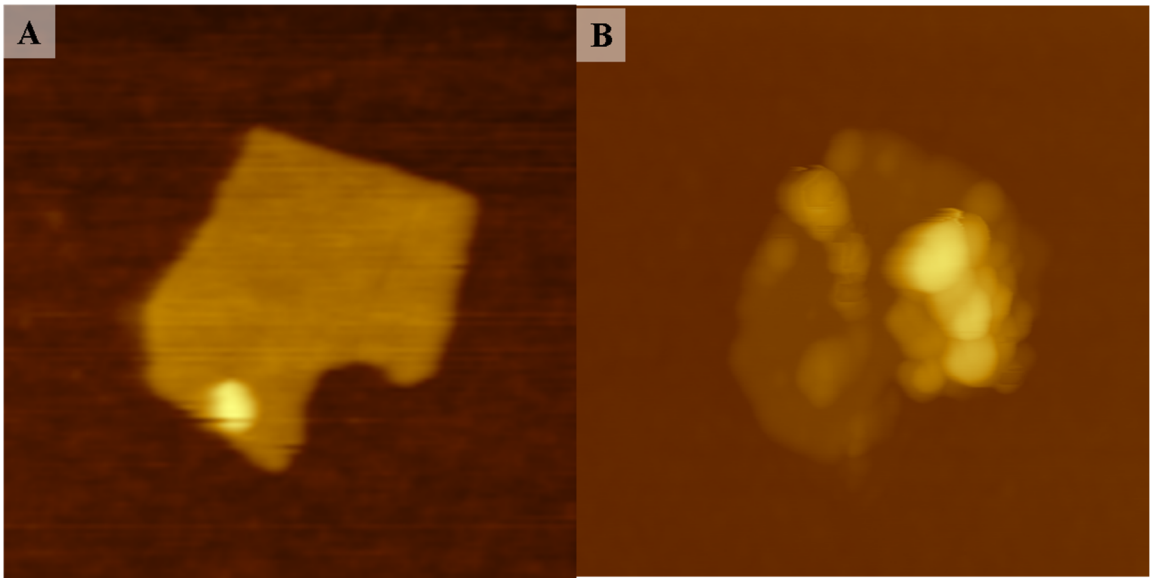

Fig 5.6. A: AFM image of an MFI-nanosheet. B: AFM image of MFI nanosheet in (A) after the secondary growth in the dilute gel at 100 ºC for 1 day.

80-nm thick MFI nanosheet films were grown on silica supports using both the dilute (n H_20 = 100) and the concentrated growth gels (n H_20 = 40). In a typical growth experiment, the growth gel was prepared by stirring the stoichiometric amount of reactants in a polypropylene beaker. After stirring for 4 hours, the gel was agitated with a food blender for 2 minutes. About 15 ml of the gel was filled in a Teflon-lined stainless steel autoclave. Then, the silica support coated with the *b*-oriented MFI nanosheet film was pushed vertically inside the gel. Another 5 ml of the growth gel was filled in the Teflon liner and the gel was pressed to ensure good contact with the MFI seed layer.

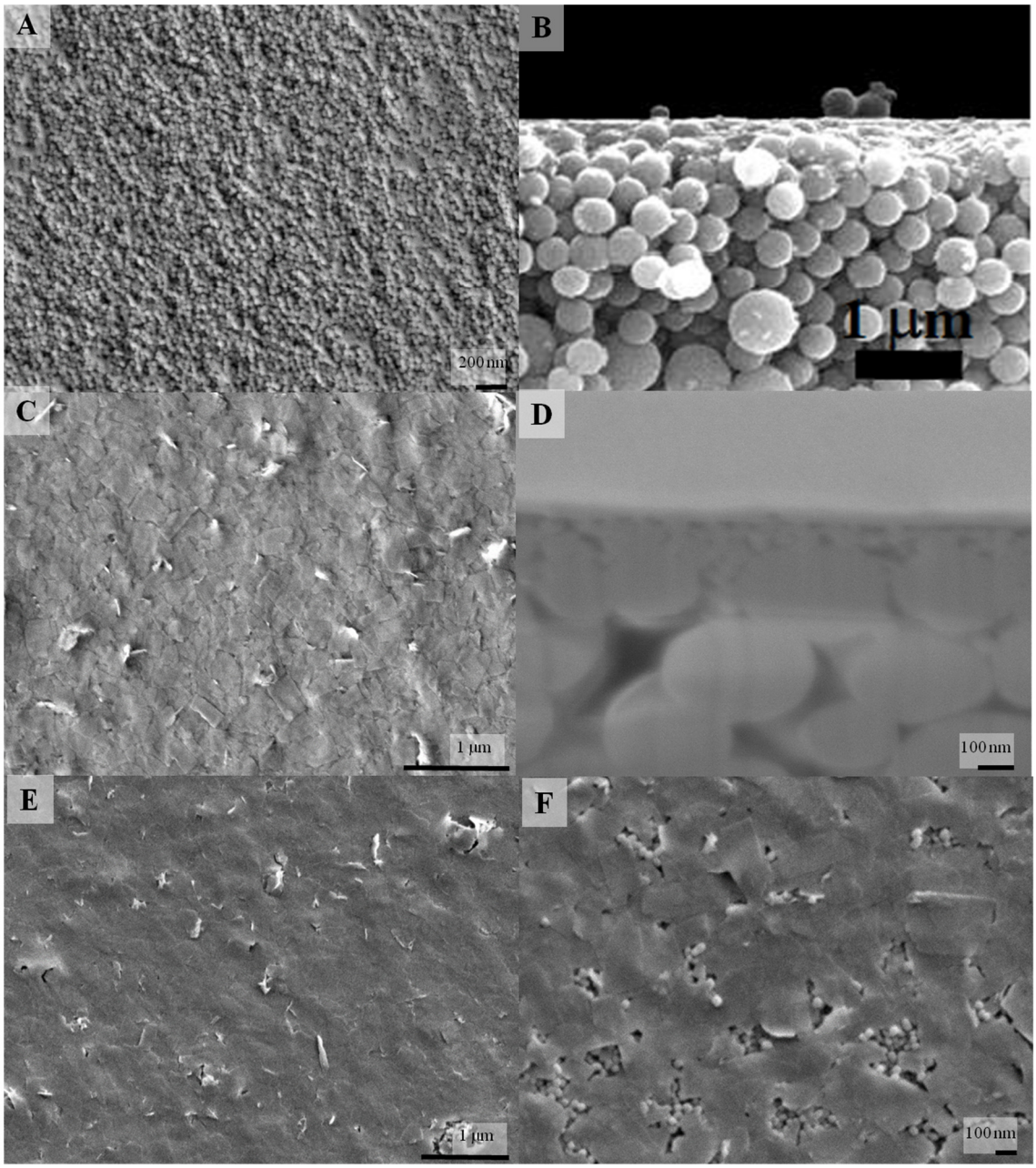

Fig 5.7. A: Surface microstructure of a silica support. B: Cross-sectional image of a silica support showing a very thin coating of 50 nm sized nanoparticles on the surface of the support (image reproduced from Pham et al. [15] C: Filter coating of MFI nanosheets on a silica support. D: Cross-section of nanosheet coating shown in C, revealing ca. 80 nm thick film of MFI-nanosheet. E: An approximately 30 nm thick coating of MFI nanosheets. F: An approximately 3-10 nm thick coating of MFI nanosheets.

The autoclave was sealed and heated to the desired temperature in an oven. The secondary growth took place during the heat treatment. After heating for a specific time,

the autoclave was cooled to room temperature and the membrane was rinsed by washing with deionized water. To remove the amorphous silica from the growth gel, the membrane was soaked in 0.2M NH_4F solution for 4 hours. Following this, the membranes was calcined at 480 ºC for 4 hours with heating and cooling rates of 30 ºC/hour.

The secondary grown membranes were characterized by SEM and by the permeation studies of xylene isomers. In the case of dilute growth gel (115 ºC for 3 days), a very small growth was observed (Fig. 5.8A and B). This growth was not sufficient to eliminate the interparticle gaps and hence, these films did not separate *p*-xylene from *o*-xylene. A few large MFI crystals (length along *c*-axis~ 1 µm) were present on the surface of the film. This could be due to the depletion of growth nutrients in the gel in the vicinity of these growing MFI crystals. The nanosheet edges were rounded. The thickness of the nanosheets had increased, as evident from the thickness of a few out-of-plane crystals. These observations are consistent with the growth behavior of the MFI-nanosheets on Si Wafers (Fig. 5.6A and B). To increase the growth of the nanosheets, the growth temperature and the heating time were increased. However, the growth of MFI-nanosheets in the dilute gel at elevated temperatures for longer times (175 ºC for 4 days) did not improve the separation performance. Again, a few very large crystals were observed on the surface of the MFI film (Fig. 5.8C and D). This indicates to crystal growth in a growth gel depleted of nutrients. Depletion can be attribution to the high viscosity of the growth gel, which might have reduced the diffusion of the growth nutrients.

To improve the intergrowth of MFI nanosheets and to reduce the interparticle gaps, MFI nanosheet film was grown using a concentrated growth gel (n H_20 = 40) at 150 ºC. As shown in Fig. 5.9, the growth of MFI nanosheets in the concentrated gel was much higher than that in the dilute gel. Hydrothermal treatment at 150 ºC for 20 hours (Fig. 5.9A and B) led to in-plane growth of MFI nanosheets. Many large *b*-oriented MFI crystals could be seen on the surface of the secondary grown film. However, this film could not separate *p*-xylene from *o*-xylene indicating an incomplete elimination of interparticle gaps. In order to completely remove the interparticle gaps, the MFI-nanosheet seed layer was grown in a concentrated growth gel for a longer period of time. Hydrothermal treatment at 150 ºC for

3 days led a film which separated *p*-xylene from *o*-xylene with a separation factor of 5, and a *p*-xylene permeance of 3 x10^{-7} moles/m^2-Pa-s. Fig. 5.9C and D show the microstructure of this film. As revealed by these SEM images, this film is no longer *b*-oriented. Large out-of-plane MFI crystals could be seen on the surface of the film.

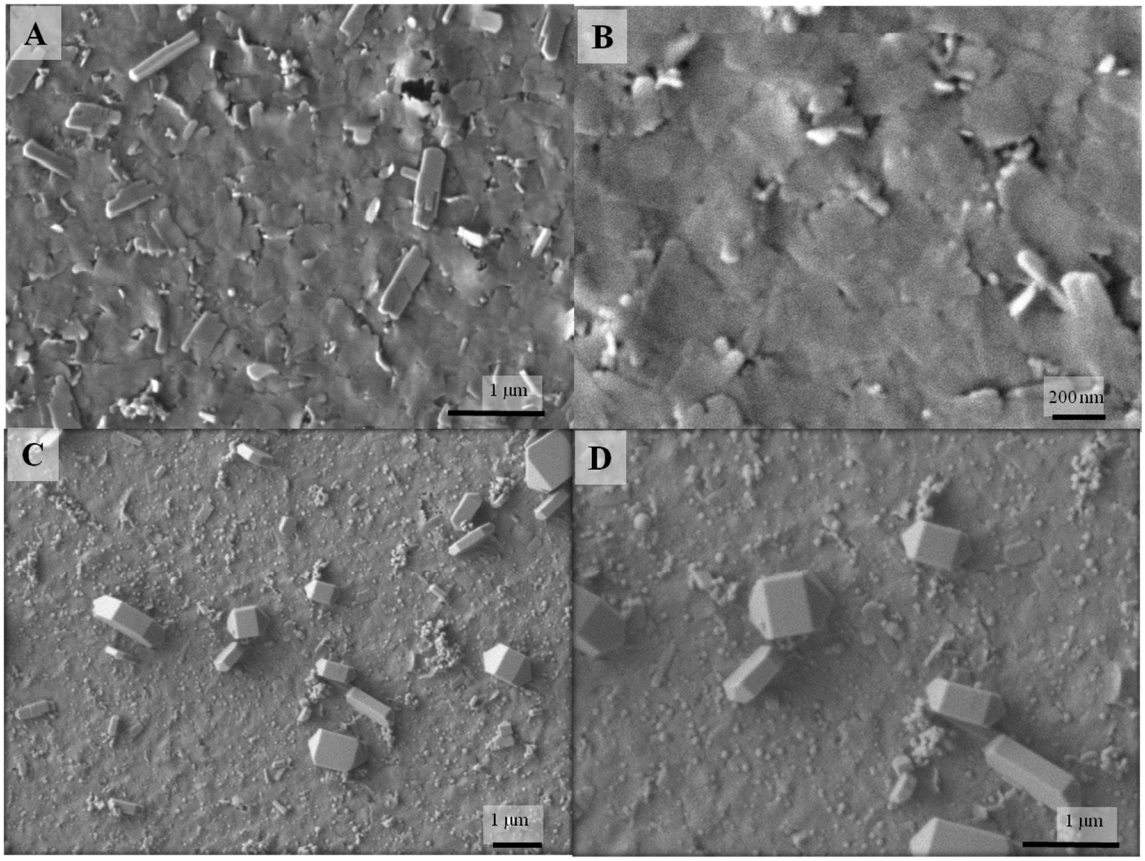

Fig 5.8. SEM images of MFI-nanosheet film on porous silica support after secondary growth in the dilute gel. A, B: Secondary growth at 115 ºC for 3 days. C, D: Secondary growth at 175 ºC for 4 days.

Hydrothermal treatment of the MFI nanosheet film in concentrated growth gel for a longer time (4 days) improved the sieving performance of the film. This film separated *p*-xylene from *o*-xylene with a separation factor of 300, and a *p*-xylene permeance of 3 x 10^{-7} moles/m^2-Pa-s. However, the film microstructure comprised of randomly oriented MFI crystals (Fig. 5.9E). Growth for even longer time (5 days) led to the formation a very thick, randomly oriented MFI film (Fig. 5.9F).

The growth behavior of the MFI nanosheet film in the ammonium fluorosilicate gel comprising of a different OSDA, was also investigated. MFI-nanosheet films were grown in gels containing TMAOH and TBAOH. The growth of MFI-nanosheets with TMAOH (Fig. 5.10A) as the OSDA was much less compared to its growth in TBAOH (Fig. 5.10B). Some nanosheets grew into large crystals, whereas a few nanosheets seemed to etch away, indicating that the growth gel was not optimum. In the case of TBAOH containing gel, MFI nanosheet film grew as long needles leading to a non-compact film. Based on these observations, growth of MFI-nanosheets in a concentrated gel containing TEAOH as the OSDA seemed to be the best route for making molecular sieving membranes.

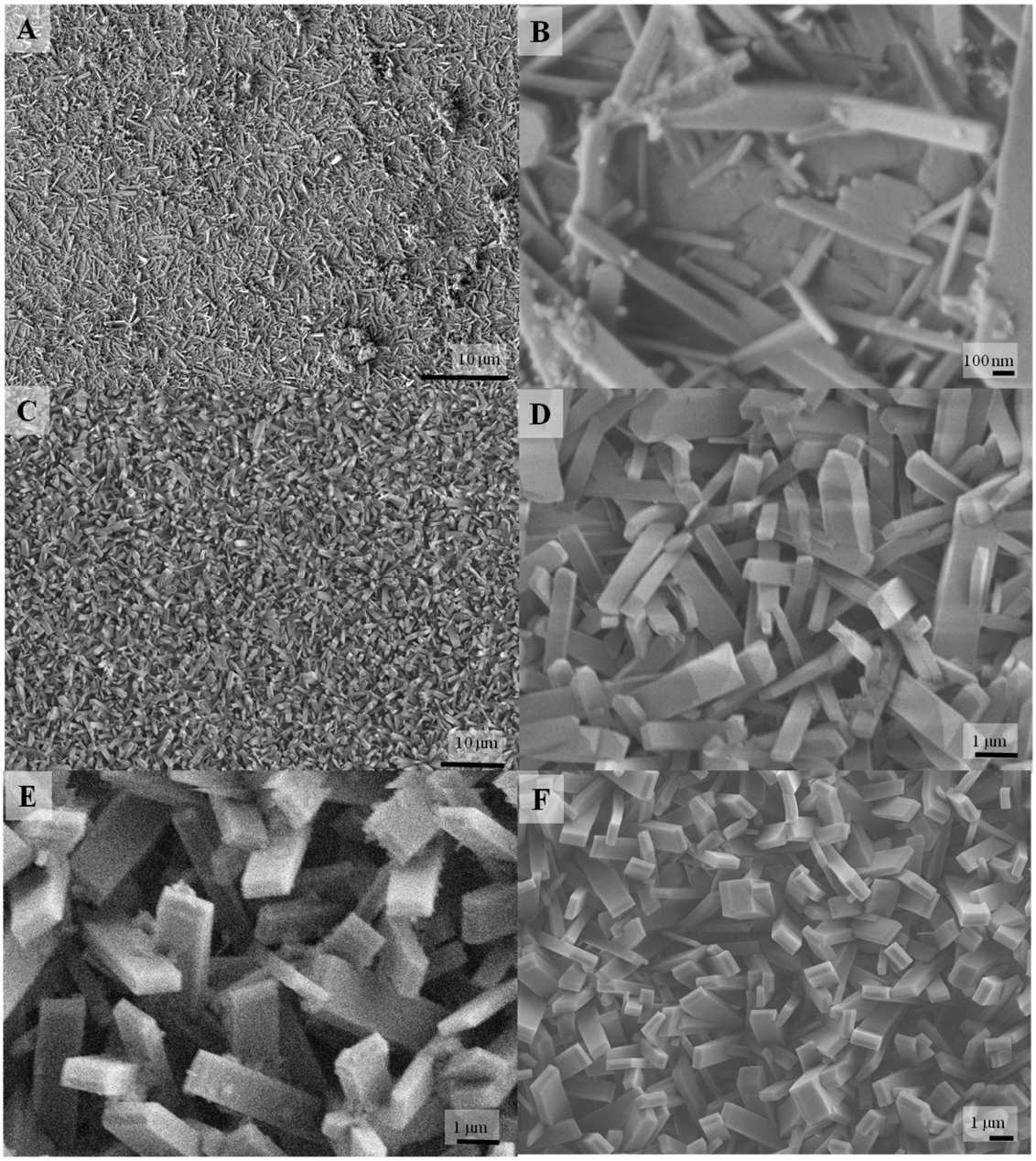

Fig 5.9. Growth of MFI-nanosheets in the concentrated growth gel at 150 ºC. A, B: Secondary growth for 20 hours. Secondary growth for 3 days is shown in (C) and (D), whereas, secondary growth for 4 and 5 days is shown in (E) and (F), respectively.

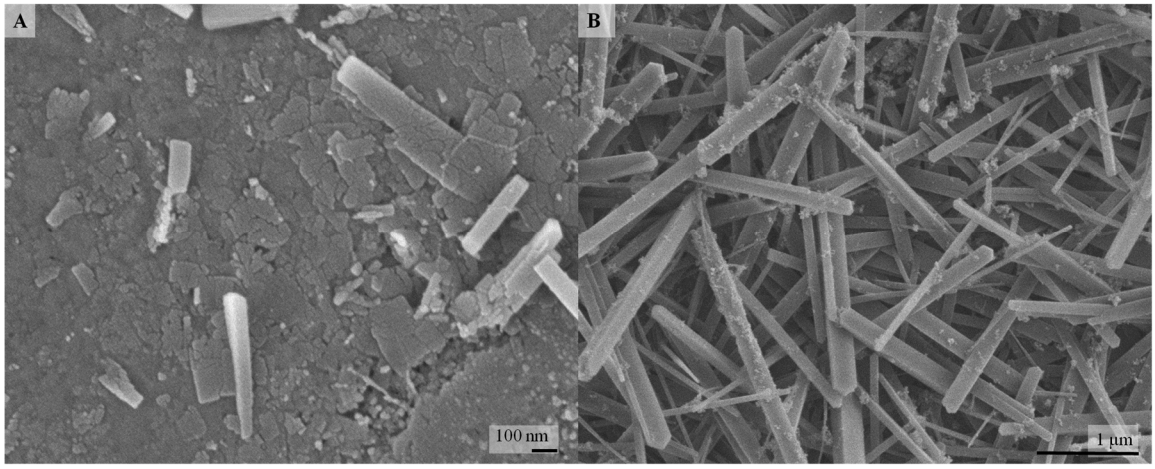

Fig 5.10. A: Secondary growth of MFI-nanosheet film on a porous silica support using TMAOH as OSDA. B: Secondary growth using TBAOH as OSDA.

5.3 In-plane Growth of MFI-nanosheets using Impregnation of OSDA

MFI-nanosheet films were grown by a recently reported impregnated growth method[128]. In a typical growth experiment, a *b*-oriented MFI nanosheet film was impregnated with a dilute OSDA solution for a specific amount of time as shown in the schematic in Fig. 5.11. The silica nanoparticle layer sandwiched between MFI nanosheet film and the silica support acts as the silica source for the secondary growth of MFI nanosheets. After impregnation, the MFI seed film was dried in air for 5 seconds and then placed in a Telfon lined stainless steel autoclave. The autoclave was sealed and then heated to 190 ºC for a period of 24- 48 hours. The secondary growth took place during this heat treatment. After completion of heating, the MFI membrane was taken out of the autoclave and calcined at 480 ºC for 4 hours with a heating and cooling rate of 30 ºC/hour. The MFI membranes were characterized by SEM and by permeance studies of xylene isomers (*p*- and *o*-xylene).

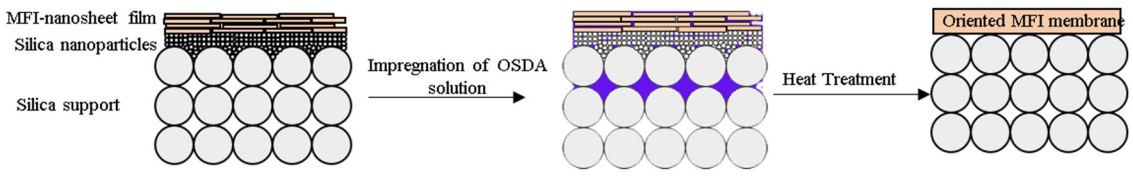

Fig 5.11. Schematic of the impregnated growth technique on a *b*-oriented MFI nanosheet film on the porous silica support.

Fig. 5.12 shows the SEM images of the MFI membrane made by the impregnation growth performed at 190 ºC for 24 hours. Impregnation was done by soaking a MFI-seed layer in a 0.025M TPAOH solution for 40 seconds. As evident from the surface morphology, in-plane growth did take place. The growth appeared uniform (Fig. 5.12A). Many large MFI crystals alongside small sheet-like crystals grew on the surface of the MFI film (Fig 5.12B and C). However, there were area in the film which did not grow at all (Fig. 5.12D). This could be due to the presence of over-sintered (partially closed) area in the silica support, which remained uncoated by filter assisted coating of MFI nanosheets. No MFI crystals were visible in these area due to the absence of a seed crystal. As expected, these films did not separate the xylene isomers. Only one out of four membranes prepared by this method separated *p*-xylene from *o*-xylene with a small separation factor of 1.7.

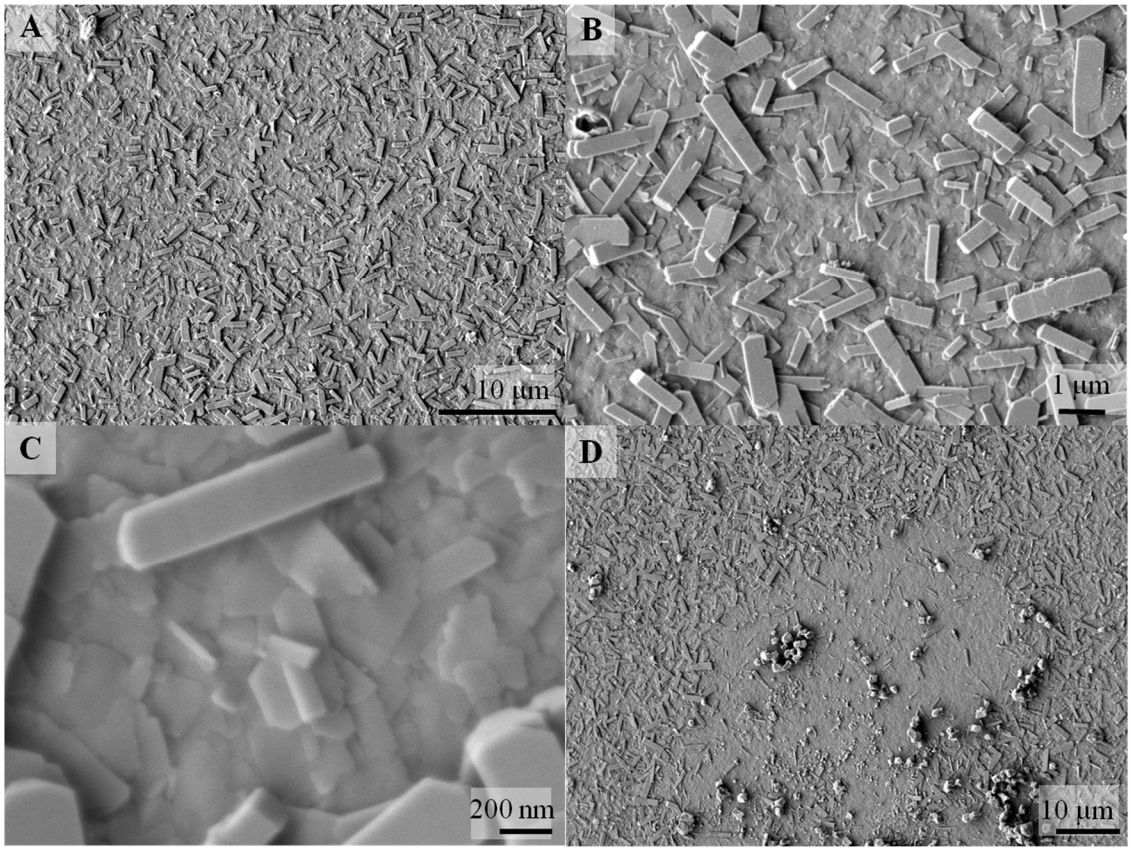

Fig 5.12. SEM images of TPAOH impregnated growth of the *b*-oriented MFI nanosheet seed layer at 190 ºC for 24 hours.

In order to improve the separation performance of the MFI nanosheet film, the growth time was increased from 24 hours to 48 hours since an increase in the crystal inter-growth would serve to reduce the interparticle gaps. Fig. 5.13 shows the morphology (A, B and C) and the cross section (D) of the MFI nanosheet film grown for 48 hours. There were a few large particles (~10-20 μm in size) on the surface of the film as indicated by the lighter spots in this image (Fig. 5.13 A). The origin of these particles is not clear. Their morphology did not resemble conventional MFI crystals. However, surrounding these particles, the crystal growth appeared to be uniform (Fig. 5.13 B). As desired, the MFI film was *b*-oriented. In between large MFI-crystals, intergrown MFI nanosheets could be observed (Fig. 5.13C). This indicated that the secondary grown MFI film is not very thick. Fig. 5.13D shows a SEM image of the cross-section of the secondary grown film. The cross-section was prepared by the FIB technique. Protective gold and platinum coatings were deposited on the top of the MFI film to protect MFI film from the beam damage during the FIB processing. As shown in Fig. 5.13D, the film thickness varied, mainly due to the presence of large MFI crystals in the vicinity of intergrown MFI nanosheets. The film was ca. 325 nm thick around intergrown MFI nanosheets. The molecular sieving characteristics of this film was characterized using an equimolar feed of *p*-xylene and *o*-xylene (close to 0.5 KPa each). This MFI film separated *p*-xylene from *o*-xylene with a separation factor of 500 and with a *p*-xylene permeance of 3 $x10^{-7}$ moles/m^2-Pa-s when operated at 150 ºC. The permeance and the separation factor of this membrane did not change during the period of 60 days of permeance testing. Five membranes prepared by this synthesis route led to *p*-xylene/*o*-xylene separation factors between 20 and 500, while the *p*-xylene permeance was close to 3 $x10^{-7}$ moles/m^2-Pa-s. This variability in the separation factor of these membranes can be due to the variation in the surface coverage of the nanosheets. As shown in Fig. 5.12D, nanosheet coatings by vacuum filtration do not take place on the over-sintered area of the silica support. These uncoated area of the silica support act as defect zones.

Fig. 5.14 shows the surface morphology and the cross sectional SEM images of a thin, *b*-oriented MFI membrane grown by the impregnation growth method. In the case of

this membrane, impregnating of the OSDA solution in the nanosheet seed layer was carried out for 120 seconds. This was followed by the hydrothermal treatment at 190 ºC for 48 hours. The growth of MFI nanosheet crystals in this case seemed to be lesser as compared to that in the previous experiment with an impregnation time of 40 seconds (Fig. 5.13). As desired, an in-plane growth of MFI nanosheet took place. The cross-section image in 5.14B indicates the thickness of this MFI film between 100 and 150 nm. This is the thinnest zeolite membrane ever reported. This film separated *p*-xylene from *o*-xylene with separation factor of 20 and with a *p*-xylene permeance of 3 x 10^{-7} moles/m^2-Pa-s when operated at 150 ºC.

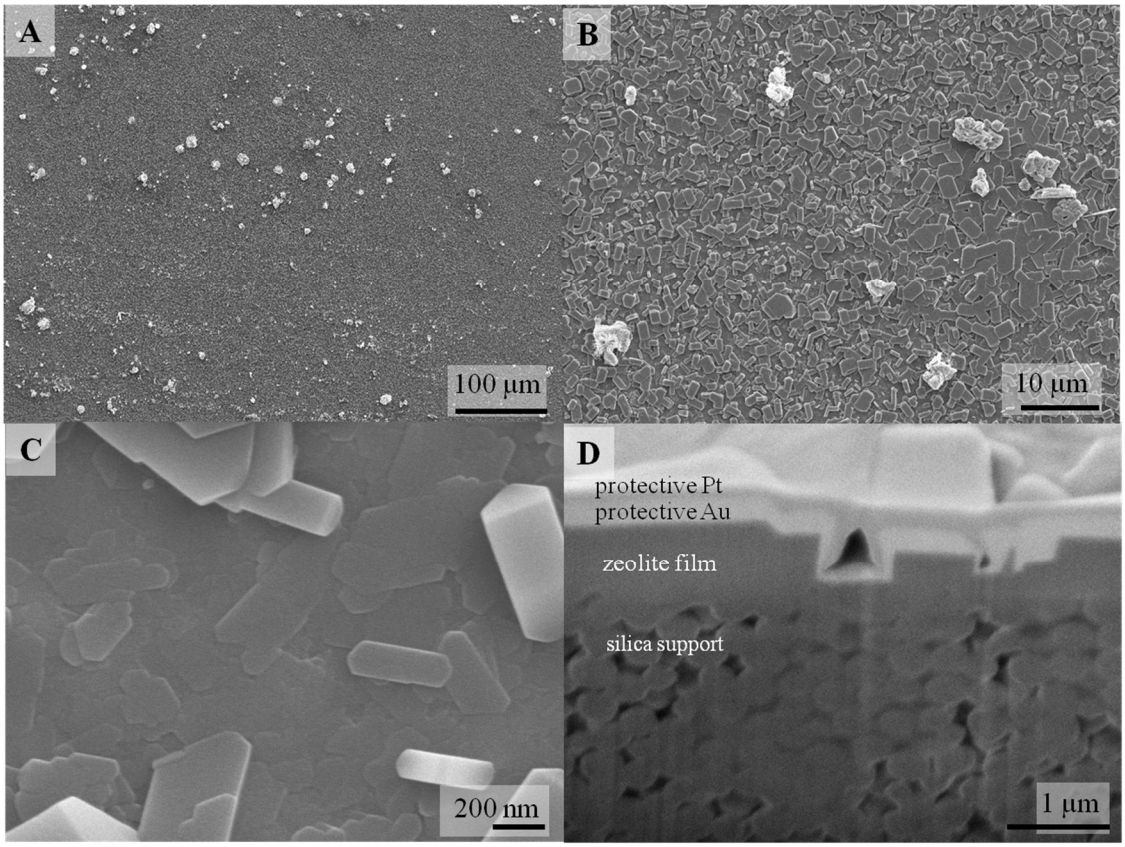

Fig 5.13. SEM images of an MFI film grown using the impregnation technique. The impregnation was done by soaking the seed layer in 0.025M TPAOH for 40 seconds. The hydrothermal treatment was carried out at 190 ºC for 48 hours. The cross section of the film is shown in (D).

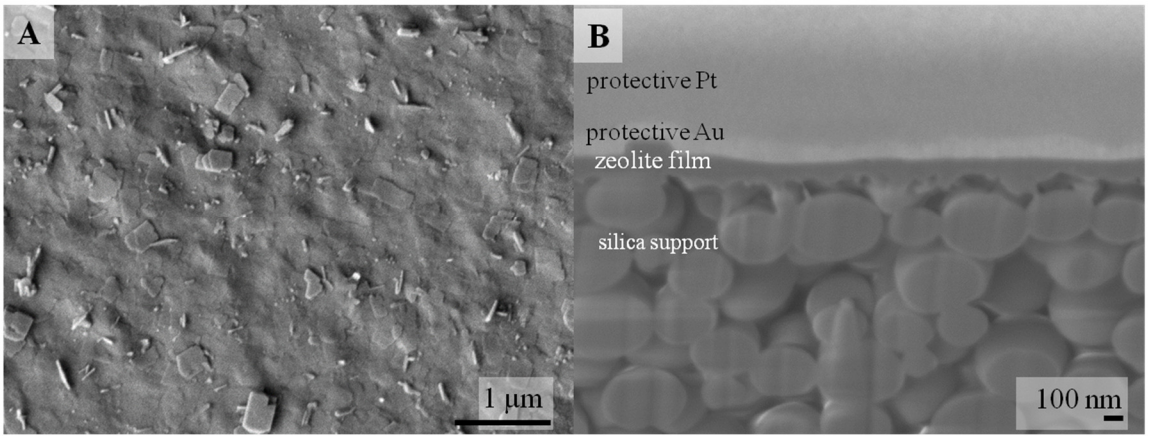

Fig 5.14. A: SEM image of an MFI film grown by the impregnation technique. The impregnation was done by soaking the seed layer in 0.025M TPAOH for 120 seconds. The hydrothermal treatment was carried out at 190 ºC for 48 hours. The cross section of the film is shown in (B).

Ultrathin MFI nanosheet seed layers (3-10 nm in thickness, Fig. 5.7F) were also subjected to the in-plane growth by the impregnation technique. The MFI seed layer was impregnated with 0.025M TPAOH solution followed by the hydrothermal treatment at 190 ºC for 48 hours. A uniform and complete crystal inter-growth was observed (Fig. 5.15A and B). However, the film did not separate xylene isomers. This could be due to presence of a few cracks on the surface of this MFI membrane (image with cracks not shown). More experiments are needed to investigate the formation of cracks in the MFI films prepared by this method.

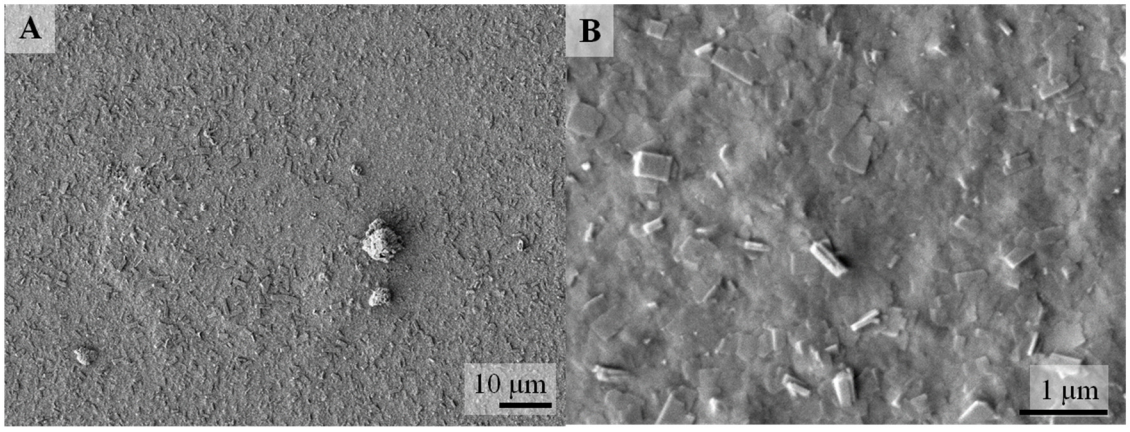

Fig 5.15. SEM images of an ultrathin MFI seed layer grown at 190 ºC for 48 hours. The SEM images of the seed layer for this film is shown in Fig 5.7F.

In-plane growth was also attempted using the impregnation of tetrapropyl ammonium bromide (TPABr) and potassium hydroxide (KOH). TPABr is a less expensive chemical compared to TPAOH as TPAOH is synthesized by the ion-exchange of the bromide salt. The use of TPABr is an environmentally friendly approach because lesser number of chemicals are used in the production of TPABr. KOH acts as a mineralizing agent during the secondary growth of the MFI film. The impregnation solution was prepared by mixing equal volumes of 0.025 M TPABr and 0.025 M KOH. The impregnated MFI nanosheet film was hydrothermally treated at 190 ºC for 36 hours. Upon calcination, this film was characterized for its molecular sieving ability. At 150 ºC, this film separated *p*-xylene from *o*-xylene with separation factor of 833 and with a *p*-xylene permeance of 2 x 10^{-7} moles/m^2-Pa-s. The separation performance of the film remained consistent for a continuous period of 60 days, after which the film was taken out for the surface characterization by the SEM. Fig. 5.16 shows the SEM images of the top surface of this MFI membrane. This membrane (Fig 5.16A and B) had domains of the in-plane growth (5.16C) and the random columnar growth (5.16 C) of MFI crystals. The domains of random growth are expected to offer a much higher resistance to the diffusion of xylenes. This explains the lower permeance of this membrane as compared to other membranes prepared by the impregnation growth. The formation of the randomly oriented MFI domains can be attributed to the underlying support microstructure. Fig. 5.17A shows a silica support surface without the 50 nm silica nanoparticle layer. The support surface also consisted of several domains (lighter area), which are essentially created by the close packing of the silica spheres. During the preparation of silica support, some of the silica spheres occasionally form 3-dimensionally ordered macroporous (3DOM)[129] structures. These 3DOM structure (lighter area in Fig. 5.17A) sinter much more than the loosely packed silica spheres (grey area in Fig. 5.17A). A coating of 50 nm silica nanoparticles followed by the heat treatment at 500 ºC leads to partial pore closure around the closely packed 3DOM structure (Fig. 5.17B). As discussed before, the filter coating method aimed to prepare a thin film of MFI-nanosheets, fails to deposit MFI nanosheets on these over-sintered area (Fig. 5.17C). Therefore, instead of secondary growth of nanosheet crystals,

primary growth of the silica nanoparticles takes place. The primary growth of silica nanoparticles leads to randomly oriented MFI crystals (Fig. 5.17D).

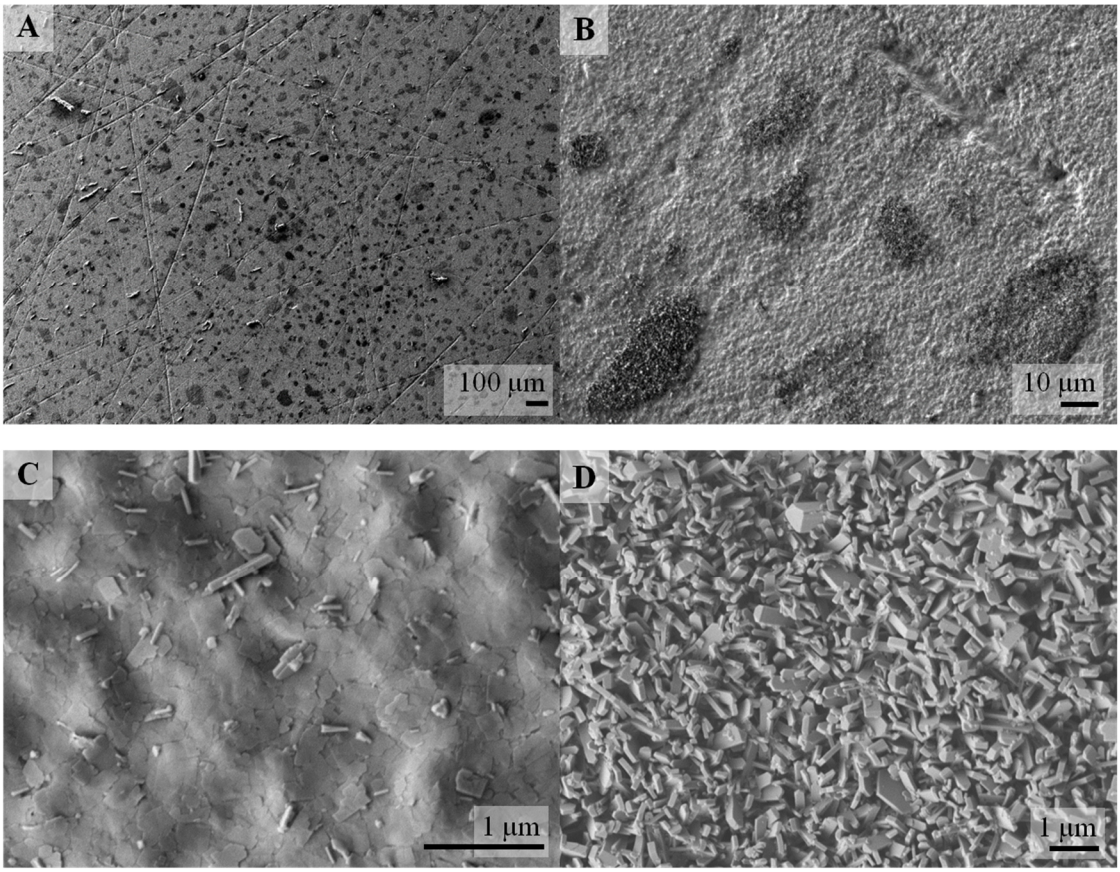

Fig 5.16. A, B: Growth of MFI nanosheet film using the impregnation of TPABr and KOH. The grey patch is the randomly oriented MFI film (D), and the lighter area is the *b*-oriented MFI film (C).

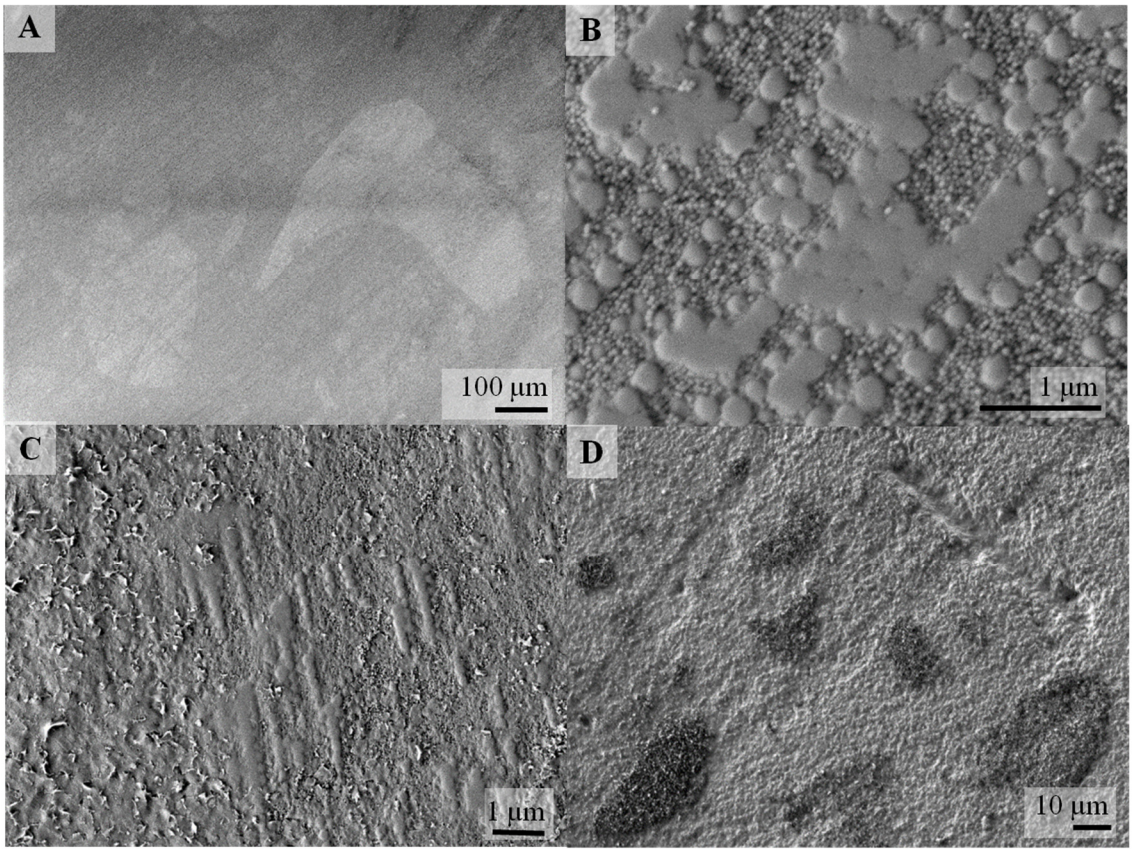

Fig 5.17. A: SEM image of the silica support surface without the 50 nm nanoparticle layer. The lighter patches on the surface are 3DOM silica domains. B: Over-sintering and partial pore blockage of the silica support after the deposition and the sintering of the 50 nm silica nanoparticle layer. C: MFI-nanosheet seed layer showing a poor coating of nanosheets on an over-sintered silica domain. D. An MFI membrane fabricated by the impregnated growth showing non-uniform surface. The darker patches are the randomly oriented MFI crystals.

5.4 Summary

The fabrication of sub-100 nm thick MFI nanosheets films of was demonstrated by depositing MFI nanosheets on an asymmetric silica support. Two secondary growth techniques (1) use of a flouride containing gel, and (2) the impregnation of the MFI seed layer by a dilute OSDA solution, were investigated for the fabrication of a *b*-oriented MFI membrane. Needle like growth of the nanosheets were observed in most of the growth experiments using the fluoride gel. Permselective membranes were achieved using the fluoride containing gel, however, MFI crystals on the surface of the membranes were randomly oriented. On the other hand, the impregnation growth method led to the *b*-

oriented permselective MFI membranes. These membrane were stable for entire duration of testing (60 days) as there was no noticeable change in the separation performance of the membrane. The highest *p*-xylene permeance recorded by these membranes was 4 x 10^{-7} mole/m^2-s-Pa, which makes the *b*-oriented MFI nanosheet membranes highly attractive for the industrial deployment.

Chapter 6: Conclusions

Zeolite membrane-based technologies offer an energy-efficient alternative to the conventional separation methods such as distillation, crystallization or pressure swing adsorption. Despite the significant advances made in the synthesis of zeolite membranes in the last two decades, their application has been limited to small- to medium-scale industries. The synthesis of high throughput membranes can pave the way for the large scale deployment of these zeolite membranes. The most popular strategy employed to construct such membranes involves both (a) the use of a high throughput support, and (b) the fabrication of thin, oriented zeolite films. The research direction presented in this dissertation surveyed both of these strategies.

The first strategy of constructing a high-throughput support was implemented by coating the zeolite platelets on a commercial high throughput PSS supports. These commercial PSS tubes had a very high surface roughness, with the pore opening ranging from 10-20 μm in size. Hydrothermally synthesized ITQ-1 particles were segregated by sonication. The segregated ITQ-1 platelets were coated on the PSS tubes using the dip coating technique. The key challenge encountered in the coating of the PSS tube with the zeolite platelets was the mismatch of the thermal expansion coefficient between the PSS tube and ITQ-1 platelets, which often resulted in the cracking or delamination of the thick, defect free ITQ-1 films. To overcome this challenge, the coating method was optimized to generate a thin film of the zeolite platelets. However, these thin coatings had many pinhole defects on the surface of the PSS tubes. Effect of the dip coating speed and the viscosity of the coating suspension (by addition of polymeric binder) on the microstructure and the thickness of the ITQ-1 film was studied. Gas permeation studies conducted on the crack-free ITQ-1 films indicated Knudsen transport as these films separated H_2 from CO_2 with an ideal selectivity of 4.

The second strategy of fabricating a thin oriented zeolite membrane was addressed by synthesizing highly crystalline, morphologically intact zeolite nanosheets. Although the exfoliation or delamination of the layered zeolites to obtain the zeolite nanosheets was

previously described in literature[7, 44], a method to prepare a coating suspension of segregated, highly crystalline and intact nanosheets was not reported. This was the biggest bottleneck in the fabrication of the sub-100 nm thick zeolite films. This issue was addressed by exfoliation of the layered zeolite by a polymer melt compounding followed by the solution processing of the polymer-zeolite nanocomposite to purify the nanosheets from the polymer matrix. One of the biggest advantages of using a solution processing method for the purification of the nanosheets was that the nanosheet morphology was well-preserved during the process without any perceivable damages such as curling or aggregation. It also allowed for the removal of large un-exfoliated particles by the centrifugation of the coating suspension. The nanosheets in the suspension were characterized extensively using TEM, HRTEM, ED, ^{29}Si MAS NMR, powder XRD, AFM and nitrogen adsorption methods. The characterization revealed that MFI-nanosheets prepared by solution processing were highly crystalline. No observable damage to the nanosheet morphology was detected. AFM and NMR confirmed the thickness of MFI-nanosheets to be 3.2 nm, corresponding to a 1.5 unit cell thickness along the *b*-axis of MFI.

For the first time, a suspension of segregated, highly crystalline, and high-aspect-ratio zeolite nanosheets was obtained. The next stride towards the realization of these nanosheets as a membrane for gas separation was the coating of the nanosheet suspension on porous supports. This was achieved by using the filter coating process. This process proved to be simple and scalable, as the nanosheets could be directly coated on the rough symmetric supports without the need for pore masking, surface functionalization, or multiple coating steps. The filter coating process is especially attractive for scale-up as it can be applied to a wide range of surfaces such as flat disks, tubes, hollow fibers etc. It also allows for a simple control of the zeolite film thickness by simply varying the amount of the coating suspension for the filter coating.

In order to fabricate sub-100 nm thick coatings, zeolite nanosheet suspension was purified by DGC in a non-linear stack of organic solvents. This novel technique allowed for the complete removal of the polymer and the un-exfoliated particles in just a few steps. This was confirmed by the TGA and the TEM studies. In addition, the yield of the purified

exfoliated nanosheets obtained from the melt compounded polymer-zeolite nanocomposite, was doubled. An unprecedented, 80-nm thick zeolite film was obtained by filter coating of this suspension on a smooth alumina support.

Ultrathin films (10-100 nm thick) of the zeolite nanosheets were prepared on an asymmetric silica support by filter coating. These films were then grown in a fluoride containing gel to fabricate perm-selective MFI membranes. However, these membranes were randomly oriented. A further study of the growth behavior of the MFI nanosheets in the fluoride containing gel revealed needle-like growth of the nanosheets. In order to overcome the problem of random orientation, an impregnation growth technique was used on the zeolite nanosheet films deposited on silica supports. Approximately 100 nm thick, *b*-oriented MFI membranes were obtained by this impregnation growth method. This membrane, along with the other membranes grown by the impregnation method, was stable for many days and no change in the membrane performance was observed in this period. The highest *p*-xylene permeance recorded by these membranes was 4×10^{-7} mole/m2-s-Pa, which makes these zeolite membranes highly attractive for industrial deployment.

Chapter 7: Future Directions

The availability of highly crystalline, high-aspect ratio zeolite nanosheets has opened many opportunities in the field of zeolites and zeolite thin films.[82] The exfoliation and the solution processing processes that are applied to zeolite nanosheets are quite generic, and can be extended to any other layered material such as graphene, clays, layered metal oxides, etc. Furthermore, these exfoliated sheets could be incorporated in a polymer matrix for the fabrication of the polymer-zeolite mixed matrix membranes (MMM).[130, 131] MMMs combine the salient features of both zeolite and polymeric membranes. The fabrication process of MMM is expected to be as simple as that of the polymer membranes. Additionally, MMM are expected to exhibit a better separation performance than that of their polymeric counterpart, owing to the incorporation of rigid zeolitic pore channels in the polymer matrix.[132]

In this dissertation, the preparation of the segregated dispersions of MWW and MFI nanosheet suspension was demonstrated. These suspensions can be used to make a hybrid zeolite film containing alternating layers of MWW and MFI nanosheets. These films will have interesting molecular sieving properties that can be used for novel applications. These films could also be used as a seed layer for the preparation of an MWW membrane for the gas separation applications. In-plane secondary growth of MWW is still challenging, and hence, MFI can act as a matrix between the MWW layers. In a similar concept, MWW nanosheets can be coated on top of the MFI nanosheet seed layer to reduce the out-of-plane growth of the MFI seed layer.[133] Without the coating of MWW film, the secondary growth of the MFI nanosheet film in C6 solution led to a film that did not separate the xylene isomers. This can be attributed to the development of surface cracks during the calcination of the secondary grown MFI film (Fig. 7.1A). Interestingly, secondary growth of MWW nanosheet coated MFI nanosheet film did not develop crack during the step (Fig. 7.1B). Also, the density of the out-of-plane *a*-oriented MFI crystal was noticeably less in this case. This can be attributed to the reduced heterogeneous nucleation of MFI on the surface of MWW nanosheets. MFI membranes prepared in this way separated *p*-xylene from *o*-xylene

with a separation factor of 84. Further studies on the heterogeneous nucleation and growth of MFI on MWW, and vice versa, is needed to understand and control the microstructure of these membranes.

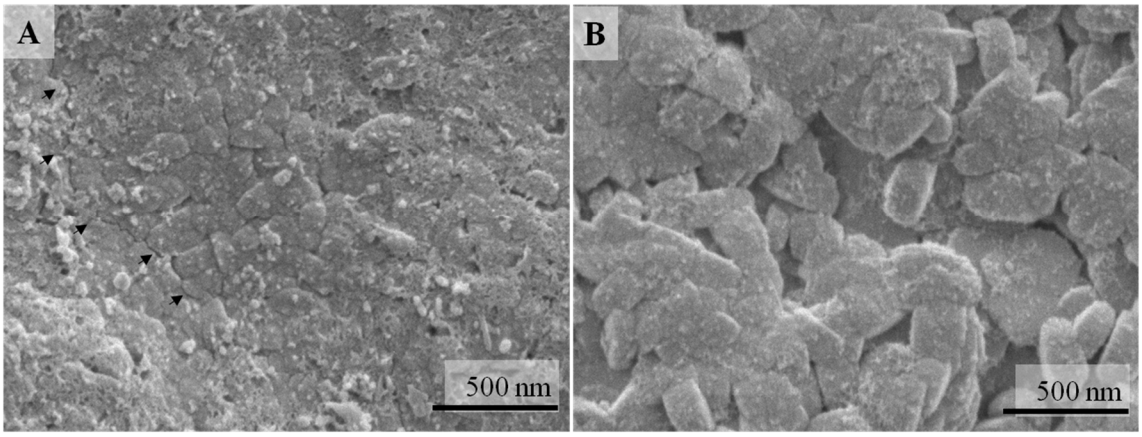

Fig 7.1. A: An MFI membrane prepared by the secondary growth of MFI-film in the C6 solution at 90 ºC for 20 hours. Cracks in the film are highlighted by black arrows. B: An MFI membrane prepared by the secondary growth of MWW nanosheet coated MFI film in the C6 solution at 90 ºC for 20 hours.

Purification of zeolite nanosheets by the DGC method is an attractive process for the complete removal of polymer and large unwanted particles in a few simple steps. In this dissertation, large unexfoliated particles were successfully removed using the rate zonal (non-equilibrium) centrifugation in a nonlinear (step) density gradient of organic solvents. This is an attractive process, since the desired separation can be achieved in 30 minutes. However, this method restricts the yield of exfoliated nanosheets because of its reliance on the relative sedimentation rate of exfoliated and unexfoliated zeolite nanosheets. A possible way to improve the yield and the purity of exfoliated zeolite nanosheets is the use of equilibrium DGC (isopycnic centrifugation). In this case, the density difference between exfoliated and unexfoliated MFI nanosheets can be exploited to obtain improved separation. Unexfoliated MFI nanosheets contain 20% OSDA incorporated in their pores and 21% extra-framework OSDA incorporated in their gallery spacing.[8, 127] In contrast, exfoliated MFI nanosheets contain only 26-28% OSDA.[127] This difference in the OSDA content creates a density difference between exfoliated and unexfoliated nanosheets. This density difference can be exploited using the equilibrium

DGC, since exfoliated nanosheets and unexfoliated nanosheets will settle to different density zones in the centrifuge tube.[99] One such DGC can be carried out using density gradients created by aqueous solutions of sodium metatungstate. Fig. 7.2 shows a plot of the density of sodium metatungstate aqueous solution as a function of the mass fraction of sodium metatungstate[134, 135]. The density of this solution can be easily adjusted up to 2.2 g/cc. The density of exfoliated and unexfoliated nanosheets are expected to fall between 1.6 g/cc and 2.2 g/cc, thus making sodium metatungstate solution an attractive option for the high yield separation of zeolite nanosheets.

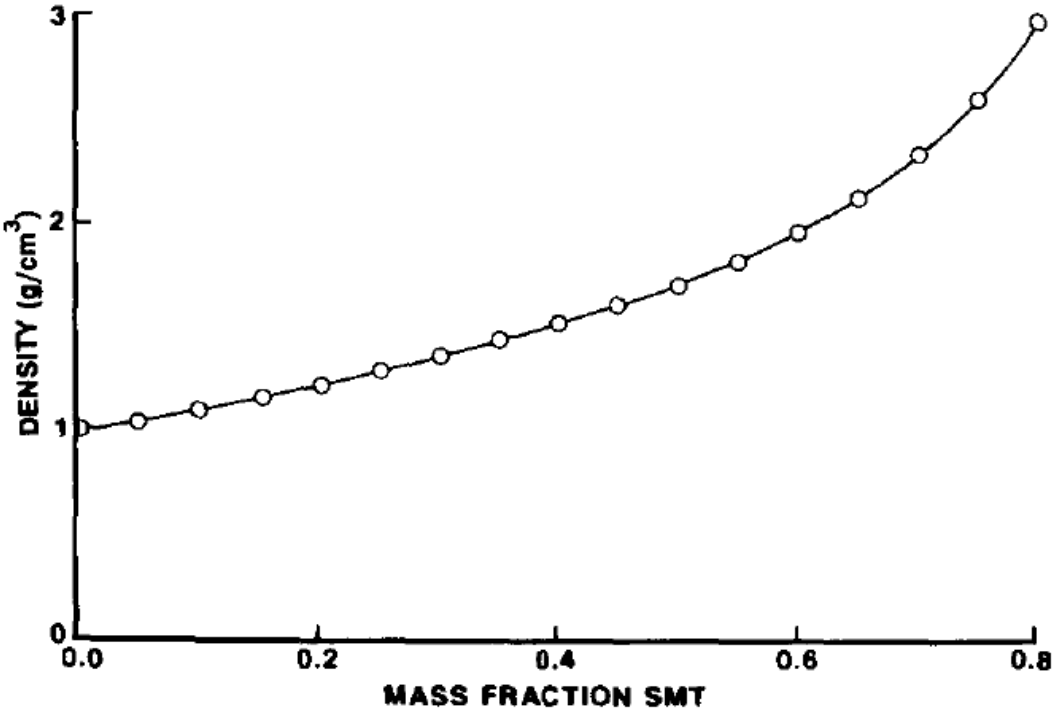

Fig 7.2: Density of the aqueous solutions of sodium metatungstate as a function of its mass fraction in the solution. The image is adapted from Hoover et al.[134]

The DGC purified MFI-nanosheets were successfully stabilized in n-octanol. A compact, oriented film of MFI-nanosheets was made on various porous supports by filter coating. However, the fabrication of a continuous MFI nanosheet film on a non-porous support using the MFI nanosheet suspension in n-octanol is challenging due to the high boiling point of n-octanol. A suspension of the zeolite nanosheets in either water or ethanol is highly desired for this purpose. Since MFI-nanosheets have OSDA embedded in their

pore channels, it is difficult to prepare their suspension in water. However, upon the removal of extra-framework OSDA, it is conceivable to disperse MFI-nanosheets in ethanol. One common technique to remove surfactants from the gallery spacing of layered zeolites is acid treatment. Recently, Corma et al. reported a two-step acid treatment method to remove cetyltrimethylammonium hydroxide (CTMA) from the gallery spacing of swollen MWW.[136] During the acid treatment, the H^+ ions from the acid replace the quaternary ammonium ions from the layer gallery. This acid treatment process was carried out on the DGC purified MWW and MFI nanosheets. After the acid treatment, both MWW and MFI nanosheets were successfully dispersed in ethanol (Fig. 7.3 and 7.4). This is an important progress because zeolite nanosheets suspended in ethanol can then be fabricated into a compact film on a non-porous support by methods such as evaporation induced self-assembly (EISA)[137], Langmuir Blodgett deposition[138], convective assembly[54, 139] etc. TEM images (Fig. 7.3A and B) of MFI-nanosheets suspended in ethanol indicate a good dispersion of MFI nanosheets in ethanol as most of MFI nanosheets do not touch each other. A strong ED pattern (Fig. 7.3C) of the acid-treated MFI nanosheet indicates the absence of any structural damage to MFI nanosheets. This ED pattern is comparable to that of MFI nanosheets before the acid treatment, indicating that the structure of MFI nanosheets is preserved during the acid treatment process (Fig 4.5B).

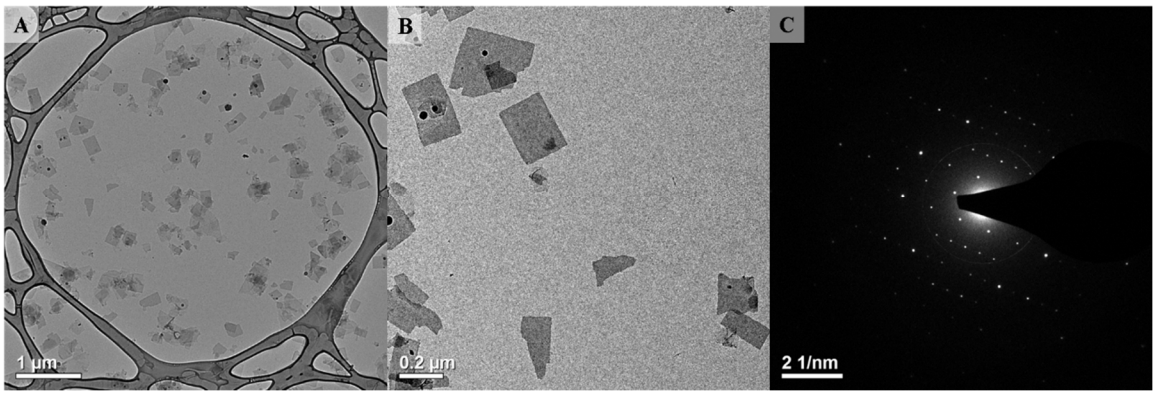

Fig 7.3. A, B: TEM images of acid treated MFI nanosheets dispersed in ethanol. C: ED pattern of one of the MFI nanosheets.

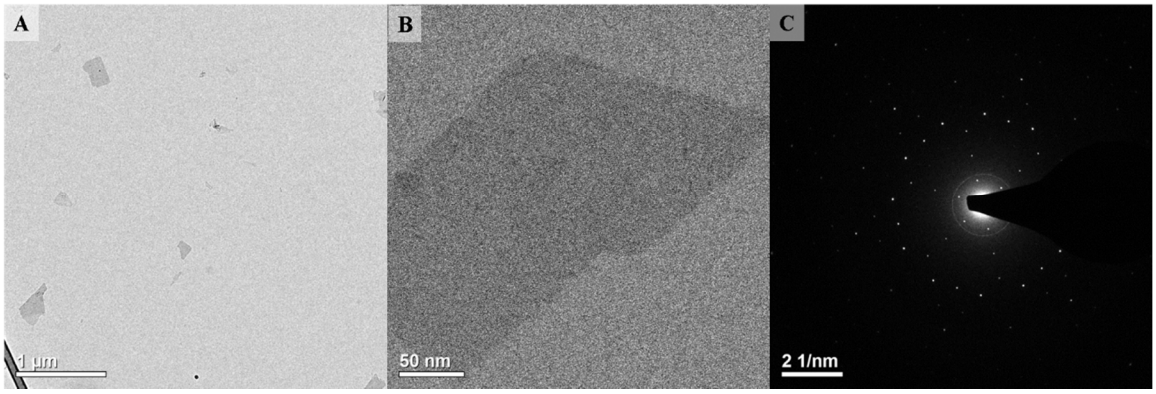

Fig 7.4. A: Low magnification TEM images of acid treated MWW nanosheets suspended in ethanol. B: High magnification TEM image of c-oriented MWW nanosheet. C: ED of nanosheet in (B).

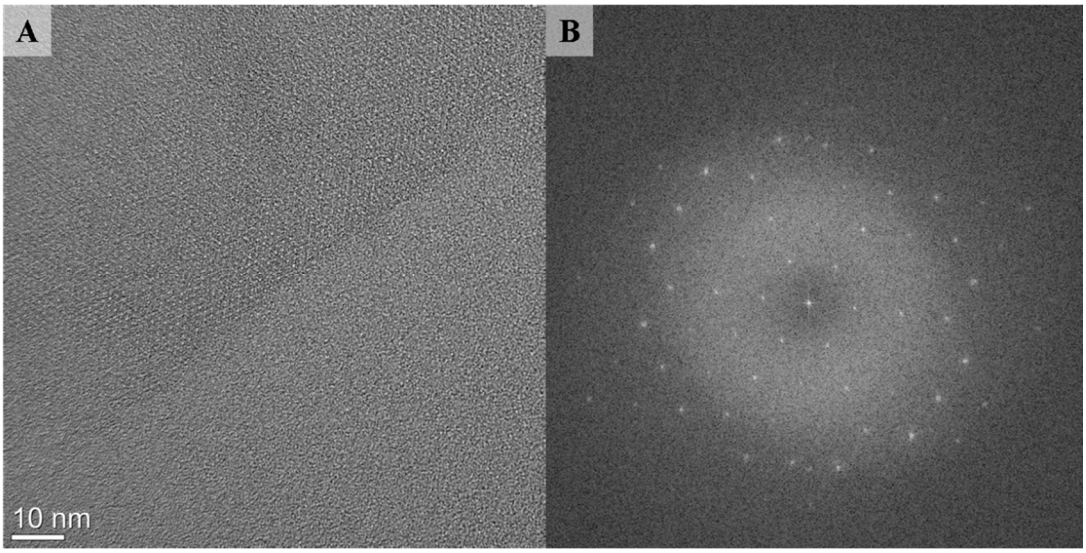

Fig 7.5. A: HRTEM image of acid treated MWW. B: FFT of the image in (A).

Fig. 7.4A and B show low and high magnification TEM images of the acid treated MWW nanosheets dispersed in ethanol. MWW nanosheets oriented themselves perpendicular to their *c*-axis on the flat TEM grid. The ED pattern of MWW nanosheets shown in Fig. 7.4B is presented in Fig. 7.4C. The ED pattern confirms that MWW nanosheets were *c*-oriented. The contrast of the ED pattern is much higher than that of the ED pattern of MWW nanosheets before the DGC purification and the acid treatment (Fig. 3.3E). This can be attributed to the absence of polymer in the acid treated MWW nanosheets. Fig. 7.5A shows an HRTEM image of the acid treated MWW nanosheets. The

pore channels of MWW nanosheets along the *c*-axis (Fig. 2.1A and B) are visible as bright spots in the image. No signs of structural damages can be observed from these images. The structure preservation is also confirmed by a fast Fourier transform (FFT) of the MWW nanosheet image (Fig. 7.5B). Further work should explore an oriented coating of these nanosheets on various non-porous supports.

Bibliography

1. Cundy, C. S.; Cox, P. A., The hydrothermal synthesis of zeolites: history and development from the earliest days to the present time. *Chemical Reviews* 2003, 103, 663-702.

2. Davis, M. E., Ordered porous materials for emerging applications. *Nature* 2002, 417, 813-821.

3. Barrer, R., Syntheses and reactions of mordenite. *Journal of the Chemical Society (Resumed)* 1948, 2158-2163.

4. Masters, A. F.; Maschmeyer, T., Zeolites - From curiosity to cornerstone. *Microporous and Mesoporous Materials* 2011, 142, 423-438.

5. Díaz, I.; Kokkoli, E.; Terasaki, O.; Tsapatsis, M., Surface structure of zeolite (MFI) crystals. *Chemistry of materials* 2004, 16, 5226-5232.

6. Leonowicz, M. E.; Lawton, J. A.; Lawton, S. L.; Rubin, M. K., MCM-22 - a molecular-sieve with 2 independent multidimension channel systems. *Science* 1994, 264, 1910-1913.

7. Corma, A.; Fornes, V.; Pergher, S. B.; Maesen, T. L. M.; Buglass, J. G., Delaminated zeolite precursors as selective acidic catalysts. *Nature* 1998, 396, 353-356.

8. Choi, M.; Na, K.; Kim, J.; Sakamoto, Y.; Terasaki, O.; Ryoo, R., Stable single-unit-cell nanosheets of zeolite MFI as active and long-lived catalysts. *Nature* 2009, 461, 246-U120.

9. Corma, A., From microporous to mesoporous molecular sieve materials and their use in catalysis. *Chemical reviews* 1997, 97, 2373-2420.

10. McLeary, E. E.; Jansen, J. C.; Kapteijn, F., Zeolite based films, membranes and membrane reactors: Progress and prospects. *Microporous and Mesoporous Materials* 2006, 90, 198-220.

11. Tosheva, L.; Valtchev, V. P., Nanozeolites: Synthesis, crystallization mechanism, and applications. *Chemistry of Materials* 2005, 17, 2494-2513.

12. Lew, C. M.; Cai, R.; Yan, Y. S., Zeolite Thin Films: From Computer Chips to Space Stations. *Accounts of Chemical Research* 2010, 43, 210-219.

13. Lai, Z. P.; Bonilla, G.; Diaz, I.; Nery, J. G.; Sujaoti, K.; Amat, M. A.; Kokkoli, E.; Terasaki, O.; Thompson, R. W.; Tsapatsis, M.; Vlachos, D. G., Microstructural

optimization of a zeolite membrane for organic vapor separation. *Science* 2003, 300, 456-460.

14. Choi, J.; Jeong, H. K.; Snyder, M. A.; Stoeger, J. A.; Masel, R. I.; Tsapatsis, M., Grain Boundary Defect Elimination in a Zeolite Membrane by Rapid Thermal Processing. *Science* 2009, 325, 590-593.

15. Pham, T. C. T.; Kim, H. S.; Yoon, K. B., Growth of Uniformly Oriented Silica MFI and BEA Zeolite Films on Substrates. *Science* 2011, 334, 1533-1538.

16. Bosko, M. L.; Ojeda, F.; Lombardo, E. A.; Cornaglia, L. M., NaA zeolite as an effective diffusion barrier in composite Pd/PSS membranes. *Journal of Membrane Science* 2009, 331, 57-65.

17. Choi, J. Y.; Lai, Z. P.; Ghosh, S.; Beving, D. E.; Yan, Y. S.; Tsapatsis, M., Layer-by-layer deposition of barrier and permselective c-Oriented-MCM-22/silica composite films. *Industrial & Engineering Chemistry Research* 2007, 46, 7096-7106.

18. Wang, Z. B.; Wang, H. T.; Mitra, A.; Huang, L. M.; Yan, Y. S., Pure-silica zeolite low-k dielectric thin films. *Advanced Materials* 2001, 13, 746-749.

19. Pham, T. C. T.; Kim, H. S.; Yoon, K. B., Large Increase in the Second-Order Nonlinear Optical Activity of a Hemicyanine-Incorporating Zeolite Film. *Angewandte Chemie-International Edition* 2013, 52, 5539-5543.

20. Ockwig, N. W.; Nenoff, T. M., Membranes for Hydrogen Separation. *Chemical Reviews (Washington, DC, United States)* 2007, 107, 4078-4110.

21. Lin, Y. S.; Kumakiri, I.; Nair, B. N.; Alsyouri, H., Microporous inorganic membranes. *Separation and Purification Methods* 2002, 31, 229-379.

22. Choi, J.; Tsapatsis, M., MCM-22/Silica Selective Flake Nanocomposite Membranes for Hydrogen Separations. *Journal of the American Chemical Society* 2010, 132, 448-449.

23. Coronas, J.; Falconer, J. L.; Noble, R. D., Characterization and permeation properties of ZSM-5 tubular membranes. *Aiche Journal* 1997, 43, 1797-1812.

24. Xomeritakis, G.; Nair, S.; Tsapatsis, M., Transport properties of alumina-supported MFI membranes made by secondary (seeded) growth. *Microporous and Mesoporous Materials* 2000, 38, 61-73.

25. Yan, Y. S.; Davis, M. E.; Gavalas, G. R., Preparation of zeolite ZSM-5 membranes by in-situ crystallization on porous alpha-Al2O3. *Industrial & Engineering Chemistry Research* 1995, 34, 1652-1661.

26. Kondo, M.; Komori, M.; Kita, H.; Okamoto, K., Tubular-type pervaporation module with zeolite NaA membrane. *Journal of Membrane Science* 1997, 133, 133-141.

27. Korelskiy, D.; Leppajarvi, T.; Zhou, H.; Grahn, M.; Tanskanen, J.; Hedlund, J., High flux MFI membranes for pervaporation. *Journal of Membrane Science* 2013, 427, 381-389.

28. *2012 World Paraxylene and Terephthalates Analysis*; Chemical Market Associates, Inc., IHS Inc.: 2011.

29. Caro, J.; Noack, M., Zeolite membranes - Recent developments and progress. *Microporous and Mesoporous Materials* 2008, 115, 215-233.

30. Lai, Z. P.; Tsapatsis, M.; Nicolich, J. R., Siliceous ZSM-5 membranes by secondary growth of b-oriented seed layers. *Advanced Functional Materials* 2004, 14, 716-729.

31. Lee, P. S.; Zhang, X. Y.; Stoeger, J. A.; Malek, A.; Fan, W.; Kumar, S.; Yoo, W. C.; Al Hashimi, S.; Penn, R. L.; Stein, A.; Tsapatsis, M., Sub-40 nm zeolite suspensions via disassembly of three-dimensionally ordered mesoporous-imprinted silicalite-1. *Journal of the American Chemical Society* 2011, 133, 493-502.

32. Krishna, R.; Wesselingh, J. A., Review article number 50 - The Maxwell-Stefan approach to mass transfer. *Chemical Engineering Science* 1997, 52, 861-911.

33. Narkhede, V. V.; Gies, H., Crystal Structure of MCM-22 (MWW) and Its Delaminated Zeolite ITQ-2 from High-Resolution Powder X-Ray Diffraction Data: An Analysis Using Rietveld Technique and Atomic Pair Distribution Function. *Chemistry of Materials* 2009, 21, 4339-4346.

34. Lupulescu, A. I.; Kumar, M.; Rimer, J. D., A Facile Strategy To Design Zeolite L Crystals with Tunable Morphology and Surface Architecture. *Journal of the American Chemical Society* 2013, 135, 6608-6617.

35. Lupulescu, A. I.; Rimer, J. D., Tailoring Silicalite-1 Crystal Morphology with Molecular Modifiers. *Angewandte Chemie-International Edition* 2012, 51, 3345-3349.

36. Chen, H. Y.; Wydra, J.; Zhang, X. Y.; Lee, P. S.; Wang, Z. P.; Fan, W.; Tsapatsis, M., Hydrothermal Synthesis of Zeolites with Three-Dimensionally Ordered Mesoporous-Imprinted Structure. *Journal of the American Chemical Society* 2011, 133, 12390-12393.

37. Na, K.; Choi, M.; Park, W.; Sakamoto, Y.; Terasaki, O.; Ryoo, R., Pillared MFI zeolite nanosheets of a single-unit-cell thickness. *Journal of the American Chemical Society* 2010, 132, 4169-4177.

38. Corma, A.; Fornes, V.; Martinez-Triguero, J.; Pergher, S. B., Delaminated Zeolites: Combining the Benefits of Zeolites and Mesoporous Materials for Catalytic Uses. *Journal of Catalysis* 1999, 186, 57-63.

39. Corma, A.; Fornes, V.; Guil, J. M.; Pergher, S.; Maesen, T. L. M.; Buglass, J. G., Preparation, characterization and catalytic activity of ITQ-2, a delaminated zeolite. *Microporous and Mesoporous Materials* 2000, 38, 301-309.

40. Corma, A., Catalysts made thinner. *Nature* 2009, 461, 182-183.

41. Sheffel, J. A.; Tsapatsis, M., A model for the performance of microporous mixed matrix membranes with oriented selective flakes. *Section Title: Unit Operations and Processes* 2007, 295, 50-70.

42. Choi, S.; Coronas, J.; Lai, Z.; Yust, D.; Onorato, F.; Tsapatsis, M., Fabrication and gas separation properties of polybenzimidazole (PBI)/nano porous silicates hybrid membranes. *Journal of Membrane Science* 2008, 316, 145-152.

43. Choi, S.; Coronas, J.; Jordan, E.; Oh, W.; Nair, S.; Onorato, F.; Shantz, D. F.; Tsapatsis, M., Layered silicates by swelling of AMH-3 and nanocomposite membranes. *Angewandte Chemie International Edition* 2008, 47, 552-555.

44. Maheshwari, S.; Jordan, E.; Kumar, S.; Bates, F. S.; Penn, R. L.; Shantz, D. F.; Tsapatsis, M., Layer structure preservation during swelling, pillaring, and exfoliation of a zeolite precursor. *Journal of the Americal Chemical Society* 2008, 130, 1507-1516.

45. Maheshwari, S. Exfoliated zeolite sheets and block copolymers as building blocks for composite membranes, Thesis, University of Minnesota 2009.

46. Guo, H. L.; Zhu, G. S.; Li, H.; Zou, X. Q.; Yin, X. J.; Yang, W. S.; Qiu, S. L.; Xu, R., Hierarchical growth of large-scale ordered zeolite silicalite-1 membranes with high permeability and selectivity for recycling CO2. *Angewandte Chemie-International Edition* 2006, 45, 7053-7056.

47. Huang, Y.; Dittmeyer, R., Preparation of thin palladium membranes on a porous support with rough surface. *Journal of Membrane Science* 2007, 302, 160-170.

48. Sato, K.; Sugimoto, K.; Nakane, T., Preparation of higher flux NaA zeolite membrane on asymmetric porous support and permeation behavior at higher temperatures up to 145 degrees C in vapor permeation. *Journal of Membrane Science* 2008, 307, 181-195.

49. Yan, H.; Xue, L.; Yiqun, F.; Nanping, X., Palladium-Based Composite Membranes: Principle, Preparation and Characterization. *Progress in Chemistry-Beijing* 2006, 18, 230.

50. Camblor, M. A.; Corma, A.; Diaz-Cabanas, M. J.; Baerlocher, C., Synthesis and structural characterization of MWW type zeolite ITQ-1, the pure silica analog of MCM-22 and SSZ-25. *Journal of Physical Chemistry B* 1998, 102, 44-51.

51. Liu, Z.; Fujita, N.; Terasaki, O.; Ohsuna, T.; Hiraga, K.; Camblor, M. A.; Diaz-Cabanas, M. J.; Cheetham, A. K., Incommensurate modulation in the microporous silica SSZ-24. *Chemistry-a European Journal* 2002, 8, 4549-4556.

52. Grosso, D., How to exploit the full potential of the dip-coating process to better control film formation. *Journal of Materials Chemistry* 2011, 21, 17033-17038.

53. Cardinal, C. M.; Jung, Y. D.; Ahn, K. H.; Francis, L. F., Drying Regime Maps for Particulate Coatings. *Aiche Journal* 2010, 56, 2769-2780.

54. Brewer, D. D.; Shibuta, T.; Francis, L.; Kumar, S.; Tsapatsis, M., Coating Process Regimes in Particulate Film Production by Forced-Convection-Assisted Drag-Out. *Langmuir* 2011, 27, 11660-11670.

55. White, D. A.; Tallmadge, J. A., Theory of drag out of liquids on flat plates. *Chemical Engineering Science* 1965, 20, 33-7.

56. Goucher, F.; Ward, H., A problem in viscosity: The thickness of liquid films formed on solid surfaces under dynamic conditions. *Philos. Mag* 1922, 44, 1002-1014.

57. Landau, L.; Levich, B., Dragging of a liquid by a moving plate. *Acta Physiocochim, URSS* 1942, 17, 42.

58. Wilson, S. D. R., Coating flow on to rods and wires. *AIChE Journal* 1988, 34, 1732-5.

59. Quere, D., Fluid coating on a fiber. *Annual Review of Fluid Mechanics* 1999, 31, 347-384.

60. Hedlund, J.; Jareman, F.; Bons, A. J.; Anthonis, M., A masking technique for high quality MFI membranes. *Journal of Membrane Science* 2003, 222, 163-179.

61. Lambert, C. K.; Gonzalez, R. D., Effect of binder addition on the properties of unsupported gamma-Al2O3 membranes. *Materials Letters* 1999, 38, 145-149.

62. De Lange, R.; Keizer, K.; Burggraaf, A., Analysis and theory of gas transport in microporous sol-gel derived ceramic membranes. *Journal of membrane science* 1995, 104, 81-100.

63. Snyder, M. A.; Tsapatsis, M., Hierarchical nanomanufacturing: From shaped zeolite nanoparticles to high-performance separation membranes. *Angewandte Chemie International Edition* 2007, 46, 7560-7573.

64. Takahashi, N.; Hata, H.; Kuroda, K., Exfoliation of Layered Silicates through Immobilization of Imidazolium Groups. *Chemistry of Materials* 2011, 23, 266-273.

65. Yu, J. H.; Xu, R. R., Rich structure chemistry in the aluminophosphate family. *Accounts of Chemical Research* 2003, 36, 481-490.

66. Gao, Q. M.; Li, B. Z.; Chen, J. S.; Li, S. G.; Xu, R. R.; Williams, I.; Zheng, J. Q.; Barber, D., Nonaqueous synthesis and characterization of a new 2-dimensional layered aluminophosphate [Al3P4O16](3-)center dot 3[CH3CH2NH3](+). *Journal of Solid State Chemistry* 1997, 129, 37-44.

67. Yuan, H. M.; Zhu, G. S.; Chen, J. S.; Chen, W.; Yang, G. D.; Xu, R. R., Dual function of racemic isopropanolamine as solvent and as template for the synthesis of a new layered aluminophosphate: $[NH_3CH_2CH(OH)CH_3]_3 \cdot Al_3P_4O_{16}$. *Journal of Solid State Chemistry* 2000, 151, 145-149.

68. Li, Z.; Marler, B.; Gies, H., A new layered silicate with structural motives of silicate zeolites: Synthesis, crystals structure, and properties. *Chemistry of Materials* 2008, 20, 1896-1901.

69. Juttu, G. G.; Lobo, R. F., Characterization and catalytic properties of MCM-56 and MCM-22 zeolites. *Microporous and Mesoporous Materials* 2000, 40, 9-23.

70. Ogino, I.; Nigra, M. M.; Hwang, S. J.; Ha, J. M.; Rea, T.; Zones, S. I.; Katz, A., Delamination of Layered Zeolite Precursors under Mild Conditions: Synthesis of UCB-1 via Fluoride/Chloride Anion-Promoted Exfoliation. *Journal of the American Chemical Society* 2011, 133, 3288-3291.

71. Liu, L.; Ferdov, S.; Coelho, C.; Kong, Y.; Mafra, L.; Li, J. P.; Dong, J. X.; Kolitsch, U.; Ferreira, R. A. S.; Tillmanns, E.; Rocha, J.; Lin, Z., New Crystalline Layered Zinc Phosphate with 10-Membered-Ring Channels Perpendicular to Layers. *Inorganic Chemistry* 2009, 48, 4598-4600.

72. Rubio, C.; Casado, C.; Gorgojo, P.; Etayo, F.; Uriel, S.; Tellez, C.; Coronas, J., Exfoliated Titanosilicate Material UZAR-S1 Obtained from JDF-L1. *European Journal of Inorganic Chemistry* 2010, 2010, 159-163.

73. Roth, W. J.; Kresge, C. T., Intercalation chemistry of NU-6(1), the layered precursor to zeolite NSI, leading to the pillared zeolite MCM-39(Si). *Microporous and Mesoporous Materials* 2011, 144, 158-161.

74. Choi, J.; Ghosh, S.; King, L.; Tsapatsis, M., MFI zeolite membranes from a- and randomly oriented monolayers. *Adsorption* 2006, 12, 339-360.

75. Nagahara, L. A.; Hashimoto, K.; Fujishima, A.; Snowdenlfft, D.; Price, P. B., Mica etch pits as a height calibration source for atomic-force microscopy. *Journal of Vacuum Science & Technology B* 1994, 12, 1694-1697.

76. Wu, P.; Nuntasri, D.; Ruan, J. F.; Liu, Y. M.; He, M. Y.; Fan, W. B.; Terasaki, O.; Tatsumi, T., Delamination of Ti-MWW and high efficiency in epoxidation of alkenes with various molecular sizes. *Journal of Physical Chemistry B* 2004, 108, 19126-19131.

77. Srivastava, S.; Kotov, N. A., Composite Layer-by-Layer (LBL) Assembly with Inorganic Nanoparticles and Nanowires. *Accounts of Chemical Research* 2008, 41, 1831-1841.

78. Osada, M.; Sasaki, T., Exfoliated oxide nanosheets: new solution to nanoelectronics. *Journal of Materials Chemistry* 2009, 19, 2503-2511.

79. *Frontiers in Chemical Engineering:Research Needs and Opportunities*. The National Academies Press: 1988.

80. Tsapatsis, M., Toward high-throughput zeolite membranes. *Science* 2011, 334, 767-768.

81. Jeong, H. K.; Nair, S.; Vogt, T.; Dickinson, L. C.; Tsapatsis, M., A highly crystalline layered silicate with three-dimensionally microporous layers. *Nature Materials* 2003, 2, 53-58.

82. Varoon, K.; Zhang, X.; Elyassi, B.; Brewer, D. D.; Gettel, M.; Kumar, S.; Lee, J. A.; Maheshwari, S.; Mittal, A.; Sung, C.-Y.; Cococcioni, M.; Francis, L. F.; McCormick, A. V.; Mkhoyan, K. A.; Tsapatsis, M., Dispersible exfoliated zeolite Nanosheets and their application as a selective membrane. *Science* 2011, 334, 72-75.

83. Zhang, X. Y.; Liu, D. X.; Xu, D. D.; Asahina, S.; Cychosz, K. A.; Agrawal, K. V.; Al Wahedi, Y.; Bhan, A.; Al Hashimi, S.; Terasaki, O.; Thommes, M.; Tsapatsis, M., Synthesis of self-pillared zeolite nanosheets by repetitive branching. *Science* 2012, 336, 1684-1687.

84. Pretlow, T. G.; Pretlow, T. P., Separation of Cells by Sedimentation. In *Cell Separation Science and Technology*, 1991; Vol. 464, pp 90-102.

85. Pretlow, T. G.; Pretlow, T. P., Velocity sedimentation of cells. *Nature* 1988, 333, 97.

86. Meselson, M.; Stahl, F. W.; Vinograd, J., Equilibrium sedimentation of macromolecules in density gradients. *Proc Natl Acad Sci U S A* 1957, 43, 581-8.

87. Leif, R. C.; Vinograd, J., The distribution of buoyant density of human erythrocytes in bovine albumin solutions. *Proc Natl Acad Sci U S A* 1964, 51, 520-8.

88. Haskill, J. S.; Moore, M. A., Two dimensional cell separation: comparison of embryonic and adult haemopoietic stem cells. *Nature* 1970, 226, 853-4.

89. Timonen, T.; Saksela, E., Isolation of human NK cells by density gradient centrifugation. *Journal of Immunological Methods* 1980, 36, 285-291.

90. Friedman, S. L.; Roll, F. J., Isolation and culture of hepatic lipicytes, kupffer cells, and sinusoidal endothelial-cells by density gradient centrifugation with stractan. *Analytical Biochemistry* 1987, 161, 207-218.

91. Radajewski, S.; Ineson, P.; Parekh, N. R.; Murrell, J. C., Stable-isotope probing as a tool in microbial ecology. *Nature* 2000, 403, 646-649.

92. Hirano, T.; Kobayashi, R.; Hirano, M., Condensins, chromosome condensation protein complexes containing XCAP-C, XCAP-E and a Xenopus homolog of the Drosophila Barren protein. *Cell* 1997, 89, 511-521.

93. Featherstone, C.; Russell, P., Fission yeast P107WEE1 mitotic inhibitor is a tyrosine serine kinase. *Nature* 1991, 349, 808-811.

94. Pertoft, H., Fractionation of cells and subcellular particles with Percoll. *Journal of Biochemical and Biophysical Methods* 2000, 44, 1-30.

95. Vauthier, C.; Schmidt, C.; Couvreur, P., Measurement of the density of polymeric nanoparticulate drug carriers by isopycnic centrifugation. *Journal of Nanoparticle Research* 1999, 1, 411-418.

96. Quintanar-Guerrero, D.; Allemann, E.; Doelker, E.; Fessi, H., Preparation and characterization of nanocapsules from preformed polymers by a new process based on emulsification-diffusion technique. *Pharmaceutical Research* 1998, 15, 1056-1062.

97. Cardoso, A. L. H.; Neto, J. M. M.; Cardoso, A.; Galembeck, F., Chemical heterogeneity in poly styrene-co-(butyl methacrylate) copolymer latexes prepared using different monomer addition modes. A study by isopycnic centrifugation in density gradient. *Colloid and Polymer Science* 1997, 275, 244-253.

98. Neto, J. M. M.; Cardoso, A. L. H.; Testa, A. P.; Galembeck, F., Heterogeneity in polymer latices-detection by zonal centrifugation. *Langmuir* 1994, 10, 2095-2099.

99. Arnold, M. S.; Green, A. A.; Hulvat, J. F.; Stupp, S. I.; Hersam, M. C., Sorting carbon nanotubes by electronic structure using density differentiation. *Nature Nanotechnology* 2006, 1, 60-65.

100. Yanagi, K.; Miyata, Y.; Kataura, H., Optical and conductive characteristics of metallic single-wall carbon nanotubes with three basic colors; Cyan, magenta, and yellow. *Applied Physics Express* 2008, 1.

101. Ghosh, S.; Bachilo, S. M.; Weisman, R. B., Advanced sorting of single-walled carbon nanotubes by nonlinear density-gradient ultracentrifugation. *Nature Nanotechnology* 2010, 5, 443-450.

102. Niyogi, S.; Densmore, C. G.; Doom, S. K., Electrolyte tuning of surfactant interfacial behavior for enhanced density-based separations of single-walled carbon nanotubes. *Journal of the American Chemical Society* 2009, 131, 1144-1153.

103. Yanagi, K.; Iitsuka, T.; Fujii, S.; Kataura, H., Separations of metallic and semiconducting carbon nanotubes by using sucrose as a gradient medium. *Journal of Physical Chemistry C* 2008, 112, 18889-18894.

104. Green, A. A.; Hersam, M. C., Processing and properties of highly enriched double-wall carbon nanotubes. *Nature Nanotechnology* 2009, 4, 64-70.

105. Green, A. A.; Hersam, M. C., Properties and application of double-walled carbon nanotubes sorted by outer-wall electronic type. *Acs Nano* 2011, 5, 1459-1467.

106. Fagan, J. A.; Becker, M. L.; Chun, J.; Hobbie, E. K., Length fractionation of carbon nanotubes using centrifugation. *Advanced Materials* 2008, 20, 1609-+.

107. Lu, Q.; Keskar, G.; Ciocan, R.; Rao, R.; Mathur, R. B.; Rao, A. M.; Larcom, L. L., Determination of carbon nanotube density by gradient sedimentation. *Journal of Physical Chemistry B* 2006, 110, 24371-24376.

108. Zhang, M. F.; Yamaguchi, T.; Iijima, S.; Yudasaka, M., Individual single-wall carbon nanohorns separated from aggregates. *Journal of Physical Chemistry C* 2009, 113, 11184-11186.

109. Sun, X. M.; Tabakman, S. M.; Seo, W. S.; Zhang, L.; Zhang, G. Y.; Sherlock, S.; Bai, L.; Dai, H. J., Separation of nanoparticles in a density gradient: FeCo@C and gold nanocrystals. *Angewandte Chemie-International Edition* 2009, 48, 939-942.

110. Tyler, T. P.; Henry, A. I.; Van Duyne, R. P.; Hersam, M. C., Improved monodispersity of plasmonic nanoantennas via centrifugal processing. *Journal of Physical Chemistry Letters* 2011, 2, 218-222.

111. Mastronardi, M. L.; Hennrich, F.; Henderson, E. J.; Maier-Flaig, F.; Blum, C.; Reichenbach, J.; Lemmer, U.; Kubel, C.; Wang, D.; Kappes, M. M.; Ozin, G. A., Preparation of monodisperse silicon nanocrystals using density gradient ultracentrifugation. *Journal of the American Chemical Society* 2011, 133, 11928-11931.

112. Green, A. A.; Hersam, M. C., Solution phase production of graphene with controlled thickness via density differentiation. *Nano Letters* 2009, 9, 4031-4036.

113. Sun, X. M.; Luo, D. C.; Liu, J. F.; Evans, D. G., Monodisperse chemically modified graphene obtained by density gradient ultracentrifugal rate separation. *Acs Nano* 2010, 4, 3381-3389.

114. Woolson, E. A.; Axley, J. H., Clay separation and identification by a density gradient procedure. *Soil Science Society of America Journal* 1969, 33, 46-48.

115. Jaynes, W. F.; Bigham, J. M., Concentration of iron-oxides from soil clays by density gradient centrifugation. *Soil Science Society of America Journal* 1986, 50, 1633-1639.

116. Bai, L.; Ma, X. J.; Liu, J. F.; Sun, X. M.; Zhao, D. Y.; Evans, D. G., Rapid separation and purification of nanoparticles in organic density gradients. *Journal of the American Chemical Society* 2010, 132, 2333-2337.

117. Ma, X. J.; Kuang, Y.; Bai, L.; Chang, Z.; Wang, F.; Sun, X. M.; Evans, D. G., Experimental and mathematical modeling studies of the separation of zinc blende and wurtzite phases of cdS nanorods by density gradient ultracentrifugation. *Acs Nano* 2011, 5, 3242-3249.

118. Cesarano, J.; Aksay, I. A., Processing of highly concentrated aqueous alpha-alumina suspensions stabilized with poly-electrolytes. *Journal of the American Ceramic Society* 1988, 71, 1062-1067.

119. Luo, L. H.; Tok, A. I. Y.; Boey, F. Y. C., Aqueous tape casting of 10 mol%-Gd2O3-doped CeO2 nano-particles. *Materials Science and Engineering a-Structural Materials Properties Microstructure and Processing* 2006, 429, 266-271.

120. Zhang, D.; Su, B.; Button, T. W., Microfabrication of three-dimensional, free-standing ceramic MEMS components by soft moulding. *Advanced Engineering Materials* 2003, 5, 924-927.

121. Boudreau, L. C.; Tsapatsis, M., A highly oriented thin film of zeolite A. *Chemistry of materials* 1997, 9, 1705-1709.

122. Ha, K.; Lee, Y. J.; Lee, H. J.; Yoon, K. B., Facile Assembly of Zeolite Monolayers on Glass, Silica, Alumina, and Other Zeolites Using 3-Halopropylsilyl Reagents as Covalent Linkers. *Advanced Materials* 2000, 12, 1114-1117.

123. Lee, J. S.; Kim, J. H.; Lee, Y. J.; Jeong, N. C.; Yoon, K. B., Manual assembly of microcrystal monolayers on substrates. *Angewandte Chemie International Edition* 2007, 46, 3087-3090.

124. Liu, Y.; Li, Y. S.; Yang, W. S., Fabrication of Highly b-Oriented MFI Film with Molecular Sieving Properties by Controlled In-Plane Secondary Growth. *Journal of the American Chemical Society* 2010, 132, 1768-+.

125. Liu, Y.; Li, Y. S.; Cai, R.; Yang, W. S., Suppression of twins in b-oriented MFI molecular sieve films under microwave irradiation. *Chemical Communications* 2012, 48, 6782-6784.

126. Liu, Y.; Li, Y.; Yang, W., Fabrication of highly b-oriented MFI monolayers on various substrates. *Chemical Communications* 2009, 1520-1522.

127. Agrawal, K. V.; Topuz, B.; Jiang, Z.; Nguenkam, K.; Elyassi, B.; Francis, L. F.; Tsapatsis, M.; Navarro, M., Solution-processable exfoliated zeolite nanosheets purified by density gradient centrifugation. *AIChE Journal* 2013, 59, 3458-3467.

128. Pham, T. C. T.; Nguyen, T. H.; Yoon, K. B., Gel-Free Secondary Growth of Uniformly Oriented Silica MFI Zeolite Films and Application for Xylene Separation. *Angewandte Chemie International Edition* 2013.

129. Stein, A.; Schroden, R. C., Colloidal crystal templating of three-dimensionally ordered macroporous solids: materials for photonics and beyond. *Current Opinion in Solid State & Materials Science* 2001, 5, 553-564.

130. Zimmerman, C. M.; Singh, A.; Koros, W. J., Tailoring mixed matrix composite membranes for gas separations. *Journal of Membrane Science* 1997, 137, 145-154.

131. Mahajan, R.; Koros, W. J., Factors controlling successful formation of mixed-matrix gas separation materials. *Industrial & Engineering Chemistry Research* 2000, 39, 2692-2696.

132. Cussler, E. L., Membranes containing selective flakes. *Section Title: Plastics Manufacture and Processing* 1990, 52, 275-288.

133. Lee, I.; Buday, J. L.; Jeong, H. K., mu-Tiles and mortar approach: A simple technique for the facile fabrication of continuous b-oriented MFI silicalite-1 thin films. *Microporous and Mesoporous Materials* 2009, 122, 288-293.

134. Hoover, M. D.; Finch, G. L.; Castorina, B. T., Sodium metatungstate as a medium for measuring particle density using isopycnic density gradient ultracentrifugation. *Journal of Aerosol Science* 1991, 22, 215-221.

135. Dyrkacz, G. R.; Ruscic, L.; Marshall, C. L.; Reagan, W., Separation and characterization of FCC catalysts using density gradient separation. *Energy & fuels* 1996, 10, 849-854.

136. Corma, A.; Díaz, U.; García, T.; Sastre, G.; Velty, A., Multifunctional Hybrid Organic– Inorganic Catalytic Materials with a Hierarchical System of Well-Defined Micro-and Mesopores. *Journal of the American Chemical Society* 2010, 132, 15011-15021.

137. Petkov, N.; Mintova, S.; Jean, B.; Metzger, T. H.; Bein, T., Stable mesostructured silicate films containing nanosized zeolite. *Chemistry of Materials* 2003, 15, 2240-2246.

138. Li, X. L.; Zhang, G. Y.; Bai, X. D.; Sun, X. M.; Wang, X. R.; Wang, E.; Dai, H. J., Highly conducting graphene sheets and Langmuir-Blodgett films. *Nature Nanotechnology* 2008, 3, 538-542.

139. Lee, J. A.; Meng, L.; Norris, D. J.; Scriven, L. E.; Tsapatsis, M., Colloidal Crystal Layers of Hexagonal Nanoplates by Convective Assembly. *Langmuir* 2006, 22, 5217-5219.